TAMPERE UNIVERSITY OF TECHNOLOGY
DEPARTMENT OF SCIENCE AND ENGINEERING

LAURI WIROLA

DEVELOPMENT OF A TISSUE-CONDUCTING AUDIO TRANSDUCER AND SENSOR FOR MOBILE USE

MASTER OF SCIENCE THESIS

Subject approved by the department council
15th September 2004
Examiners: Professor Lauri Kettunen
Docent Leo Kärkkäinen

PREFACE

Throw your physic to the dogs. I'll none of it.

-William Shakespeare, Macbeth (1606)

I believe the hardest part about writing the preface is to stay away from clichés. Therefore, I will simply use this opportunity to acknowledge the various persons, who have contributed to this work and my career so far.

Firstly, I want to thank Nokia Research Center for the funding and for the opportunity to do the research work at their service.

Secondly, I want to express my deepest gratitude to my supervisors and mentors professor Lauri Kettunen and docent Leo Kärkkäinen. Their professionalism and experience proved to be indispensable.

Thirdly, my project manager John Cozens and University of Oulu researcher Jari Juuti deserve a fair share of the credit. I have tried to make the best in testing the limits of their expertise.

Fourthly, I want to thank my parents for always making me clear, how valuable proper education truly is. Moreover, an armload of thanks goes to my fiancée Liisa-Ida Sorsa for letting me work late.

Finally, I want to thank my father M.Sc. Hannu Wirola and my high school physics teacher B.Sc. Heikki Juslén for teaching me, how to see the world in terms of Physics.

Tampere, 10th May 2005

Lauri Wirola

Table of contents

ABSTRACT

TAMPERE UNIVERSITY OF TECHNOLOGY

Degree Program in Science and Engineering, Institute of Electromagnetics

Wirola, Lauri:

Development of a tissue-conducting audio transducer and sensor for mobile use

Master of science thesis, 139 pages (printed version)

Examiners: Professor Lauri Kettunen

Docent Leo Kärkkäinen

Funding: Nokia group

Department of Science and Engineering

June 2005

The ever increasing number of mobile devices with a cellular link as well as services associated with them require innovations in audio technologies. Especially problematic are circumstances, in which high background noise level prohibits communication.

This thesis studies a tissue-conducting device for audio reproduction and recording. The proposed concept is not based on producing or sensing pressure changes in air, but in soft tissues. The device considered is an in-ear actuator and sensor that couples to tympanic canal walls.

A finite element model of ear is developed for simulating the actuator function. The FE-model includes a novel idea of using a lumped parameter representation for the middle ear bones. The results are compared with respect to the published data and the approach is found valid. The simulations concerning the actuator function show that the mode is unfeasible due to the energy loss in soft tissues. The result is confirmed by subjective tests.

The prototype of the actuator is analyzed with a FE-model. It is observed that the linear FEM cannot account for the observed characteristics in the actuator response. Therefore, a time-domain model accounting for hysteresis is developed. The hysteresis prediction is realized with a rate-independent Preisach model with an addition of a scalar product model for the reversible part of hysteresis. It is shown that the rate-independent Preisach model is not sufficient to predict the response and that a dynamic model is required.

In the sensor mode the device works up to 2.5-3 kHz, after which the recorded signal drops below the noise floor. The finding is supported by the literature. The transfer function between the speech recorded with a microphone and the device is observed to have a decreasing trend. The study leaves open, whether this effect is due to the tissue transfer characteristics, sensor coupling to the tissue or sensor properties.

Moreover, a comprehensive discussion on the theory associated with the Finite Element Method is given. Both, structural and piezoelectric FEM are covered.

KEYWORDS: FEM, ear modeling, piezoelectricity, piezoelectric actuator, piezoelectric sensor, hysteresis, classical Preisach model, bone conduction, tissue conduction

TIIVISTELMÄ

TAMPEREEN TEKNILLINEN YLIOPISTO
Teknis-luonnontieteellinen koulutusohjelma, Sähkömagnetiikan laitos
Wirola, Lauri:
Kudosjohtavan audioalueen aktuaattorin ja sensorin kehittäminen mobiilikäyttöön.
Diplomityö, 139 sivua (paperiversio)
Tarkastajat: Professori Lauri Kettunen
Dosentti Leo Kärkkäinen
Rahoitus: Nokia Oyj
Teknis-luonnontieteellinen osasto
Kesäkuu 2005

Mobiilaitteiden määrä kasvaa jatkuvasti. Pelkästään GSM-laitteita arvioidaan olleen käytössä vuoden 2004 lopussa noin 1.3 miljardia kappaletta. Laitteiden ja palvelujen määrän kasvu asettaa uusia ja yhä kovempia vaatimuksia laitteiden äänentoistolle sekä -nauhoittamiskyvylle. Nauhoittamisella tarkoitetaan tässä yhteydessä sekä puheen konkreettista tallentamista että laitteella kommunikointiin liittyvää lähipään puheen sisäänottamista laitteeseen.

Erityisen ongelmallisia nykyisin käytetyille audioratkaisuille ovat olosuhteet, joissa taustamelun taso on korkea ja tästä syystä signaali-kohina suhde huono perinteisillä mikrofoneilla nauhoitettaessa. Näissä olosuhteissa yhtenä ratkaisuna käytetään multimikrofonijärjestelmiä, joissa useiden mikrofonien ja digitaalisen signaalinkäsittelyn avulla luodaan keila hyötyäänen suuntaan. Taustamelun tasoa voidaan näin oleellisesti laskea lopullisessa signaalissa. Korkea taustamelun taso on yhtä lailla ongelma myös ääntä toistettaessa, sillä näissä olosuhteissa ääntä ei aina saada tuotettua taustamelua selkeästi korkeammalla tasolla. Tällöin puheen ymmärrettävyys kärsii.

Kokonaan toisentyyppinen lähestymistapa on käyttää luujohtumiseen perustuvia ratkaisuja. Näissä aktuaattori, esimerkiksi värähtelevä osa, kytkeytyy tiukasti pään luuhun ja siirtää aaltoliikkeen kallon luihin. Värähtelyt kulkeutuvat luita pitkin korvan rakenteeseen ja saavat aikaan kuuloaistimuksen. Samaan tapaan luujohtavat sensorit kytkeytyvät esimerkiksi leukaluuhun ja havaitsevat sen värähtelyjä. Olennaista luujohtavissa sensoriratkaisuissa on, että luussa etenevä värähtely on taustamelusta vapaata. Luun/kudoksen ja ilman akustiset impedanssit eroavat niin merkittävästi

toisistaan, että tehon siirtohäviö rajapinnalla on erittäin iso (noin 30 dB). Tästä syystä luuvärähtelyssä on käytännössä ainoastaan puhujan itse tuottama ääni. Suunnittelemalla sensori siten, että maksimoidaan kytkentä korkean impedanssin luuhun ja vastaavasti minimoidaan kytkentä ilmaan, saadaan tuloksena puhdas signaali.

Luu- ja kudosjohtavissa aktuaattoreissa päästään myös erittäin hyvään hyötysuhteeseen. Perinteisesti käytetyissä kaiuttimissa ongelmana on huono hyötysuhde johtuen kahdesta syystä. Ensinnäkin elektrodynaamisten laitteiden lämpöhäviöt ovat isot. Toisekseen mekaanisen järjestelmän kytkentä ilmaan on heikko. Toisaalta, luu- ja kudosjohtavissa aktuaattoreissa kytketään mekaaninen järjestelmä toiseen mekaaniseen järjestelmään. Tällöin impedanssisovitus voidaan suunnitella optimaaliseksi.

Tässä työssä tutkitaan ratkaisua, jossa värähtelijällä kytkeydytään pehmytkudokseen luun sijasta. Tavoitteena on tutkia kudosjohtavan aktuaattorin ja sensorin yhdistämistä yhdeksi laitteeksi, joka sijoitetaan käyttäjän korvakäytävän suulle. Toimiessaan aktuaattorina laite värähtelee radiaalisesti ja siirtää paineaallon korvakäytävän pehmytkudokseen. Aalto etenee käytävän seinämissä tärykalvolle ja saa sen värähtelemään. Vastaavasti sensoritoiminnassa laite havaitsee kudoksen värähtelyjä, jotka syntyvät äänihuulten värähdellessä. Itse asiassa 1960-luvulla tehdyissä tutkimuksissa on todettu, että omasta äänestään ihminen kuulee noin puolet painetietä pitkin ja loput luujohtumisen kautta. Näin ollen kudosten värähtelyamplitudi on paikoitellen, erityisesti kurkun alueella, hyvinkin iso.

Tässä työssä tarkastellaan korvan, erityisesti ulko- ja sisäkorvan, rakennetta ja fysiikkaa. Tämän tietämyksen pohjalta korvan toiminnasta kehitetään FEM-malli. Malli sisältää kuvaukset korvakäytävästä, sitä ympäröivästä rusto-, rasva- ja luukerroksista, tärykalvosta sekä kuuloluista. Kehitetyssä mallissa kuuloluiden geometriaa ei kuitenkaan mallinneta, vaan niiden tärykalvolle kohdistama taajuusriippuva kuorma otetaan huomioon sijaiskytkennän avulla. Lähestymistavan etu on se, että kuorma saadaan mallinnettua suhteellisen tarkasti ilman aikaa vievää geometrian luomista ja verkottamista. Kuorma saadaan FE-mallissa otettua huomioon taajuuden funktiona massa-, jousi- ja vaimennuselementtien avulla. Mallin tuottamien tulosten vertailu julkaistuihin mittaustuloksiin osoittaa, että lähestymistapa ennustaa tärykalvon värähtelyamplitudille oikean taajuusvasteen. Mallia verrataan lisäksi julkaistuihin tärykalvon poikkeamajakaumiin. Myös tämä vertailu osoittaa valitun lähestymistavan oikeaksi.

Mallin avulla tutkitaan korvan käyttäytymistä, kun korvakäytävän pehmytkudokseen herätetään värähtely. Mallin tulosten perusteella voidaan löytää käyttötarkoitukseen parhaiten sopiva värähtelymoodi sekä tarvittava amplitudi. Tässä työssä mallin tulokset kuitenkin osoittavat, että pehmytkudokseen herätetty värähtely häviää rasvakudoksessa eikä energiaa siirry tärykalvolle. Sama tulos saatiin myös mittauksissa, joissa todettiin, että kudosaktuaattorin tuottama havaittu äänenpainetaso ei noussut, kun aktuaattori kytkettiin pehmytkudokseen tai irti siitä. Ainoastaan aktuaattorin rakenteen tuottama akustinen heräte havaittiin.

Kudosjohtava aktuaattori toteutettiin pietsosähköisten elementtien avulla. Värähtelijän toiminta mallinnettiin FE-mallilla, jonka ennustama poikkeamataajuusvaste ei kuitenkaan vastannut mitattua vastetta. Tässä työssä osoitetaan, että syy tähän mallin ja mittauksen väliseen eroon on pietsosähköisten kiteiden hystereesi ja relaksaatio. Taajuusvasteen tarkempaa ennustamista varten pietsovärähtelijän rakenteesta kehitetään hystereesi huomioonottava malli. Hystereesi kytketään analyysiin aikariippumattoman Preisach-mallin avulla. Työssä kuitenkin osoitetaan, ettei aikariippumaton Preisach-malli ole riittävä, vaan että jatkomallinnuksessa tulee käyttää aikariippuvaa mallia.

Kehitettyä kudosaktuaattoria testattiin myös sensorina korvakäytävässä havaitsemaan kudosten värähtelyjä. Sensorin havaittiin toimivan kudostyyppisenä 2.5 kHz:iin asti, minkä taajuuden yläpuolella sensorin akustinen herkkyys kasvaa voimakkaasti, jolloin sensorin toimintakin muuttuu akustiseksi. Myös kirjallisuus tukee havaintoa, että sensori ei toimi kudosjohtumisen avulla enää 2.5 kHz:n yläpuolella. Tämän rajataajuuden läheisyydessä kallon värähtelymoodit muuttuvat eivätkä korvakäytävän reunat enää värähtele.

Työ sisältää myös kattavan katsauksen rakenteellisen FE-mallinnuksen matemaattisiin perusteisiin. Pietsosähköisen ilmiön teorian perusteella johdetaan perusyhtälöt myös pietsosähköisten rakenteiden FE-mallinnukseen.

AVAINSANAT: FEM, korva, luujohtuminen, kudosjohtuminen, pietsosähköisyys, hystereesi, Preisach-malli

LIST OF ABBREVIATIONS

3D	Three-dimensional
A/D	Analog-to-Digital
Anterior	Toward the front, away from back (*medical)*
BC	Boundary Condition
CDMA	Code Division Multiple Access
DOF	Degree Of Freedom in FE-modeling
DSP	Digital Signal Processing
ECE	Ear Canal Exciter
FE	Finite Element
FEM	Finite Element Method
GSM	Global System for Mobile communication
HATS	Head And Torso Simulator
Inferior	Lower (*medical*)
JCG	Jacobi Conjugate Gradient
Lateral	Away from axis or midline (*medical*)
Medial	Towards the axis or midline (*medical*)
NMR	Nuclear Magnetic Resonance
ODE	Ordinary Differential Equation
NB	Narrowband
Posterior	Towards the back, away from front (*medical*)
PoC	Push-to-Talk over Cellular
PZT	Lead Zirconate Titanate
PZT-5H	PZT piezo material, doped with niobium, Nb
RF	Radio Frequency
SNR	Signal-to-Noise Ratio
SPL	Sound Pressure Level
Superior	Upper (*medical*)
TL	Transmission loss
VAD	Voice Activity Detection
VoIP	Voice over Internet Protocol
WB	Wideband

LIST OF SYMBOLS

A	Area
$\underline{a}$	Traction vector in FE-modeling
$\underline{B}$	Magnetic flux density
B^u	Discrete displacement- strain operator in FE-modeling
B^v	Discrete electric field – electric potential operator in FE-modeling
$\underline{b}$	Volume load vector in FE-modeling
C	Heat capacity
C^e	Element damping matrix in FE-modeling
C_e	Electric capacitance
c	Stiffness matrix
c_{ijkl}	Stiffness tensor, 4th rank
D_i	Electric flux density, 1st rank
$\underline{D}$	Electric flux density
d	Piezoelectric matrix
d_{ijk}	Piezoelectric tensor, 3rd rank
E_i	Electric field, 1st rank
$\underline{E}$	Electric field
$\underline{e}$	Strain vector
$\underline{e}_i$	ith basis vector
e_{ij}	Strain field tensor, 2nd rank
$\underline{F}$	Force
$\underline{F_V^e}$	Force on the element due to volume loads in FE-modeling
$\underline{F_P^e}$	Force on the element due to external pressure in FE-modeling
G	Gibbs free energy
g	Inverse piezoelectric matrix
$\underline{H}$	Magnetic field
H_0	Lorentzian distribution parameter
i	Imaginary unit
$\underline{J}$	Current density
K^e	Element stiffness matrix in FE-modeling
K_D^e	Dielectric conductivity matrix in FE-modeling
K_Z^e	Piezoelectric coupling matrix in FE-modeling
k	Spring constant

L	Length
M^e	Element mass matrix in FE-modeling
m	Mass
N^u	Displacement shape function matrix in FE-modeling (element support)
N_i^u	Displacement shape function matrix associated with the ith node
$\underline{N^v}$	Electric potential shape function vector in FE-modeling (support)
N_i^v	Electric potential shape function associated with the ith node
$\underline{n}$	Normal vector
$\underline{p}$	Linear momentum
p_i	Pyroelectric tensor, 1st rank
Q	Heat
$\underline{Q_S^e}$	Nodal surface charges in FE-modeling
$\underline{Q_V^e}$	Element charge density in FE-modeling
q	Volume charge density
R_{mech}	Mechanical damping
S	Entropy
S^u	Displacement-strain operator
S^v	Electric potential – Electric field operator
s	Compliance matrix
s_{ijkl}	Compliance tensor, 4th rank
T	Temperature
t	Time
U	Internal energy
V	Volume
$\underline{u}$	Displacement vector
$\underline{u^e}$	Listing of nodal displacement in FE-modeling
$\underline{u_i^e}$	Nodal displacement in FE-modeling
v	Electric potential
$\underline{v^e}$	Listing of nodal electric potentials in FE-modeling
v_i^e	Nodal electric potential in FE-modeling
W	Work done
$\underline{X}$	Material coordinate
$\underline{x}$	Position vector
Δx	Elongation in x-direction

Z_{mech}	Mechanical impedance
z	z-coordinate of a point
$\hat{\underline{z}}$	Unit vector in z-direction
Δz	Elongation in z-direction
α_{ij}	Thermal expansion tensor, 2nd rank
β_1 , β_2	Rayleigh damping parameters
δ_{ij}	Kroenecker delta
$\delta\underline{u}$	Virtual displacement
δv	Virtual potential
δW	Virtual work
ε_0	Permittivity of free space
ε	Permittivity matrix
ε_{ij}	Permittivity tensor, 2nd rank
ϕ	Phase angle
$\Gamma_{\xi 1,\xi 2}$	Elementary Preisach operator with switching values ξ_1 and ξ_2
γ_1, γ_2	Weight coefficients
Ω	Integration domain
ρ	Density
Ψ	Polarization
$\underline{\sigma}$	Stress vector
σ_{ij}	Stress field tensor, 2nd rank
σ_c	Lorentzian distribution parameter
Θ	Arbitrary tensor quantity
υ	Velocity
υ_{medium}	Velocity of sound in a given medium
ω	Angular frequency

ABOUT NOTATION

Differentiation

When assigning partial derivatives, the variables kept constant in the differentiation are in the lower right hand corner in brackets. For instance, in

$$\varepsilon_{ij} = \left.\frac{\partial D_i}{\partial E_j}\right|_{(\sigma,T)}$$

stress (σ) and temperature T are kept constant in the differentiation.

Moreover, depending upon what is practice in the literature, different types of differentiation symbols are used in the thesis. These are now stated for the sake of clarity.

$$\partial_x = \frac{\partial}{\partial x} \text{ and } \dot{y} = \frac{\partial y(t)}{\partial t}$$

Material constants

In the previous example, ε_{ij} found by differentiation assumes constant stress and constant temperature. In this work, this behavior is expressed by writing $\varepsilon_{ij}^{(\sigma,T)}$, which implies that the permittivity value stated applies under constant stress and constant temperature.

LIST OF FIGURES

LIST OF TABLES

1. INTRODUCTION

Mobile devices constantly find their use in new applications and usage scenarios. This trend is simply based on the ever growing number of device users. According to [30], in the end of 2004 there were 1.268 billion GSM-subscribers and, for instance, 16.3 million WCDMA (3G) users. Even though the amount data transferred in the wireless networks increases rapidly, voice services will continue to dominate operators' revenues and profits [23]. In addition, as new voice-based service concepts, such as *Push-to-talk over Cellular* (PoC) and *Voice over Internet Protocol* (VoIP), are launched, it becomes clear that new innovations are needed for audio recording and reproduction.

Traditionally audio is reproduced by the means of electrodynamic loudspeaker. However, due to the impedance mismatch between mechanical and acoustic domains, the power transmission between the two domains is generally quite weak. Typically, only 1% of the input electrical power is converted to acoustic power. Hence, substantial amount of heat is produced in the system, which power loss must be controlled and transferred away. Since there is no excess power in mobile devices to waste, any improvement in the efficiency is valuable.

The efficiency problem may be approached by reproducing audio in a non-traditional way. It has been found [9] that a person hears approximately half of one's own voice via pressure path and the other half by bone conduction. A non-traditional approach uses the latter path to produce the sensation of hearing. Advantages include substantially better impedance matching and, hence, efficiency. This is because now two mechanical domains, actuator and the human, are coupled directly instead of trying to optimize the weak mechano-acoustic coupling.

As the number of applications increases, mobile devices also find their use in more and more demanding circumstances. Already now it is a common practice to offer consumers devices that can tolerate moisture, dust and mechanical shocks. However, audio solutions that can cope with high background noise levels are still few. Often the performance is also highly dependent on the noise type (for instance, traffic, music, speech or wind).

The noise problem is associated with the isotropic directional response of pressure microphones. Traditional pressure microphones receive equally well background noise as well as the desired information from a sound source. One solution to overcome this

inherent problem is to use several pressure microphones and by the means of digital signal processing (DSP) generate a beam towards the sound source. Simultaneously, noise originating from the surrounding sources is rejected or reduced. This technology is known as beam forming.

Another option is to pick-up the speech information directly from the tissue vibrations as the person speaks. Since about half of the sound is transmitted via the bone conduction path, tissue vibrations originating from the speech production are strong enough for enabling sound recording from skin surface. Advantages in recording the speech directly from the tissue include high external noise rejection. Power transmission loss (TL) at the air-tissue boundary is in the order of –30 dB. Therefore, the amplitude is reduced by 60 dB at the boundary. Hence, the tissue vibrations are fairly free from external noise even if high level of noise should be present in the surroundings.

The use of bone/tissue conducting actuators and sensors for audio reproduction and recording is not a novel idea. In fact, several patents quote utilizing such technology.

The US patent US20030048915 A1, Communication device using bone conduction, describes a bone-conducting actuator hidden in the earpiece of eye-glasses. Such an arrangement provides tight coupling to the skull bone in the ear region. The force transducer is of electromechanical type. The invention also includes a conventional microphone for sound recording.

The patent WO0207477 A2, Audio headset, utilizes a traditional loudspeaker to reproduce audio. However, the sound recording takes place inside the ear canal. The inventor claims that the sound in a closed ear canal is free from the external noise, but contains the speech produced by the person. Audio is recorded with a traditional miniature microphone from the ear canal.

The US patent US6463157 B1, Bone conduction speaker and microphone, utilizes piezoelectric benders to reproduce and record audio from bone. The actuator and sensor are “strategically” placed in contact with user’s head or head area. The invention claims to attenuate external noise by more than 80 dB by optimizing the mismatch between air and the sensor. Invention is a very traditional bone-conduction solution with separate actuator and sensor.

The patents quoted work to show the variety of audio devices and concepts utilizing bone/tissue conduction. However, it seems that the research topic undertaken in this thesis has its space within the patents. This is because the thesis is set to examine the possibility to combine the tissue conducting actuator and sensor. The project goals include developing a high-efficiency actuator, a noise-rejecting sensor and having a minimal cross-talk between the two functions. The concept chosen for the study comprises of a hands-free device inserted in the user's ear similarly to the insert-ear earphones. The actuation and sensing shall be realized with piezoelectric structures due to their high mechanical impedance, low cost and low energy consumption.

2. EAR CANAL EXCITER -PROJECT

2.1 The concept

The originator of the idea for the Ear Canal Exciter (ECE) is Ph.D. Leo Kärkkäinen from Nokia Research Center, Finland. The idea was first introduced in the late 2003, and the actual project concerning the development of the ECE was commenced in February 2004.

The principle behind the ECE is straightforward. Whereas the coupling of traditional transducers to air is weak, the coupling from a mechanical device to a mechanical system can be made strong. The ECE is a device designed to connect to the ear mechanically, not via an acoustic pressure path. The principal idea is to develop a small insertion earphone that fits into the user's concha and/or ear canal. The fit is made tight by applying a layer of silicone rubber on the device. This layer works to provide comfort as well as impedance matching to the surrounding tissue.

Figure 1 shows that once in ear, the ECE device is surrounded by skin, cartilage, fat and bone. It is hypothesized that the mechanical vibration produced by the ECE device is transferred to the eardrum as vibration in the canal skin as well as via bone conduction directly to cochlea. Similarly, the ear canal walls are known to vibrate as a result of human sound reproduction [9]. This vibration may be detected and recorded as audio signal.

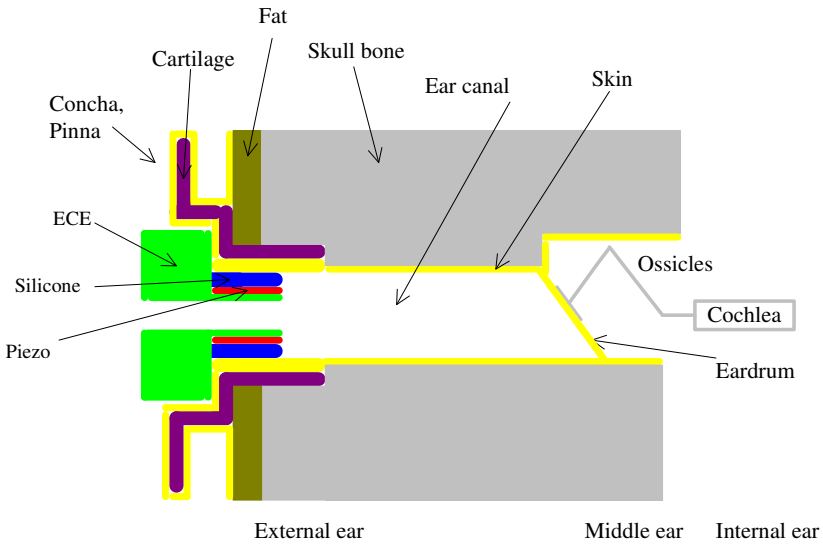

Figure 1. Schematic view on the ECE working principle.

Due to this working principle, ECE is very different from the known concepts, some of which were introduced in the previous chapter. None of the concepts known combine the actuator and sensor or utilize tissue-type conduction. In contrast, the known actuators make an attempt to couple to the skull bone.

The ECE concept also provides advantage in various use cases, in which hearing external sound environment is necessary. Such cases include driving a car or bin-aural recording. Now, the ECE device may easily be made either transparent or non-transparent to the external sounds. Figure 1 shows the ECE with a hole through its circular structure. The hole now allows for externally excited pressure waves to enter the ear canal. By blocking the hole, the ECE may be used as an ear-plug still allowing for two-way communication. A fine concept might include using the ECE in a high-noise environment, in which the ECE would provide both, protection of hearing (ear-plug function) and communication channel coping well in the problematic surroundings. The ECE device providing a noise-free uplink signal might be of great value in such circumstances.

From the concept point of view, the ECE may be a stand-alone Bluetooth-based solution or a wired one. In either case, the required signal processing (equalization, noise-suppression, echo cancellation) is performed in the mobile device. This is due to the mobile device having a dedicated processor for the task. Hence, adding such a processor to the ECE device would only increase costs.

If the ECE is to work as a stand-alone solution, the casing must include at least a power source, RF-circuitry and power amplifier. Moreover, a DC-DC up-converter may also be required, because piezos generally need higher driving voltages as compared with traditional electrodynamic actuators. Since there are two power-intensive circuits in the system, RF-circuit and the up-converter, the power consumption control is critical. The bluetooth-based hands-free devices utilizing traditional actuator technology have fairly short battery life. As a piezo-based solution is used, the situation may potentially further worsen.

In contrast, if the ECE is used in a wired mode, the power consumption is less critical, since the power may be drawn from the mobile device. Also, as no RF-circuitry is needed, the structure of the device is generally less complicated.

Considering then the bandwidth requirements for the device, it is noted that the current Narrowband (NB) audio standard includes frequencies 300-3400 Hz. Initially, the goal is to examine the ECE functionality in this frequency band. However, the Wideband (WB) standard includes frequencies 150-7000 Hz. Secondarily, the ECE function in this band is examined.

2.2 Approach

This thesis is a proof-of-concept type research. The aim is not in developing a finished and stylized product with the required electronics. In fact, the goal is to establish the required competence in the both technology areas, bone/tissue conduction and piezoelectric structures. Learning the required modeling skills and performing the characterization of the manufactured prototype are included in the task. Moreover, being able to give recommendations for the future development directions is appreciated.

The project consists of modeling work, prototyping and measurements in order to verify the models and the concept.

In the early stages of the project it was decided to pursue the modeling and prototyping paths simultaneously. The decision was based on time savings achieved by designing the prototype based on best guesses and at the same developing a detailed model of the ear behavior. The prototype may then be used for the model verification purposes as well as to produce experiences that can be employed in the further prototype and model development. In addition, a coarse model of the prototype must be developed for the manufacturing purposes. Later, the ECE model will be tuned in order to develop the prototype, optimize its function as well as build up modeling skills.

The prototype manufacturing was given to the subcontractor. The University of Oulu (Finland) Microelectronics laboratory has world-class competence in producing piezoelectric structures and, hence, it was chosen as the partner. Microelectronics laboratory has the responsibility to model and manufacture the first prototype.

The development of the Finite Element (FE) model describing the ear behavior under the function of ECE shall be initiated simultaneously with the subcontracting project. The task includes learning about the ear structure in order to be able to identify the key elements for

the model development. The Finite Element model on the ear will provide estimates on the transmission loss and the transfer path characteristics.

2.3 Potential problems known

Before initiating the actual research work, various potential problems may be identified within the different sub-tasks.

Human ear. From a modeling point of view, the human ear is challenging. The geometry associated with the structure is complicated. The geometry must be simplified to a great degree and, hence, detailed knowledge on the anatomy is required in order to be able to make the necessary modeling decisions. Also, the mechanical parameters needed in the modeling work may not be well established. At least they have high uncertainty, which leads to a need to run simulations with varied parameters.

Also, it is unknown whether the concept has any possibilities to function properly. As noted, the traditional bone conducting solutions, as their name implies, try to excite the skull bone. Now, as tissue-type conduction is utilized, the performance is unknown. Moreover, considering the sensor function, it is known that military applications have long used throat-type microphones. Now, as the tissue vibration is sensed in the ear, it is unknown to what degree the vibrations have attenuated. The signal may also be distorted, if the transfer path should behave non-linearly.

Finally, the varying anatomies may pose a challenge to the device design. In order to achieve a proper coupling between the device and tissue, the fit in the canal must be tight. Now, it may be hypothesized that ear canal shapes vary significantly depending upon, say, age and gender. This issue is not considered in detail in the study, but should be kept in mind considering the future development.

Piezo technology. Piezos are generally known to be high-force low-displacement type devices. In practice, high voltages are required in order to obtain high displacement levels. The problem becomes especially critical in mobile devices, in which power consumption must be maintained minimal. Although there are various emerging technologies, such as single-crystal and multilayer solutions, in the piezo area, the voltage requirements still remain higher than in traditional electrodynamic solutions. The new solutions are fairly expensive and, hence, unacceptable. DC-DC up-converters are a well-established

technology and might be suitable for the current task. However, since the current work is only a proof-of-concept study, the voltage issue is not considered in detail. It is only noted that such issues exist as piezo technology is utilized.

Measurements. The measurements required in the characterization may be divided in subjective and non-subjective measurements. The non-subjective measurements are generally straightforward and include, for instance, certain frequency responses.

Subjective measurements include the characterization of the tissue transfer path. Both, the actuator and sensor functions must be characterized by subjective measurements. The method induces uncertainties in the measurements due to varying anatomies between the subjects. It may also be difficult to repeat measurements due to various human factors. However, the method chosen is considered the only feasible means at this stage. A full discussion on the measurement method and the associated uncertainties is given in the thesis.

2.4 Intellectual property rights

The concept concerning the function and the use cases of the ECE are owned by Nokia group, Finland. The patent application has been filed in Finland. The application FI 20041625 is included in the appendix B.

3. HUMAN EAR

3.1 Ear anatomy

Human ear (*organum vestibulocochleare*) consists of three main sections: external, middle and inner ear. In addition to carefully summarizing the key elements in the external and middle ear, some insight on the function of inner ear is given as well. Now, the three parts are examined in turn.

3.1.1 External ear

External ear is the part of the human hearing system beginning from *auricle* and ending at the *tympanic membrane*. A detailed view on the external ear can be seen in figure 2.

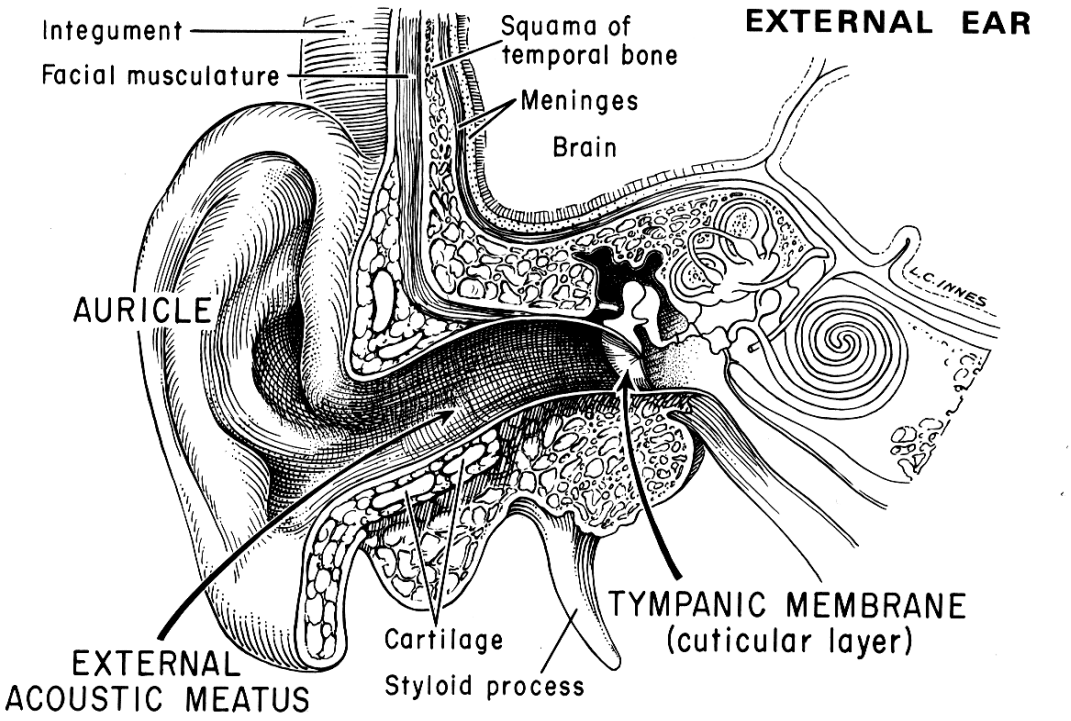

Figure 2. Schematic view on the external acoustic meatus. Figure source [4].

Auricle is the outmost part of the human ear. It is the visible part of the hearing organ and is fastened to the side of the head. Its function is to enable sound source localization at the frequencies above 1 kHz. Below 1 kHz localization is based on the phase difference of the incoming wave between the ears. However, above 1 kHz the wavelength approaches the dimensions of head and, hence, sound pressure level becomes dependent upon the

orientation of head [9]. Auricle consists of elastic fibrocartilage covered with a thin layer of skin [3].

The deep impression in the middle of auricle is called concha. Opening of concha leads to the external acoustic meatus, or tympanic canal. Tympanic canal is terminated medially by the tympanic membrane. Moreover, the canal may by subdivided into two parts. The lateral part, approximately one-third of the total length, is cartilaginous and the medial two-thirds is osseous. The division is illustrated in figure 2. In the cartilaginous section the canal skeleton is provided by cartilage, whereas in the osseous part the canal consists of thin skin surrounded by bone. The cartilage is fixed to the bone at the transition point. The skin lining the canal skeleton is continuous from auricle to the tympanic membrane, where the canal skin forms the outmost layer of the membrane. The thickness of the highly fibrous skin at the cartilaginous part is approximately 1 mm and 0.2 mm at the osseous part [3]. Moreover, in the thick tissue of the cartilaginous part there are ceruminous glands that secrete ear wax. The cartilaginous part is also covered with hair, while in the osseous part the amount of hair is minimal. It should be noted that the ECE is designed to function in the cartilaginous section exciting the thick soft tissue rather that thin.

Canal is, on average, 25 mm long in posterosuperior wall and 31 mm long in anteroinferior wall [4]. This results from the tympanic membrane being positioned in angle with respect to the canal axis. This angle includes individual variations, but [19] gives the angle a mean value of 55°, which is the angle used in the modeling work. The canal is elliptic in cross-section with the longer axis being vertical at the concha, but almost horizontal at the tympanic end. At the tympanic end, the longer axis is on average 9 mm and the shorter axis 6 mm [4]. The shape of ear canal is advantageous in the ECE design work, since it allows for designing a device that fits in the canal in a certain position only.

However, not only the cross-section is complicated in shape, but so is also the behavior of the canal axis. On average, the canal courses somewhat upwards in the cartilaginous section and somewhat downwards in the osseous section. However, in the horizontal plane the canal is somewhat S-shaped. The part, in which the canal radius of curvature is greatest, is somewhat smaller in cross-sectional area than the rest of the canal. [3]

From the ECE point of view, the most problematic issue with the external ear is that its dimensions change with the jaw movement [3]. This behavior may result in the need for the ECE having somewhat flexible structure so that it can adjust to the dimension changes.

In acoustic sense, the tube formed by the tympanic canal works as a band-pass filter. In the external acoustic meatus, the audio signal is still in pressure domain. The tube that is closed at the other end, resembles a quarter-wave resonator, which implies a resonance frequency of approximately 345 ms^{-1} / (4 · 25mm) ≈ 3500 Hz. Moreover, the resonance occurs over a wide range of frequencies, since the tympanic membrane provides damping to the system and lowers its Q-value. Typically, the canal amplifies frequencies between 3 and 5 kHz approximately 10 dB. At 1 and 8 kHz the amplification has already dropped to 1 dB [74]. Therefore, the gain introduced by the tympanic canal to the middle frequencies is significant.

3.1.2 Middle ear

The middle ear consists of the tympanic membrane, tympanic cavity, the ossicles (the hearing bones) and auditory tube. The purpose of the middle is to convert audio signal from the pressure domain to the mechanical domain so that the signal can be mediated further to the inner ear. A detailed view on the middle ear is given in figure 3.

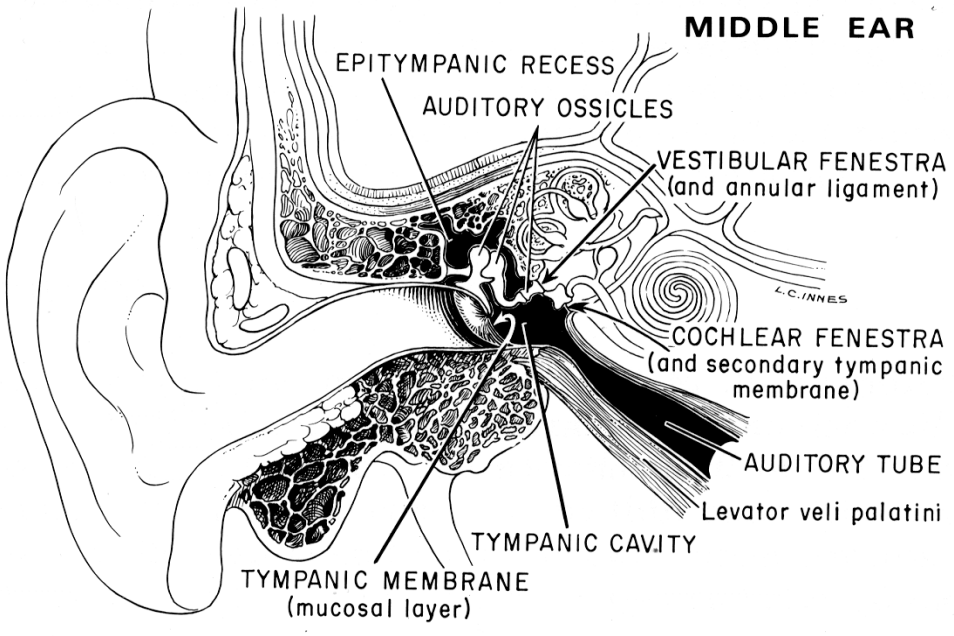

Figure 3 . Schematic view on the middle ear. Figure source [4].

Tympanic cavity is an 0.5-cm^3 mucus-covered cavity located behind the tympanic membrane. Cavity is bounded laterally by the tympanic membrane and medially by the inner ear wall. Mechanically the tympanic cavity acts as a spring load on the membrane. [72]

Eustachian, or auditory, tube connects the middle ear air space to the nasal cavities. The tube provides the means to equalize pressures in the external acoustic meatus and the middle ear cavity. This pressure equalization ensures that the tympanic membrane maintains maximal receiving sensitivity in all circumstances.

Tympanic membrane

The tympanic membrane is located at the end of the external meatus and, hence, it separates the external acoustic meatus from the tympanic cavity. The membrane is positioned approximately in a 55º-angle with respect to the canal floor. [72]

The membrane itself can be seen in figure 4. It is oval in form having a maximum diameter of 10 mm and an 8-mm diameter perpendicular to the greatest diameter. Membrane thickness varies from 55 to 90 μm and weighs approximately 14 mg. [3]

The tympanic membrane may be subdivided in three major sections as illustrated in figure 4. Pars flaccida is the thinnest section and is located superiorly. Pars tensa forms the major part of the membrane and is somewhat thicker than pars flaccida. The third section, manubrium, is a part of the most lateral hearing bone, malleus. The three sections have different mechanical properties as well as differences in nervous and venous patterns. Moreover, the membrane is not confined to a single plane. Rather, its inner surface is convex resulting from the malleus tensing the membrane and drawing it approximately 2 mm medially. The point of greatest displacement is called umbo. [3]

The tympanic membrane attaches to the surroundings by two different manners. The outer edge of pars tensa is a fibrocartilaginous ring (tympanic annulus), which is fixed to the tympanic sulcus of the temporal bone. However, the ring is deficient superiorly at the Notch of Rivinus. In this region the tympanic membrane connects directly to the tympanic bone. These restraints are of the greatest importance, when considering the ear model boundary conditions. [4]

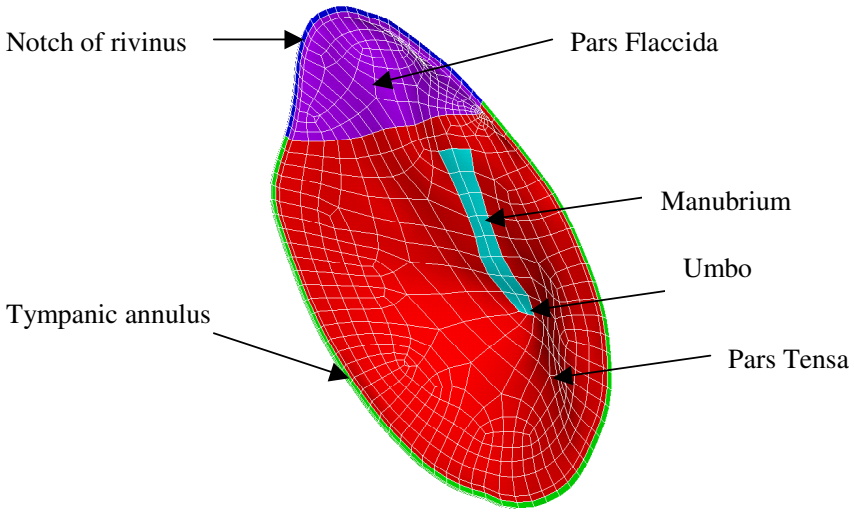

Figure 4. Sections of tympanic membrane

Structurally there are three layers to the membrane. Layers contribute to the mechanical properties of the membrane sections. Outmost and inmost layers are composed of canal skin and cavity mucus, respectively. However, the middle layer has the most profound effect on the membrane properties, since it consists of radial and circumferential fibers. [72]

The function of the tympanic membrane is to absorb the incoming pressure signal and transform it to translational and rotational energy. Its compliance, cone shape and low mass make the membrane especially suitable for sound absorption [74].

The auditory ossicles

The ossicles include three movable, small bones: malleus, incus and stapes. Malleus is attached to the tympanic membrane (manubrium), whereas stapes footplate connects to the inner ear. The auditory ossicles are shown in figure 5.

To give an insight on the size of the bones, it should be noted that they are located in the tympanic cavity having a volume of 0.5 cm^3. Malleus is 8-9 mm, incus 5 mm and stapes 3 mm long [4]. Their total mass varies from 50 to 63 mg. In addition to the ossicles itself, the cavity also includes various tendons and muscles that connect to the ossicles. Without going into the details, the muscles, tensor tympani and stapedius, have an important role in protecting ear from high SPL signals. In effect, the muscles can make the mechanical transmission path more rigid in order to reduce the oscillatory amplitude [72].

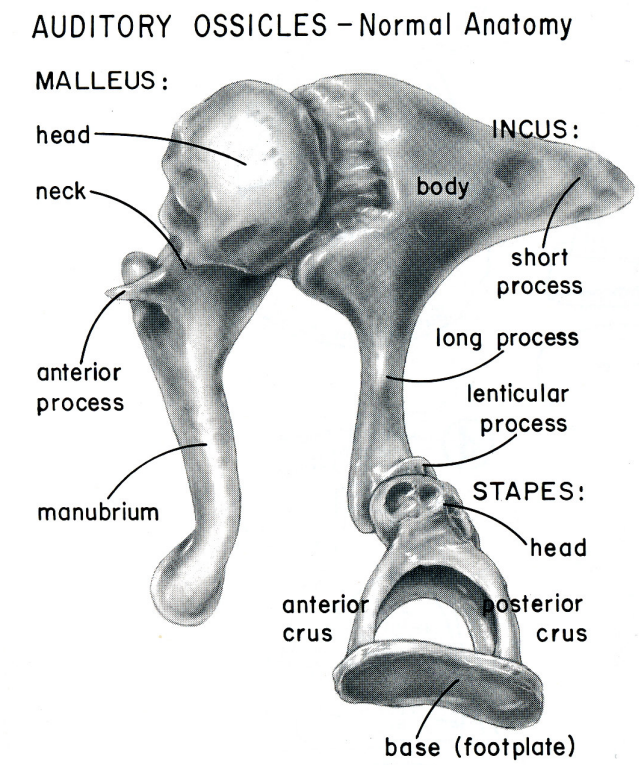

Figure 5. Normal adult auditory ossicles. Figure source [4].

Mechanically, the auditory ossicles provide impedance matching between air and inner ear fluid. In order to see, why this is an important function, consider a direct coupling of air to the cochlear fluid. It is known that the power transmission loss on the medium boundary can be given as a function of acoustic impedances. Assuming a plane wave, impedance can be given by the product $\rho_{medium} v_{medium}$ where ρ_{medium} and v_{medium} are density and velocity of sound, respectively. Using $\rho_{air} = 1.29$ kgm^{-3}, $v_{air} = 340$ ms^{-1}, $\rho_{water} = 1000$ kgm^{-3} and $v_{water} = 1500$ ms^{-1}, it is obtained for the power transmission loss, TL, that

$$\mathrm{TL} = 10 \cdot \log_{10}\left[4 \cdot \frac{Z_{air}/Z_{water}}{(1 + Z_{air}/Z_{water})^2} \right] = 10 \cdot \log_{10}\left[\frac{4 \cdot (\rho_{water} v_{water} / \rho_{air} v_{air})}{(1 + \rho_{water} v_{water} / \rho_{air} v_{air})^2} \right] \approx -30\,\mathrm{dB} \quad (1)$$

This is exactly the hearing loss observed with patients lacking the middle ear structure. The transformer action now required to compensate for the impedance mismatch, is provided by the lever ratio of the ossicles (about 1.5) and area difference between the tympanic membrane and stapes footplate (about 17). In total they account for $20 \cdot \log_{10}(1.5 \cdot 17) \approx +28$ dB. In fact, the middle ear works as a band-pass filter, since the pressure in the inner ear actually exceeds the pressure at the tympanic membrane in the

range from 0.1 to 10 kHz with the maximum amplification occurring in the vicinity of 1 kHz. [74]

3.1.3 Inner ear

Whereas external and middle ear anatomy as well as function contribute to the ECE design, inner ear has no apparent effect on the design process. However, its anatomy and function is reviewed for consistency. A detailed view on inner ear is given in figure 6.

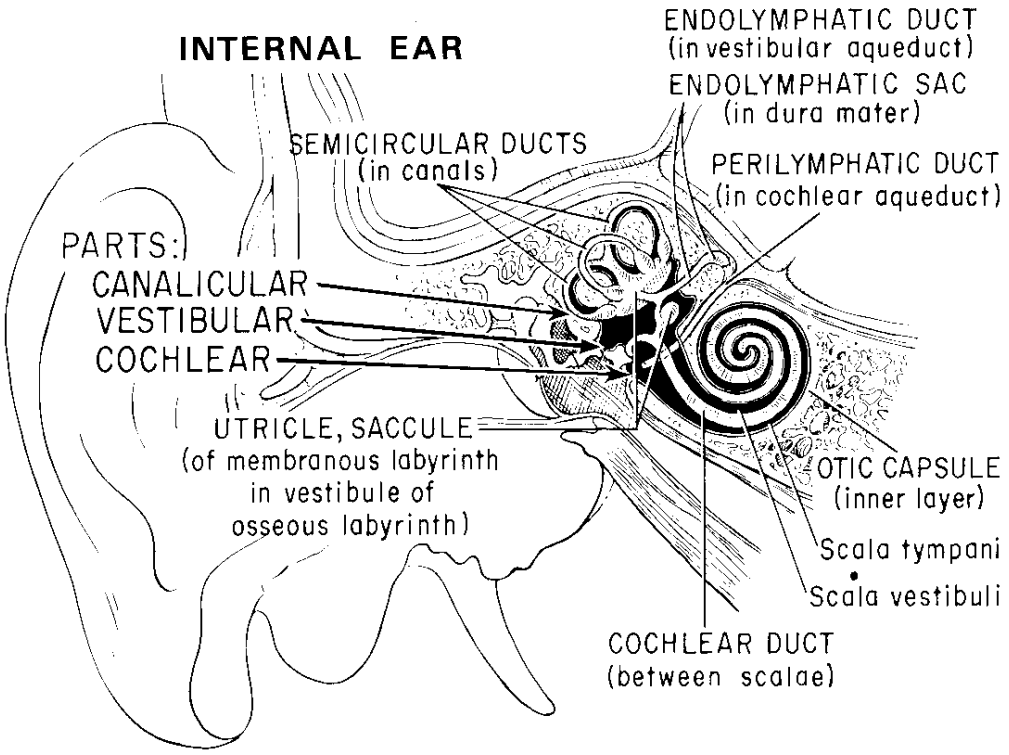

Figure 6. Internal ear anatomy. Source [4].

Anatomy of internal ear is extremely complex with various labyrinths, ducts and organs. For the review purposes, it suffices to concentrate on the superstructure and on two widely known specific organs, semicircular canals and the cochlea.

In the superstructure, the internal ear consists of two parts, the perilympatic (osseous) and endolympatic (membranous) labyrinths. The membranous labyrinth is contained within the bony labyrinth and follows fairly faithfully the osseous canal form. Ultimately, the both labyrinths are contained within the bony otic capsule [4].

In the microstructure, the membranous labyrinth contains semicircular canals, utricle and saccule as well as the cochlea. Semicircular canals are connected to the cochlea via utricle and saccule, which are contained within a bony cavity called vestibule. Moreover, all four organs are filled with the same fluid called endolymph, but they all float within another fluid, perilymph, in order to isolate the hearing system effectively from body-borne disturbances. The fine division is illustrated in figure 7. [72]

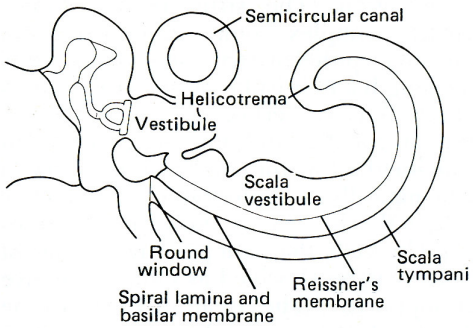

Figure 7. Schematic structure of the membranous labyrinth. Source [74].

Semicircular canals are the three membranous ducts visible in figure 6. They begin and end at the utricle. Functionally, semicircular canals are responsible for the maintenance of equilibrium. Movements of head and body cause disturbances in the canal fluid, which disturbances are sensed by sensory cells. The organ delivers information on both the static position of head in space as well as the kinetic state of the body. [74]

The cochlea is the ultimate hearing organ, which terminates the mechanical transfer path of the audio signal. Its sole function is to transform the pressure signal picked by the tympanic membrane and matched by the ossicles to an electric signal for further processing in the nervous system.

The cochlea is a 35-mm fluid filled organ that lies inside a bony cochlear canal. The canal as well as the cochlea have a spiral form as shown in figure 6. The cochlea is divided in upper and lower ducts called scala vestibule and scala tympani, respectively. Scala vestibule and tympani are connected at the apex of cochlea, helicotrema.

The cochlea has three openings to it. The first one, oval window, is the site of the stapes footplate. Through this window, the pressure excitation from the ossicles is transferred into the cochlear fluid. Specifically, the oval window opens to scala vestibule. The second opening, round window, terminates scala tympani. In fact, the round window is a

secondary tympanic membrane that allows pressure to equalize in the tympanic cavity. As the stapes footplate moves, it generates pressure changes within the cavity. However, simultaneously the round window, which is connected to the oval window via the scalae fluid, moves approximately out-of-phase and equalizes pressure within the tympanic cavity. This is yet another method to maximize the sensitivity of the ear in all circumstances. Finally, the third opening connects the cochlea to the saccule and further to the semicircular canals. However, the coupling between the cochlea and the semicircular canals is extremely weak due to the small size of the connecting tubes. [74]

The actual process of hearing takes place at the organ of Corti that is located at the upper surface of the basilar membrane shown in figure 7. The organ of Corti contains approximately 20 000 hair cells that react to the stapes induced pressure changes within the cochlear fluid. Moreover, the basilar membrane has a variable stiffness due to changing geometry along its length, which yields a location-dependent frequency response. In fact, the cochlea performs a frequency-location Fourier-transform, which allows the cochlea to differentiate between tones of different frequency. The cochlea and its mechanical properties are also responsible for various other phenomena, such as masking effect and loudness. [46] [74]

4. THE FINITE ELEMENT METHOD

4.1 Lagrange and Euler descriptions

Finite Element (FE) modeling is about formulating boundary value problems in finite-dimensional function spaces. Zienkiewicz [75] defines Finite Element Method (FEM) as a method to approximate continuum in such a way that the continuum is divided into finite number of parts, in which the continuum is approximated by a finite-dimensional function space.

In this work, FEM is used for modeling mechanical and electromagnetic phenomena. In the following three chapters, basic equations are derived for structural analysis. Structural FEM shall be utilized in ear modeling. The piezoelectric analysis, on the other hand, combines structural and electromagnetic analyses. Piezoelectric FE-modeling is considered in detail in the chapter 6.3.

Before proceeding with the discretization process, fundamental continuum mechanics principles are introduced. First, the Lagrangian and Euler descriptions are defined.

Whenever a continuum is in motion, tensor quantities that are associated with the particles in a body change as a function of time [44]. The corresponding changes can be represented in either Lagrangian or Euler descriptions.

Lagrangian description is based on following the movement of a particular particle. Here, the particle is identified by its initial position, the material coordinate $\underline{X}$. Hence, a given material quantity Θ is represented by $\Theta(\underline{X},t)$. In the Lagrange description, particle displacement $\underline{u}$ is given by $\underline{u}(\underline{X},t) = \underline{x}(\underline{X},t) - \underline{X}$, where $\underline{x}$ is the particle location.

Another option is to observe changes at a fixed location $\underline{x}$. This is known as the Euler description and the quantity Θ is expressed by $\Theta(\underline{x},t)$. The particle displacement is therefore expressed by $\underline{u}(\underline{x},t) = \underline{x} - \underline{X}(\underline{x},t)$. Here it is assumed that the initial location of the particle, $\underline{X}(\underline{x},t)$, can be deduced by observing the particle at the location $\underline{x}$.

Typically, the Euler description of the quantity is known. On the other hand, the conservation laws are usually expressed in the Lagrange description. The rate of change of $\Theta(\underline{x},t)$ must therefore be expressed in the Lagrange description. This rate is obtained from the convective derivative defined in equation (2).

$$\frac{D}{Dt}\Theta(\underline{x}(\underline{X},t),t)=\frac{\partial\Theta}{\partial x_i}\frac{\partial x_i}{\partial t}+\frac{\partial\Theta}{\partial t}=grad(\Theta)^T\,\underline{v}+\frac{\partial\Theta}{\partial t}, \tag{2}$$

where $\partial x_i \big/ \partial t$ are evaluated with constant X_i. These time derivatives define the velocity $\underline{v}$ of the particle.

4.2 Conservation laws

There are two conservation laws to be taken into account in deriving the continuum equations. These are the conservation of mass and linear momentum.

The conservation of mass can be se stated by

$$\begin{aligned}0=\frac{Dm}{Dt}=\frac{D(\rho\Delta V)}{Dt}=\Delta V\frac{D\rho}{Dt}+\rho\frac{D(\Delta V)}{Dt}=\Delta V\frac{D\rho}{Dt}+\rho\Delta V div(\underline{v})\\ =\Delta V\left(\underline{v}^T grad(\rho)+\frac{\partial\rho}{\partial t}+\rho div(\underline{v})\right)=\Delta V\left(div(\rho\underline{v})+\frac{\partial\rho}{\partial t}\right)\end{aligned}, \tag{3}$$

where m represents mass, ΔV virtual volume and ρ density. The principle of convective derivative has been utilized in order to obtain the final form.

The conservation of linear momentum is given by

$$\underline{F}=\frac{D\underline{p}}{Dt}=\frac{D(m\underline{v})}{Dt}=\underline{v}\frac{Dm}{Dt}+\rho\Delta V\frac{D\underline{v}}{Dt}=\rho\Delta V\frac{D\underline{v}}{Dt}=\rho\Delta V\left(grad(\underline{v})^T\,\underline{v}+\frac{\partial\underline{v}}{\partial t}\right), \tag{4}$$

where $\underline{F}$ is force and $\underline{p}$ linear momentum. Again, the convective derivative gives the final form.

Next, force exerted on a virtual volume element ΔV is considered. The Cauchy lemma states that the pressure exerted on the area defined by the normal vector $\underline{n}$ is given by the linear mapping

$$\sigma_{ij}\,\underline{n}=\underline{a}, \tag{5}$$

where σ_{ij} is a certain 2nd rank tensor field and $\underline{a}$ the traction force vector. As the lemma is superimposed on a volume ΔV, it turns out that the force density in a small volume can be given as the divergence of the field σ_{ij} [43]. Hence,

$$\underline{F} = \rho\left(\underline{v}^T grad(\underline{v}) + \frac{\partial \underline{v}}{\partial t}\right)\Delta V = div\,\sigma_{ij}\,\Delta V = \partial_m \sigma_{im}\,\underline{e_i}\,\Delta V \tag{6}$$

The tensor field σ_{ij} is called the stress tensor. Moreover, $\underline{e_i}$ is the i[th] basis vector.

Now, equation (6) allows for writing the Cauchy equation of motion that defines the dynamics of any given body. The Cauchy equation may be expressed in the absence of losses and thermal strains [44] by

$$\rho\ddot{\underline{u}} = div\,\sigma_{ij} + \rho\underline{b}\,, \tag{7}$$

where $\underline{b}$ is the volume specific load vector. In the structural FEM, equation (7) is approximated in finite-dimensional function spaces.

4.3 Deformation of the body

Before proceeding with the discretization, the means of deducing the deformation of the body from the stress tensor must be developed.

The measure of deformation is the strain tensor e_{ij} and its form can be deduced by considering, how the scalar product between two points changes in the deformation. By the Lagrange definition, the particles initially at $\underline{X}$ and $\underline{X} + \underline{dX}$ arrive at the positions $\underline{x}$ and $\underline{x} + \underline{dx}$ after the deformation. Now,

$$\underline{x} = \underline{X} + \underline{u}(\underline{X}, t) \tag{8}$$

and

$$\underline{x} + \underline{dx} = \underline{X} + \underline{dX} + \underline{u}(\underline{X} + \underline{dX}, t) \tag{9}$$

Therefore,

$$\underline{dx} = \underline{dX} + \underline{u}(\underline{X} + \underline{dX}, t) - \underline{u}(\underline{X}, t) = \underline{dX} + \underline{dX}^T grad(\underline{u})\,, \tag{10}$$

where $grad(\underline{u})$ is the displacement gradient. Next, the scalar product between the two Lagrangian displacements, $\underline{dx_1}$ and $\underline{dx_2}$, is considered.

$$
\begin{aligned}
\underline{dx_1}^T \underline{dx_2} &= \left[\underline{dX_1} + \underline{dX_1}^T grad(\underline{u})\right]^T \left[\underline{dX_2} + \underline{dX_2}^T grad(\underline{u})\right] \\
&= \underline{dX_1}^T \underline{dX_2} + \underline{dX_1}^T \underline{dX_2}^T grad(\underline{u}) + grad(\underline{u})^T \underline{dX_1}\underline{dX_2} + grad(\underline{u})^T \underline{dX_1}\underline{dX_2}^T grad(\underline{u}) \\
&= \underline{dX_1}^T \underline{dX_2} + \underline{dX_1}^T grad(\underline{u})^T \underline{dX_2} + \underline{dX_1}^T grad(\underline{u})\underline{dX_2} + \underline{dX_1}^T grad(\underline{u}) grad(\underline{u})^T \underline{dX_2} \\
&= \underline{dX_1}^T \underline{dX_2} + \underline{dX_1}^T \left[grad(\underline{u}) + grad(\underline{u})^T + grad(\underline{u}) grad(\underline{u})^T\right] \underline{dX_2} \\
&= \underline{dX_1}^T \underline{dX_2} + \underline{dX_1}^T e_{ij} \underline{dX_2}
\end{aligned}
\tag{11}
$$

Green-Lagrange strain tensor [44] is therefore defined as

$$
e_{ij} = \frac{1}{2}\left[\nabla \underline{u} + \nabla^T \underline{u} + \nabla^T \underline{u} \cdot \nabla \underline{u}\right] \tag{12}
$$

However, when strain is in the order of few percents, the non-linear term $\nabla^T \underline{u} \cdot \nabla \underline{u}$ is of the order 10^{-4} and can therefore be neglected. This formulation is called the theory of small strains. In the following, small strains are assumed. Hence,

$$
e_{ij} = \frac{1}{2}\left[\nabla \underline{u} + \nabla^T \underline{u}\right] = \frac{1}{2}\begin{bmatrix} \partial_1 u_1 & \partial_2 u_1 & \partial_3 u_1 \\ \partial_1 u_2 & \partial_2 u_2 & \partial_3 u_2 \\ \partial_1 u_3 & \partial_2 u_3 & \partial_3 u_3 \end{bmatrix} + \frac{1}{2}\begin{bmatrix} \partial_1 u_1 & \partial_1 u_2 & \partial_1 u_3 \\ \partial_2 u_1 & \partial_2 u_2 & \partial_2 u_3 \\ \partial_3 u_1 & \partial_3 u_2 & \partial_3 u_3 \end{bmatrix} = \nabla^{SYM} \underline{u}, \tag{13}
$$

where ∇^{SYM} is a symmetric gradient operator. Since the strain tensor lacks the asymmetric part, the tensor includes only pure shear. Pure rotation is associated with the asymmetric gradient operator.

Moreover, with a given strain tensor there is also an associated strain vector [50] defined by

$$
\underline{e} = \left[\partial_x u_x \quad \partial_y u_y \quad \partial_z u_z \quad \left(\partial_x u_y + \partial_y u_x\right) \quad \left(\partial_y u_z + \partial_z u_y\right) \quad \left(\partial_x u_z + \partial_z u_x\right)\right]^T \tag{14}
$$

The factor 2 is required in order to ensure that strain energies match in tensor and vector formulations.

Finally, it is postulated that for the first approximation, the stress σ_{ij} and strain e_{ij} are obtained by linear mapping from each other. This is expressed in the generalized Hooke's law as

$$
\sigma_{ij} = c_{ijkl} e_{kl} \Leftrightarrow e_{ij} = s_{ijkl} \sigma_{kl}, \tag{15}
$$

where c_{ijkl} and s_{ijkl} are the 4th rank stiffness and compliance tensors, respectively.

4.4 Weak form of the Cauchy equation

The integral formulation, called weak form, forms the basis for the Finite Element Method (FEM). The weak form of the Cauchy equation is needed, because the strong form of the partial differential equation presented in equation (7) does not easily allow for replacing its exact solution by an approximate solution. Having derived the weak form, the problem may be rewritten as a minimization problem. It is now possible to find approximate solutions by restricting the minimization to a finite subspace of basis functions. Now, in order to derive the weak form, the concept of virtual displacement and virtual work is presented next.

Virtual displacement (or test function), $\delta\underline{u}$, is an arbitrary, smooth infinitesimal displacement that satisfies geometrical boundary conditions, i.e. $\delta\underline{u}(\underline{r}) = \underline{0}$ at the Dirichlet boundary, and fulfills equation (13) with $\nabla^{SYM}\delta\underline{u} = \delta\nabla^{SYM}\underline{u} = \delta e_{ij}$.

The weak formulation is based on a variational energy formulation that is obtained by multiplying the equation of motion in equation (7) and the Cauchy lemma in equation (5) by a virtual displacement, integrating them over a volume and the corresponding bounding area, respectively, and summing them. This yields for $\forall\,\delta\underline{u}$

$$\begin{aligned} 0 &= \int_V \delta\underline{u} \bullet \left(\rho\ddot{\underline{u}} - div\sigma_{ij} - \rho\underline{b} \right) dV + \int_{\partial V} \delta\underline{u} \bullet \left(\sigma_{ij}\,\underline{n} - \underline{a}\right) dA \\ &= \int_V \delta\underline{u} \bullet \left(\rho\ddot{\underline{u}} - div\sigma_{ij} - \rho\underline{b} \right) dV + \int_{A_{NEUMANN}} \delta\underline{u} \bullet \sigma_{ij}\,\underline{n}\, dA - \int_{A_{NEUMANN}} \delta\underline{u} \bullet \underline{a}\, dA \end{aligned} \tag{16}$$

Note that the surface integral needs only be taken over the Neumann boundary, since $\delta\underline{u} = \underline{0}$ at the Dirichlet surface.

In the integral formulation of equation (16), only the term $\int_V \delta\underline{u} \bullet div\sigma_{ij}\, dV$ requires closer attention. It can be shown ([44], [50]) that

$$div\left(\sigma_{ij}\delta\underline{u}\right) = \delta\underline{u} \bullet div\sigma_{ij} + \delta\left(\nabla\underline{u}\right)\sigma_{ij} \tag{17}$$

Hence,

$$\int_V \delta\underline{u} \bullet div\sigma_{ij}\, dV = \int_V div\left(\sigma_{ij}\delta\underline{u}\right) dV - \int_V \delta(\nabla\underline{u})\sigma_{ij}\, dV \tag{18}$$

Applying Gauss's law on the first term on the right hand side, we have

$$\begin{aligned}\int_V \delta\underline{u} \bullet div\sigma_{ij}\, dV &= \int_{\partial V} \delta\underline{u} \bullet \sigma_{ij}\,\underline{n}\, dA - \int_V \delta(\nabla\underline{u})\sigma_{ij}\, dV \\ &= \int_{A_{NEUMANN}} \delta\underline{u} \bullet \sigma_{ij}\,\underline{n}\, dA - \int_V \delta(\nabla\underline{u})\sigma_{ij}\, dV\end{aligned}, \tag{19}$$

where the surface integral is once again evaluated only on the Neumann surface. Moreover, since the term $\delta(\nabla\underline{u})\sigma_{ij}$ represents double contraction between a symmetric tensor σ_{ij} and a non-symmetric tensor $\delta(\nabla\underline{u})$, $\nabla\underline{u}$ may be replaced by its symmetric part $\delta(\nabla\underline{u})^{SYM}$ [50]. Hence, the term $\int_V \delta\underline{u} \bullet div\sigma_{ij}\, dV$ may finally be expressed in the form

$$\begin{aligned}\int_V \delta\underline{u} \bullet div\sigma_{ij}\, dV &= \int_{A_{NEUMANN}} \delta\underline{u} \bullet \sigma_{ij}\,\underline{n}\, dA - \int_V \delta(\nabla\underline{u})^{SYM}\sigma_{ij}\, dV \\ &= \int_{A_{NEUMANN}} \delta\underline{u} \bullet \sigma_{ij}\,\underline{n}\, dA - \int_V \delta e_{ij}\sigma_{ij}\, dV\end{aligned}, \tag{20}$$

where equation (13) was used in order to obtain the final form. Integral equation (16) then becomes

$$\begin{aligned}&\int_V \rho\delta\underline{u} \bullet (\ddot{\underline{u}} - \underline{b})\, dV - \int_V \delta\underline{u} \bullet div\sigma_{ij}\, dV + \int_{A_{NEUMANN}} \delta\underline{u} \bullet (\sigma_{ij}\,\underline{n} - \underline{a})\, dA \\ &= \int_V \rho\delta\underline{u} \bullet (\ddot{\underline{u}} - \underline{b})\, dV - \int_{A_{NEUMANN}} \delta\underline{u} \bullet \sigma_{ij}\,\underline{n}\, dA + \int_V \delta e_{ij}\sigma_{ij}\, dV \\ &\quad + \int_{A_{NEUMANN}} \delta\underline{u} \bullet \sigma_{ij}\,\underline{n}\, dA - \int_{A_{NEUMANN}} \delta\underline{u} \bullet \underline{a}\, dA \\ &= \int_V \rho\delta\underline{u} \bullet (\ddot{\underline{u}} - \underline{b})\, dV + \int_V \delta e_{ij}\sigma_{ij}\, dV - \int_{A_{NEUMANN}} \delta\underline{u} \bullet \underline{a}\, dA \\ &= 0\end{aligned} \tag{21}$$

Rearranging yields the weak form

$$\int_V \rho\delta\underline{u} \bullet \ddot{\underline{u}}\, dV + \int_V \delta e_{ij}\sigma_{ij}\, dV = \int_V \rho\delta\underline{u} \bullet \underline{b}\, dV + \int_{A_{NEUMANN}} \delta\underline{u} \bullet \underline{a}\, dA \qquad \forall\delta\underline{u} \tag{22}$$

4.5 Finite element discretization

Equation (22) now states the principle of virtual work: the virtual change in internal energy $\delta W_{internal}$ must be offset by identical external virtual work $\delta W_{external}$. Therefore, $\delta W_{internal} = \delta W_{external}$.

Having now derived the weak form, the final discretized finite element equations are obtained by evaluating the integral in equation (22) over single elements one at time. In such a case $\underline{u}$ becomes displacement at a point within the element. Now, $\underline{u}$ may be approximated by

$$\underline{u}(\underline{x},t) \approx N^u(\underline{x})\underline{u^e}(t) = \sum_i^n N_i^u(\underline{x})\underline{u_i^e}(t), \tag{23}$$

where $N^u(\underline{x}) = \left[N_1^u(\underline{x}) \quad N_2^u(\underline{x}) \quad \cdots \quad N_n^u(\underline{x})\right]$ is the element displacement support, $N_i^u(\underline{x})$ the matrix of shape functions associated with the ith node, n the number of nodes in the element and $\underline{u^e}$ the listing of the nodal displacements for a single element and $\underline{u_i^e}$ the individual nodal displacements. The shape functions in N^u define the basis for the finite-dimensional function space, in which the weak form (22) is approximated. The reader should also note the time-space separation in equation (23). The shape functions are time-independent and depend only upon spatial coordinates. The time dependency is concealed in the nodal displacements.

Moreover, it must be stressed that for the equation (23) to hold, $N_i^u(\underline{x})$ are required to fulfill

$$N_i^u(\underline{x_j}) = \delta_{ij}, \tag{24}$$

where $\underline{x_j}$ is the location of the jth node. This formulation is called the Galerkin's method [43].

For the purpose of evaluating the integral (22), the following operators are defined.

$$\underline{e} = \begin{bmatrix} \partial_x & 0 & 0 \\ 0 & \partial_y & 0 \\ 0 & 0 & \partial_z \\ \partial_y & \partial_x & 0 \\ 0 & \partial_z & \partial_y \\ \partial_z & 0 & \partial_x \end{bmatrix} \underline{u} = S^u \underline{u}\,, \tag{25}$$

which is in fact the matrix form of equation (13). Moreover, the generalized Hooke's law may be expressed in the matrix form by

$$\underline{\sigma} = c\underline{u}\,, \tag{26}$$

with $\underline{\sigma} = \lfloor \sigma_x \quad \sigma_y \quad \sigma_z \quad \sigma_{xy} \quad \sigma_{yz} \quad \sigma_{xz} \rfloor$ being the stress vector and c being the stiffness matrix. Finally, a discrete differential operator B^u is defined that fulfills

$$\underline{e} \approx B^u \underline{u^e}\,, \tag{27}$$

from which it directly follows

$$\underline{e} = S^u \underline{u} \approx S^u N^u \underline{u^e} = B^u \underline{u^e} \Rightarrow B^u = S^u N^u \tag{28}$$

Now, based on these definitions, the individual terms in the integral (22) are evaluated over the element domain Ω by noting that ρ is constant over the domain. Moreover, the time and spatial coordinate arguments for various variables are omitted for the sake of clarity.

$$\int_\Omega \rho \delta \underline{u} \bullet \ddot{\underline{u}}\, dV = \int_\Omega \rho \left(N^u \delta \underline{u^e}\right)^T \left(N^u \ddot{\underline{u^e}}\right) dV = \left(\delta \underline{u^e}\right)^T \left[\rho \int_\Omega \left(N^u\right)^T \left(N^u\right) dV\right] \ddot{\underline{u^e}} \tag{29}$$

$$\begin{aligned} &\int_\Omega \delta e_{ij} \sigma_{ij}\, dV \hat{=} \int_\Omega \left(\delta \underline{e}\right)^T \underline{\sigma}\, dV = \int_\Omega \left(B^u \delta \underline{u^e}\right)^T c\underline{e}\, dV = \left(\delta \underline{u^e}\right)^T \int_\Omega \left(B^u\right)^T c B^u \underline{u^e}\, dV \\ &= \left(\delta \underline{u^e}\right)^T \left[\int_\Omega \left(S^u N^u\right)^T c \left(S^u N^u\right) dV\right] \underline{u^e} \end{aligned} \tag{30}$$

$$\int_\Omega \rho \delta \underline{u} \bullet \underline{b}\, dV = \int_\Omega \rho \left(N^u \delta \underline{u^e}\right)^T \underline{b}\, dV = \left(\delta \underline{u^e}\right)^T \left[\rho \int_\Omega \left(N^u\right)^T \underline{b}\, dV\right] \tag{31}$$

$$\int_{\partial\Omega_{NEUMANN}} \delta\underline{u} \bullet \underline{a}\, dA = \int_{\partial\Omega_{NEUMANN}} \left(N^u \delta\underline{u^e}\right)^T \underline{a}\, dA = \left(\delta\underline{u^e}\right)^T \int_{\partial\Omega_{NEUMANN}} \left(N^u\right)^T \underline{a}\, dA \tag{32}$$

Hence, the integral (22) may now be given in a discrete form that depends on the nodal displacements and element support functions.

$$\begin{aligned} &\left(\delta\underline{u^e}\right)^T \left[\rho \int_\Omega \left(N^u\right)^T \left(N^u\right) dV\right] \underline{\ddot{u}^e} + \left(\delta\underline{u^e}\right)^T \left[\int_\Omega \left(S^u N^u\right)^T c\left(S^u N^u\right) dV\right] \underline{u^e} \\ &= \left(\delta\underline{u^e}\right)^T \left[\rho \int_\Omega \left(N^u\right)^T \underline{b}\, dV\right] + \left(\delta\underline{u^e}\right)^T \int_{\partial\Omega_{NEUMANN}} \left(N^u\right)^T \underline{a}\, dA \end{aligned} \qquad \forall\, \delta\underline{u^e} \tag{33}$$

Since equation (33) must hold for $\forall\, \delta\underline{u^e}$, for a single element it can be written that (with an addition of damping)

$$M^e \underline{\ddot{u}^e}(t) + C^e \underline{\dot{u}^e}(t) + K^e \underline{u^e}(t) = \underline{F_V^e} + \underline{F_P^e}, \tag{34}$$

where

$$M^e = \rho \int_{Element} \left(N^u\right)^T N^u\, dV \qquad \text{Element mass matrix} \tag{35}$$

$$C^e \qquad \text{Element damping matrix. See below.} \tag{36}$$

$$K^e = \int_{Element} \left(S^u N^u\right)^T c\left(S^u N^u\right) dV \qquad \text{Element stiffness matrix} \tag{37}$$

$$\underline{F_V^e} = \rho \int_V \left(N^u\right)^T \underline{b(t)}\, dV \qquad \text{Force vector due to volume loads} \tag{38}$$

$$\underline{F_P^e} = \int_{A_{NEUMANN}} \left(N^u\right)^T \underline{a(t)}\, dA \qquad \text{Force vector due to external pressure} \tag{39}$$

The general form of the damping matrix C^e was not derived above due to the inherent problems associated with the underlying theory. Moreover, difficulties arise in trying to express damping matrix in a numerical form. Therefore, an often used form for the damping matrix is

$$C^e = \beta_1 M^e + \beta_2 K^e, \tag{40}$$

which is called the Rayleigh structural damping matrix with damping parameters β_1 and β_2. The Rayleigh form for damping has no physical justification, but is often utilized due to the lack of better description. The damping parameters may be optimized with respect to measured data.

As a further note, in harmonic analysis $\underline{u^e}$ may expressed by $\underline{u^e} = \underline{u_0^e} e^{i\omega t}$, from which it formally follows (assuming harmonically varying loads also)

$$\left[-\omega^2 M^e + i\omega C^e + K^e\right]\underline{u_0^e} = \underline{F_V^e} + \underline{F_P^e} \Leftrightarrow \underline{u_0^e} = \left[-\omega^2 M^e + i\omega C^e + K^e\right]^{-1}\left[\underline{F_V^e} + \underline{F_P^e}\right]. \qquad (41)$$

When systems containing more elements are analyzed, the matrix definitions introduced in equations (35) - (39) are utilized to compile the total system matrices for the use in equation (34). In such a case, $\underline{u^e}$ transforms to a listing of nodal displacements of all the nodes in the model. The system of equations in (34) also carries information on the applied boundary conditions.

5. FINITE ELEMENT EAR MODEL

5.1 Overview

This chapter describes the process of building a FE model of the ear. The purpose of the model is to provide meaningful order-of-magnitude estimates on the ear behavior for the ECE development. Ultimately, the aim is to be able to model the transmission loss occurring in the mechanical transfer path.

The major parts included in the model are the tympanic canal and the associated cartilaginous and bony parts, tympanic membrane as well as the ossicles. This chapter introduces the model parts and describes the various approximations made in the model. In addition, a thorough discussion on the prior art in the field of the ear FE-modeling is given. This also includes a summary on the general problems associated with the biomechanical modeling.

Finally, the model is validated against published data. The chapter closes with the discussion on the results obtained.

5.2 About biomechanical modeling

Modeling of biological systems is especially challenging due to the complex geometries and processes associated with the systems as well as because of the lack of data on the material parameters. And even if the data were available, they are often controversial or the error margins are such significant that the modeling accuracy becomes questionable. Moreover, in biological systems anisotropy and non-homogeneity play such a significant role that the parameters are often educated guesses or heavy approximations.

Fortunately, a good number of publications is available on the middle ear modeling. The publications used in the development work of the current ear model are reviewed in the section 5.3. These sources provide the material parameters required for the model development, but also reveal the wide spread of data. In this work, a set of consensus parameters was searched and used in the simulations. The parameter considerations are discussed in the section 5.5.

In the literature review, no publications were found, in which the middle ear mechanics would have been combined with the external ear structure. The publications found concentrate on considering the middle ear (tympanic membrane, tympanic cavity and the

ossicles), but none couples this with the tympanic canal structure. In the current work, this coupling between the hearing organs and the skin-cartilage-bone system protecting the organs is of the greatest importance.

This brings the discussion to an important question on how to model the skin covering the tympanic canal. Gladilin [29] gives a fine discussion on the problems associated with the skin modeling. Gladilin states that, in general, the skin exhibits non-homogenous, anisotropic, quasi-incompressible and non-linear plastic-viscoelastic material properties. Non-homogeneity and anisotropy can be understood by noting that the skin has four distinct layers with different compositions. Moreover, the skin consists mostly of collagen fibers running in different directions depending upon the layer. This fibric behavior results in anisotropy.

Skin consists of compressible substances, such as collagen, and incompressible materials, such as water. This mix is the reason for quasi-incompressibility. In the FE-analysis this behavior can be taken into account by adjusting the Poisson's ratio.

The generalized Hooke's law assumes that the stress-strain relationship is linear. This assumption becomes invalid under high strains and skin makes no exception in this. However, the strains generally modeled are such small (order of magnitude 10^{-3} or 10^{-4}) that the non-linear effects can be neglected.

Finally, plasticity and viscoelasticity are characteristics that will not be considered in the current model, but are summarized here for reference. Plasticity of the material refers to the irreversible processes and hysteresis. In practice, this means that if the material has plastic properties, the material does not return to its original state after being subjected to high strain, but deforms permanently. According to Gladilin, the behavior is difficult to take into account, since currently too little is known about the plastic behavior of soft tissues. Viscoelasticity, on the other hand, means that the response of the material is dependent upon the loading history. This can be formulated by writing

$$\sigma_{ij} = \sigma_{ij}(\dot{e}_{ij}, e_{ij}), \tag{42}$$

which means that stiffness is dependent upon the current strain and its rate of change. Viscosity and elasticity are properties of fluids and solids, respectively, and hence it is natural that a substance consisting of fluids and solids, such as skin, follows a viscoelastic

behavior. Taking the viscoelastic effects into account requires knowledge on the relaxation constant of the material, which again may be difficult to measure or predict.

In conclusion, having gone through all the considerations summarized above, Gladilin states that in tissue modeling, the reasonable assumptions are piecewise homogeneity, isotropy, quasi-incompressibility and non-linearity. However, in the current work an additional assumption of skin being linear is made.

5.3 Studies reviewed

Wada & Metoki & Kobayashi. 1992, [70]. The model presented in this paper is a complete 3D-model of the middle ear. The geometry of the membrane and ossicles is obtained from the accurate measurements by Kirikae [41]. The membrane in the model has a varying thickness (97-232 μm) and isotropic material parameters. The Young's modulus in pars flaccida is taken to be the third of that in pars tensa.

The grounding of the membrane is done with linear and torsional springs that represent the tympanic annulus and Notch of Rivinus. However, spring constants used are somewhat low, which leads to unexpectedly high displacement values at the outer boundary of the membrane.

To further simplify the analysis, Wada et al. assume a fixed rotational axis for the ossicles. They do, however, state that this contradicts with observations. They acknowledge that the correct approach would be to include the ligaments and muscles supporting the ossicles in the model.

For the purpose of validating the current FE-model, Wada et al. provide displacement patterns for the tympanic membrane at 996 Hz and 1924 Hz. These frequencies correspond to the first two membrane resonances in their model. They note that the patterns compare well with published measured results and, hence, it will be useful to compare their results to the results obtained from the current FE-model.

Prendergast & Ferris & Rice & Blayney. 1997, [57]. The model presented in this paper was developed for studying the function of an ossicles prosthesis. The model geometry is taken from [41] and, hence, the work closely follows the work by Wada et al. [70] In addition to the membrane and ossicles geometry, Prendergast et al. also include the tympanic canal in the analysis. The geometry for the canal is extracted from nuclear

magnetic resonance (NMR) imaging of the ear. In contrast with [70], pars tensa has orthotropic mechanical properties.

Hudde & Engel. 1998, [35] [36] [37]. This series of papers presents, how the complete conduction path from the concha to the cochlea is modeled as a chain of two-port models. The study is comprehensive and they consistently state the various assumptions, simplifications and restrictions included in their model. The data presented in this paper forms the basis for defining the ossicles and cochlear load for the current ear FE model.

Abel & Lord. 2001, [1]. The authors claim that the defects of incus account for 59% of conductive hearing loss cases. Most often, incus pathologies are corrected in surgery by replacing ossicles by a rod that rigidly couples tympanic membrane to the oval window. However, the lever action of ossicles is thereby lost. Now, the authors have previously shown that by replacing only the incus, hearing can be restored within 10 dB. They set a FE-simulation to study, how the replacement ought to be done and how the incus should be attached to malleus and stapes.

The geometry for the ossicles is obtained from a high-resolution NMR imaging. The tympanic membrane is defined as a curved surface and is assumed to be uniform in thickness (100 μm). The membrane is defined as having orthotropic mechanical parameters. However, the Young's modulus values used in their model are considerably higher than in other recent studies.

The cochlear load was not modeled in this work. Moreover, no tympanic annulus is included in the model, but the membrane rigidly fixed at the boundaries. As a result, the membrane, as well as the stapes, has a resonance at 1.5 kHz. Generally, the resonance is quoted to occur at 800-1000 Hz [27] [28] [71]. Moreover, their model shows growing displacement values above 8 kHz, which behavior is not observable in typical measurements results found in the literature.

Koike & Wada & Kobayashi. 2002, [42]. This study continues the work done in [70]. Additional features, such as three ligaments and two muscles supporting the ossicles are added. This removes the requirement to define a fixed rotational axis for the ossicles and, hence, enables making a more realistic model of the middle ear function. Moreover, various cavities, such as the external meatus and tympanic cavity, are added in order to be able to perform coupled-field analyses.

In addition to introducing a more realistic model, the paper presents a comprehensive set of mechanical parameters for others to evaluate and use. For instance, the Young's module for ligaments are calibrated by comparing simulations and measurements. The authors, however, note that the parameters obtained in this manner do not necessarily represent true physical parameters, but are the best fit. Nevertheless, the presented parameter set provides a good starting point for the current modeling work.

In general, it can be said the model presented in the paper is state-of-the-art. With realistic thickness distribution across the membrane, joints between the ossicles, cochlear damping and air-filled cavities, this model is one of the most comprehensive models presented in the literature.

Moreover, the paper includes a plethora of insights that can be utilized in the current modeling work. Firstly, Koike et al. modify the connection between the tympanic membrane and the malleus handle to resemble more closely the realistic situation. In other words, instead of defining rigid connection, they define a loose connection. However, Koike et al. find that this partial uncoupling affects neither the displacement distribution nor amplitudes across the membrane significantly. Hence, it can be neglected. Penultimately, Koike et al. find that defining anisotropic mechanical parameters for the tympanic membrane is not necessary. The model produces reasonably accurate results with isotropic material definitions. Finally, Koike et al. use Rayleigh damping to model damping in various parts of the model and present the calibrated damping parameters.

Sun & Gan & Chang & Dormer. 2002, [66]. Geometry for this modeling work was obtained by scanning 600 20-μm histological sections from the temporal bone. The result is a very accurate geometric representation of the middle ear with ligaments, muscles and proper joints between ossicles. However, their model still lacks air-filled cavities

Sun et al. also make some insightful statements about models. They state that since the strains in the membrane are in the order of 10^{-4}, the first order Hookean representation holds for elasticity. It can therefore be also concluded that at these strain levels the second order term in the Green-Lagrange strain tensor vanishes and, hence, no geometrical non-linearity is present.

Sun et al. are (probably) also the first to define tympanic annulus as a material, not in terms of springs as in earlier studies. They define the annulus dimensions and present

isotropic mechanical parameters for the material. For the tympanic membrane Sun et al. define orthotropic parameters for pars tensa and isotropic for pars flaccida, as was done in [1] and [57].

In general, the work presented in the paper is a solid modeling work with good documentation of the model validation process. Moreover, they provide meaningful data for others to repeat their work and to support further research.

Gan & Feng & Sun. 2004, [28]. Geometry for the Gan's model is obtained by similar approach as in [66], but they use another temporal bone. However, in contrast to [66], the external acoustic meatus as well as tympanic cavity are added to the model.

Material parameters used in the modeling work are collected from the previous art and also the model validation was done with respect to the same data as in [66].

The model presented by Gan et al. is yet another state-of-the-art ear model with fine geometrical description of the ear. Moreover, detailed considerations are given on how uncertainties in the mechanical parameters affect the simulation results.

5.4 Model overview

This section gives a brief overview of the general features of the ear model. Specific issues, such as material parameters and load exerted by the ossicles on the tympanic membrane will be discussed later in detail.

Figure 8 shows the ear model from two different angles without the bone surrounding the tympanic canal.

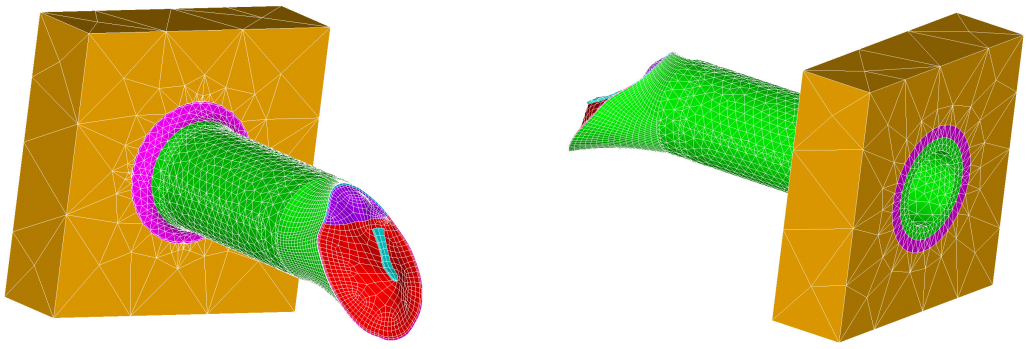

Figure 8. Ear model from two different angles without bone. Dark yellow – fat, light violet – cartilage, green – skin, blue – notch of rivinus, dark violet – pars flaccida, red – pars tensa, violet surrounding the pars tensa – tympanic annulus, turquoise – handle of malleus. Note that the handle covers the manubrium and, hence, it cannot be seen.

Figure 8 shows the features discussed in the anatomy section. The lateral part of the tympanic canal is supported by a 1-mm cartilage layer (light violet). This layer is in turn surrounded by fat located between head skin and skull.

In the bony part the skin (green) becomes thinner (0.2 mm). The bony part is surrounded by bone that is, however, not shown in figure 8 for the sake of clarity. The complete model with the bone is shown in figure 9.

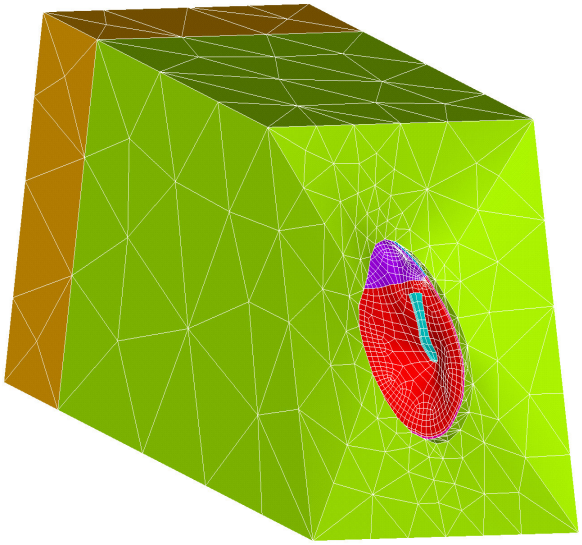

Figure 9. Ear model with bone (dark green). Tympanic membrane and its sections are visible as well.

The tympanic canal is modeled simply as a tube. The model is a crude simplification of the true, s-shaped canal. It is still believed that this approximation will provide valuable order-of-magnitude estimates on the behavior of the mechanical transfer path. However, Koike et al. [42] have shown that if meaningful pressure response is required, the correct canal shape is essential.

Finally, the connection between the ear canal skin and the tympanic membrane is considered. The point of the attachment is shown in figure 10.

The tympanic canal skin forms the lateral layer of the membrane. Hence, there is a strong connection between the skin and membrane. However, the skin also connects to the tympanic annulus, which in turn is fixed to the bone. Now, the canal skin has 2 element layers. As figure 10 shows, the tympanic annulus and the Notch of Rivinus are only one layer wide. Therefore, the outer element layer of the skin connects to the annulus or the

Notch of Rivinus and the inner layer to either pars tensa or pars flaccida. This choice mimics the natural situation sufficiently and guarantees that the skin vibrations, if any, are carried to the membrane. Moreover, the tympanic membrane is then also properly grounded to the bone.

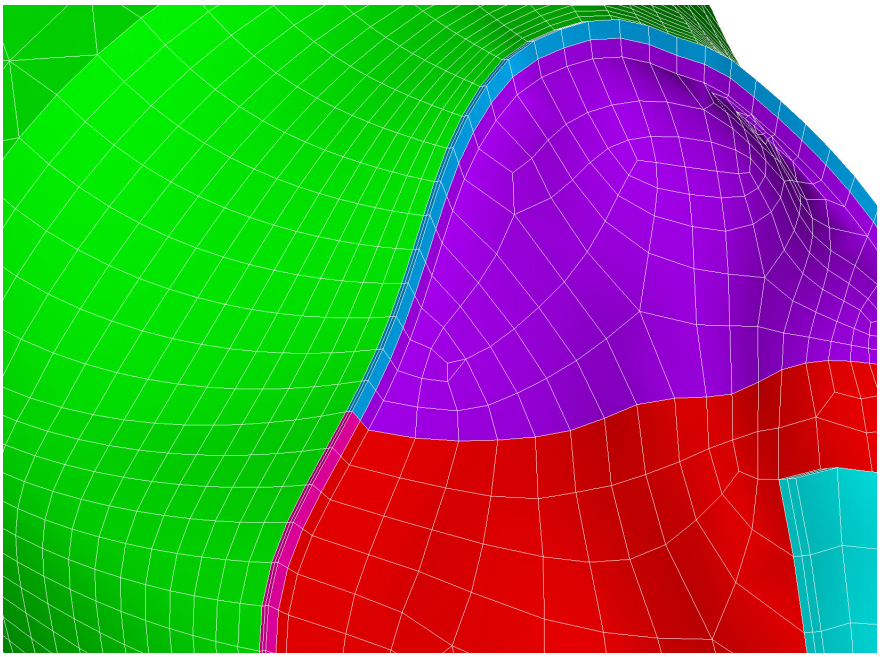

Figure 10. Eardrum attachment to the ear canal skin. Tympanic annulus and Notch of Rivinus are clearly visible.

The reference [66] quotes 0.2 mm for both, the tympanic annulus thickness and width. In the current model, the width is only half of that, 0.1 mm. Moreover, the thickness is more than halved down to 75 μm. This is due to the choice to model the tympanic membrane as having a uniform thickness of 75 μm. The membrane geometry was kindly provided by professor Robert Funnell (McGill University, Canada).

5.5 Material parameters

Table 1 summarizes the various material properties used in the ear FE-model. The table gives densities, Young's module, Poisson ratios as well as the origin of the data. A brief discussion on the parameters follows the table.

Material	Density ρ, $kg \cdot m^{-3}$	Young's modulus, MPa	Poisson ratio	Source(s)
Manubrium	1000	4700	0.3	[28]
Pars Flaccida	1200	11	0.3	[28], [42], [57]
Pars Tensa	1200	30	0.3	[28], [42], [57], [70]
Notch of Rivinus	1200	0.6	0.3	[28]
Tympanic Annulus	1200	0.6	0.3	[27], [28]
Ear canal skin	1200	0.1	0.45	[24], [29]
Fat	900	0.01	0.45	[24], [29]
Cartilage	1100	5	0.4	[24]
Bone	1600	17000	0.4	[20], [24]
Handle of malleus	0-24520	4700	0.3	-

Table 1. Material properties for the ear model.

Manubrium. Only one used source, [28], defines the manubrium as a separate section on the membrane.

Pars flaccida. Various sources quote isotropic properties with Young's modulus around 10 MPa. However, reference [1] uses orthotropic properties with radial and circumferential Young's module of 45.6 and 20 MPa, respectively. Sources [1] and [28] quote the density of 1200 $kg \cdot m^{-3}$ for pars flaccida and tensa.

Pars tensa. Sources [70] and [42] give 33.4 MPa for pars tensa Young's modulus. Reference [28] proposes orthotropic properties with radial and circumferential module of 35 and 20 MPa, respectively. Moreover, reference [1] quotes radial and tangential Young's module of 85.7 and 48 MPa, respectively. However, since the source [42] states that isotropic properties yield sufficient accuracy, no anisotropic properties were defined.

Moreover, the reference [66] claims that the Poisson ratio has no significant effect on the middle ear behavior and uses therefore a generic value of 0.3 for the ratio. However, the source [1] quotes 0.35 and 0.43 for pars tensa and flaccida, respectively.

Skin. The reference [29] quotes Young's module of 0.5 and 0.09 MPa for skin depending upon the source. Skin density varies between 1093 - 1190 $kg \cdot m^{-3}$ according to [24].

Fat. The source [29] gives fat Young's module of 1 and 5 kPa depending upon the original source. The reference [24] states the density of fat (breast) to lie between 917 - 939 $kg \cdot m^{-3}$.

Poisson ratio for skin and fat lies between 0.40 – 0.49 according to [29]. Moreover, it is known that higher water content in the tissue results in higher ratio. FEM may have problems with solution accuracy, when the ratio approaches 0.5. When this happens, one should utilize mixed formulations that consider pressure as an independent variable in addition to the displacement DOFs. In practice, however, it was noticed that varying the ratio in the model did not have a decisive effect on the results.

Cartilage. Density and Young's modulus were obtained from [24] for nasal cartilage. In general, the source [24] quotes values ranging from 0.32 to 5.83 MPa.

Bone. Density for bone is obtained from the sources [20] and [24]. According to [20], density is 1600 - 1700 $kg \cdot m^{-3}$. Young's module vary between 6.9 and 18.4 GPa in [24] for cortical bone. In the source [20], 17 GPa is given parallel to the axis of long bones. However, the Young's modulus in bone is in any case orders of magnitude greater than in other materials and, hence, its exact value plays insignificant role.

Poisson ratio for bone and cartilage ranges from 0.12 to 0.62 and from 0.18 to 0.47, respectively. The values are given in [24]. Moreover, the ratios are heavily dependent upon the bone direction.

Rayleigh damping factor β_1. In the current study, this parameter is set to zero. However, for instance the reference [42] uses $\beta_1 = 260\ s^{-1}$.

Rayleigh damping factor β_2. The literature gives values 0.37e-4 s, 0.75e-4 s and 1e-4 s in [57], [28] and [66], respectively. The value of 0.5e-4 s is used in the current study.

Handle of malleus. Handle of malleus represents added mass on the tympanic membrane due to the ossicles and cochlear load. The added mass is frequency dependent and, hence, the density ranges from 0 to 24520 $kg \cdot m^{-3}$. Other properties are the same as in the manubrium.

5.6 Ossicles load

In the early phase of the modeling work, a decision was made not to try to model the ossicles in detail. This was due to two reasons. Firstly, modeling the exact middle ear

function is by no means necessary for examining the ear behavior under the ECE excitation. Secondly, modeling the ossicles with a correct geometry including joints, ligaments and muscles is a demanding task and is not within the scope of this study. Moreover, today the geometries are often obtained by the means of NMR imaging, which was not possible in this study.

Having the correct loading on the membrane by the ossicles is important in order to obtain the correct frequency response. Therefore, the ossicles are modeled as a one-mass model as added mass and spring-dampers.

Hudde et al. provide a lumped parameter model, which allows for finding the mechanical impedance of the ossicles-cochlea system [35] [36] [37]. Their model is quoted to apply only up to 5-6 kHz. However, in the lack of better description of the impedance, the same model is used in this work up to 8 kHz. The somewhat modified model is shown in figure 11.

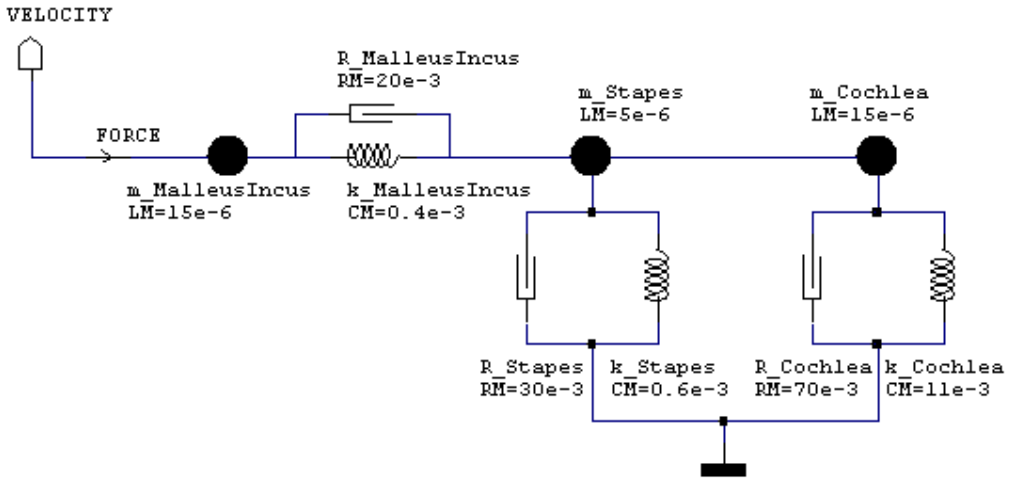

Figure 11. Lumped parameter model of the middle ear conduction path. Model is presented in mobility analogy with force being the flow and velocity the potential quantity. In the figure, LM denotes the mass in kg, RM damping in Ns/m and CM compliance in m/N. Note that this model omits the mechanical path, i.e. bone conduction.

The most notable difference between the model presented here and by Hudde et al. is the value of *k_MalleusIncus*, which represents the stiffness of the joint between the incus and stapes. Hudde et al. gives CM=$3 \cdot 10^{-3}$ mN^{-1} for the joint. However, it was noticed that it was necessary to increase the stiffness of the joint in order to match the tympanic membrane low frequency response with the published data. The need for this correction may indicate that the membrane model itself has too low stiffness.

Now, mechanical impedance, Z_{mech}, of a given system is defined as

$$Z_{mech}(i\omega) = \frac{F(i\omega)}{v(i\omega)}. \tag{43}$$

Based on the definition, figure 12 gives the mechanical impedance of the equivalent circuit in figure 11 in terms of amplitude and phase angle.

Figure 12. Complex mechanical impedance of the ossicles and cochlea.

Now, in the FE-model, the load is taken into account as a one-dimensional oscillator. For a simple harmonic oscillator [53] mechanical impedance is written as

$$Z_{mech}(i\omega) = \frac{F(i\omega)}{v(i\omega)} = R_{mech} + i \cdot \left(m \cdot \omega - \frac{k}{\omega} \right), \tag{44}$$

where R_{mech} is damping, m added mass and k spring constant. Knowing the impedance allows then finding the damping as well as added mass and spring constant as a function of frequency. These are plotted in figures 13 and 14, respectively.

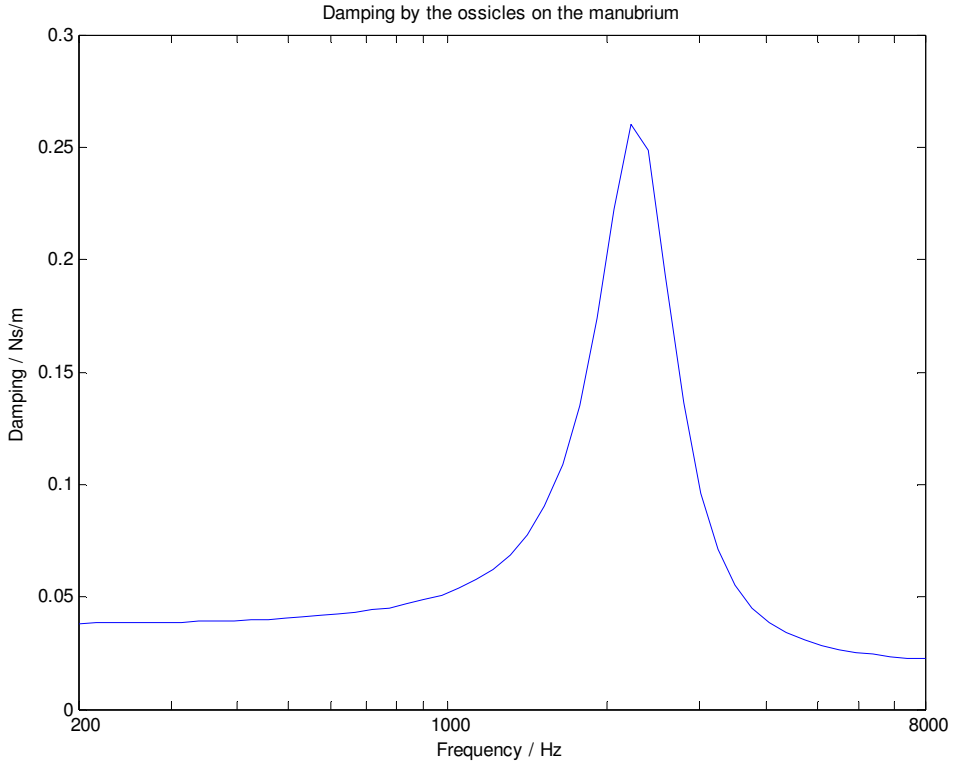

Figure 13. Damping as a function of frequency.

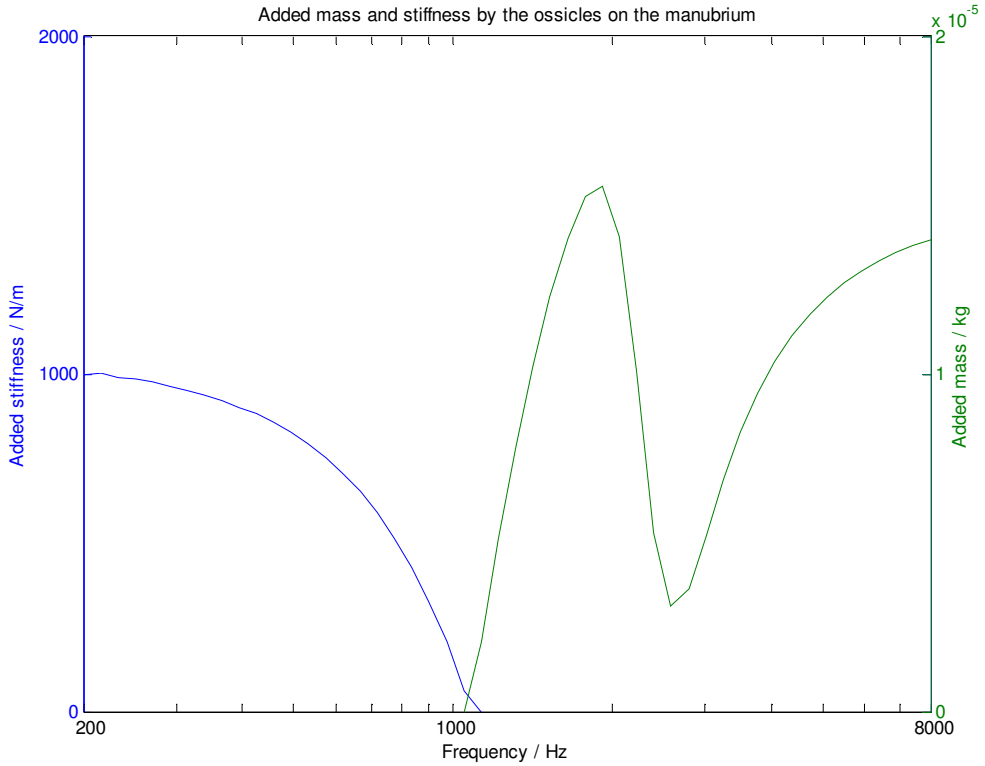

Figure 14. Added mass and spring constant as a function of frequency.

Finally, figure 15 shows the approach in the FE-model. On the manubrium, there is a 200-µm thick layer of stiff material, of which density is varied as a function frequency. Moreover, the same figure shows the spring-damper elements that are normal to the manubrium surface. The elements are defined by two nodes, one is on the added mass volume surface and the other 100 µm to the normal direction. In total, there are 27 spring-damper elements on the surface.

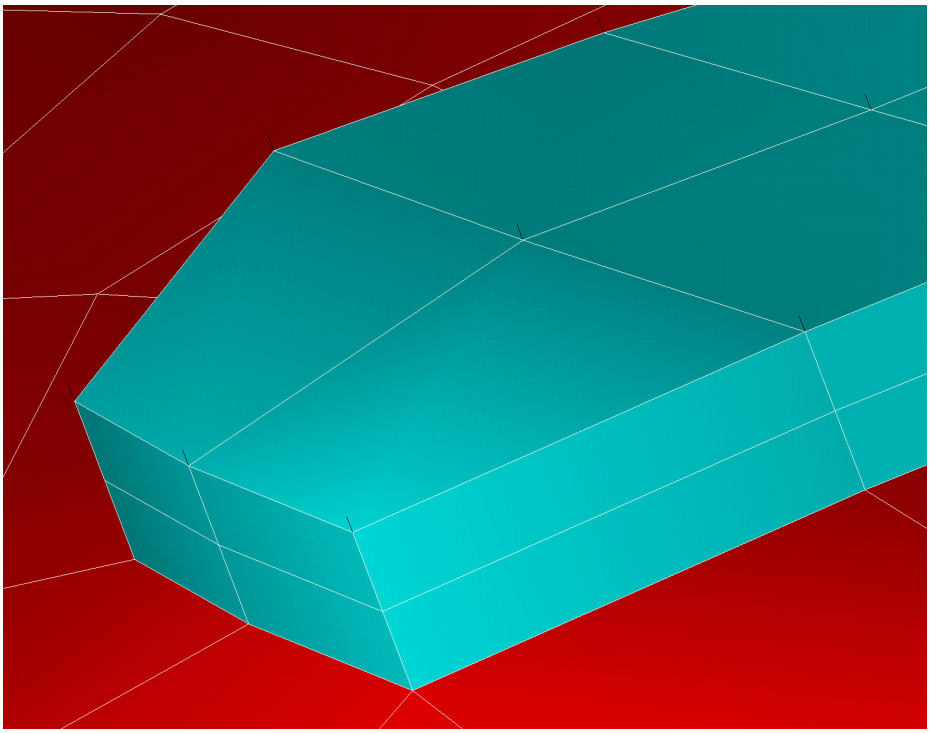

Figure 15. Head of the handle of malleus (blue) showing the spring-damper elements (black). Pars tensa is shown in red.

5.7 Model verification

The verification of the ear model is divided in two parts. The first phase consists of comparing the model predictions with published data. In the second phase, the model results will be compared with the measured data. The reason for this approach is that there is no published data on the properties of such a mechanical transfer path as modeled in this work. Therefore, these predictions can be verified only after there are measured data. On the other hand, much has been published on the tympanic membrane behavior under different types of excitation. The current model is now compared with respect to these data.

The data sets used in the comparison originate from Nishihara et al. [66] and Gan et al. [28]. In their measurements, umbo displacement has been observed under constant harmonic pressure at different frequencies in order to obtain the frequency response of the membrane. The both data sets represent open cavity situations, which means that the effects arising from the tympanic canal and cavity volumes have been removed by opening the corresponding cavities.

Open cavity is desirable in checking the model validity, since the cavities affect the membrane behavior significantly [42], but are at the same time difficult to take into account. The cavity effects can successfully be modeled only if the cavity geometry is available with sufficient accuracy. This is because the cavity eigenfrequencies depend upon the geometry.

In FE-modeling, the tympanic canal can successfully be taken into account by extracting the geometry with, for instance, NMR imaging [28]. The canal walls may also be assumed rigid, which further simplifies the analysis. However, the tympanic cavity has much more complicated geometry, which makes the geometry extraction and especially the meshing problematic. Moreover, the mastoid air cells covering parts of the cavity are elastic and, hence, the cavity walls are not rigid. The same cells are also able to vary the cavity volume, which affects the eigenfrequencies.

In conclusion, the model validation is more accurate under the open cavity situation. The choice of the method of validation is further justified by noting that in the current work, the aim is to obtain estimates on ear mechanics, not on the pressure path. However, the two domains are strongly coupled at the membrane area and, hence, a refinement of the model might include the addition of air in the canal. In such a case, the true canal geometry should be scanned and attached to the current membrane model.

In the FE-model, the open cavity behavior is achieved by modeling the ear in vacuum. This is advantageous, since by neglecting air, the element count and, hence, computational time required can significantly be reduced. In vacuum conditions, pressure load corresponding to a certain SPL level is directly applied on the membrane area. The same principle has also been used in [66] and [28].

The membrane and ossicles model is verified by applying 90 dB rms (0.632 Pa_{rms}) on the membrane and observing the umbo displacement (peak) in the piston-like direction. A

harmonic analysis ranging from 200 Hz to 8 kHz is run. Figure 16 shows the simulation results and the comparison data.

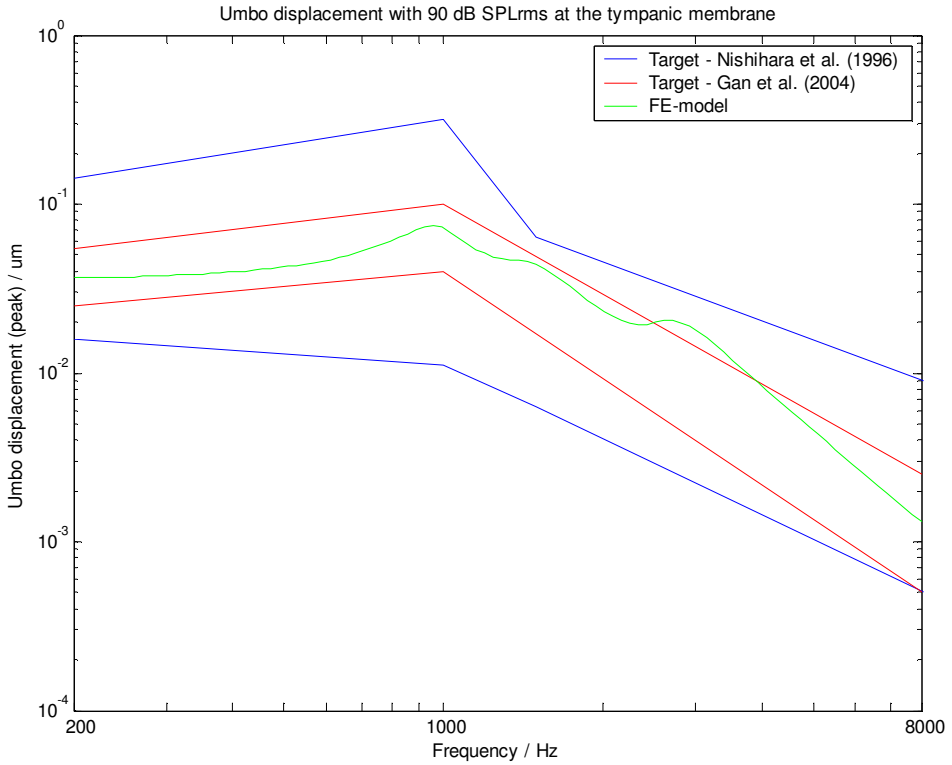

Figure 16. Response of the model, when 90 dB SPL rms is applied on the lateral side of the tympanic membrane. Target data by Nishihara et al. can be found in [66] and the data by Gan et al. in [28]. The umbo displacement is given in the projected piston-like direction, i.e. the normal of the average membrane plane. Note that the target graphs are only crude envelopes of the real measured data.

As figure 16 shows, the current model compares well with the measured data. The important features of the response are all captured in the current model. These include the fairly flat response up to the first resonance, the location of the first resonance and the decreasing response after the first resonance. Moreover, in the original data by Nishihara et al. a minor resonance, or at least evening of the response, is observable at 2 kHz. This might correspond to the small resonance observed below 2 kHz in the current model. Also Wada et al. [70] report resonance at 2 kHz in their FE-model.

The resonance visible at 3 kHz is due to the cochlear load, but no published data shows it being as strong as now seen in the modeled response. Additional damping at the cochlea could even the resonance out. Moreover, the current understanding is that the cochlear load is damping dominated [28], which would justify the added damping. However, no

damping was added, since the response already now fits well within the published boundaries.

The model accuracy diminishes at high frequencies (above 4 kHz). Although the absolute response still remains well within the given target range, the slope is erroneous. The response decreases too rapidly, which implies that there is too much mass in the system. However, although an attempt was made to correct the situation by decreasing mass in the ossicles model, it only resulted in resonances shifting to higher frequencies. It was then considered more important to have the first resonance at the correct frequency and let the small error remain in the high-frequency response. The error may imply that the simple ossicles model truly becomes invalid at higher frequencies as originally noted by Hudde et al.

Finally, the tympanic membrane vibration mode is compared with published data. Figure 17 shows the membrane displacement distribution under 508-Hz excitation.

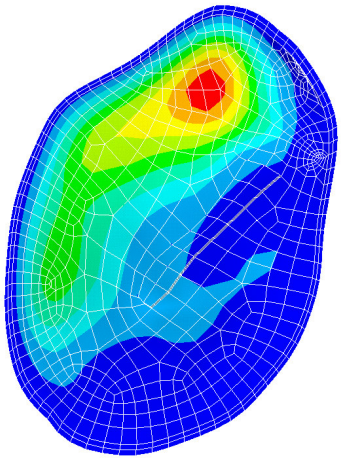

Figure 17. Tympanic membrane displacement distribution with 90 dB SPL rms at 508 Hz applied on the lateral side of the membrane. The maximum displacement is 40 nm. Red and blue denote the greatest and smallest displacements, respectively.

The overall shape of the distribution compares qualitatively with that presented in [42]. The simulation can be expected to give somewhat different results than observed, since in a real case the pressure distribution along the membrane is not constant, but varies spatially. Still, this comparison can be considered as further evidence that the model is capable of giving meaningful predictions.

5.8 Model predictions

The successful validation of the model allows for using the model for the ECE function prediction. In the model, the ECE excitation is applied as a displacement boundary condition over the length of 5 mm in the lateral end of the tympanic canal. The excitation is applied over the whole circumference and the transmission loss for all three excitation types, radial, axial and tangential are modeled. Figure 18 gives the TL in decibels for different excitation types.

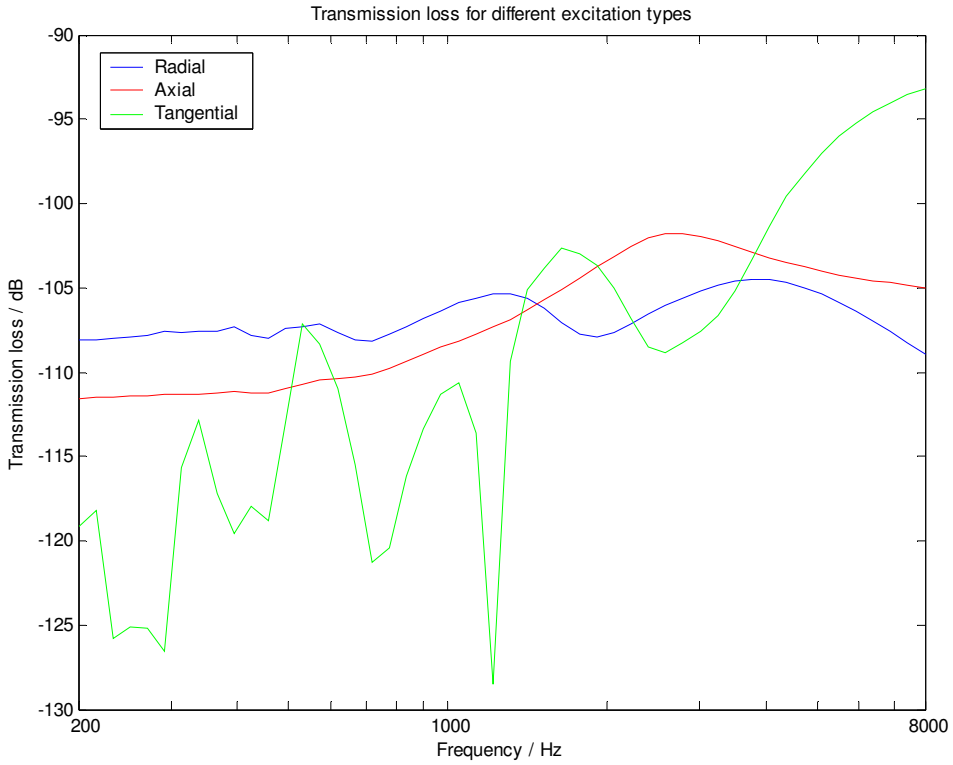

Figure 18. Amplitude transmission loss for radial, axial and circumferential excitations. The results show that no type is better than the other. The results are for the mechanical parameter set presented in table 1.

Figure 18 shows that based on the model predictions, the ECE cannot work as hypothesized. The transmission loss of 100 dB means in practice that in order to have 0.1-µm tympanic membrane displacement, the ECE needs to vibrate with a 1-cm amplitude. Clearly, this is not acceptable.

The uncertainties in the model include boundary conditions and the validity of the skin model. The model boundary conditions (BCs) include the ECE excitation as well as the rigid body motion prevention. The results show that no ECE excitation type is transmitted better than other and, hence, also none combination of the excitations. Therefore, the problem cannot be appointed for the excitation. The rigid body motion has been prevented

by fixing the outer boundaries of the bone. An attempt was made to improve the transmission by modifying these BCs. However, it turns out that the vibrations caused by the ECE diminish fairly quickly in the bone and, hence, modifying the BCs at the outer bone boundaries has no effect on the results.

The mechanical parameters for skin and cartilage were also varied, since they are believed to affect the transmission the most. For cartilage, the Young's modulus was varied from 0.5 MPa to 5 MPa with no significant effect on the transmission properties. For skin, the Young's modulus as well as Poisson's ratio was varied. By varying the Young's modulus in the range from 0.05 MPa to 0.5 MPa and Poisson's ratio from 0.4 to 0.49, approximately 10 dB variations were observed in the transmission characteristics as compared to the data presented in figure 18. These simulations were made only for radial excitation and at a few point-frequencies in order to get fast estimates on the effect of the variations.

Finally, it should be stressed that modifications in modeling the skin-bone contact might lead to different results. In the model, the skin-bone boundary was defined non-sliding by coupling the nodes. However, the fourth layer of skin, fascia, actually forms a sliding contact with the underlying bone [29]. Assuming a rigid connection may lead to unnecessarily large energy flow to the bone at the expense of reduced vibration amplitude in the skin layer.

In conclusion, the results obtained from the ear model show that the ECE transmission losses are significant, since vibrations diminish quickly in the soft tissue surrounding tympanic canal. Moreover, the results also include that due to the various assumptions made, the model must validated by direct measurements.

6. PIEZOELECTRICS

6.1 Piezoelectricity

Piezoelectricity can be characterized as electric polarization produced by mechanical strain in crystals belonging to certain classes, the polarization being proportional to the strain and changing sign with it. This effect is known as direct piezoelectric effect. The opposite, strain produced by polarization, is called inverse piezoelectric effect. Curie brothers discovered the effects in 1880 and 1881, respectively. [16]

Piezoelectric effect rises from the symmetries possessed by crystals. Crystals can be classified into 32 crystallographic point groups according to the sets of symmetry operations defined about a point. Now, there are 11 point groups that remain invariant as acted upon by inversion. Formally, this leads to all third rank tensors, such as piezoelectric tensor, being zero tensors. Moreover, there is a single point group, symmetry group 432, without inversion symmetry but with such other symmetry properties that all its third rank tensor properties are zero. Hence, there are 32 - 11 - 1 = 20 out of 32 crystallographic point groups that show piezoelectricity. [15] [55]

While some naturally occurring crystals as well as some polymers show piezoelectricity, the most commercially exploited piezoelectric materials are synthetic polycrystalline ferroelectric ceramics [69]. These ceramics are manufactured, as their name suggest, by starting from solid powders that are milled into appropriate particle sizes and then mixed. By applying a correct series of heat treatments and by adding an appropriate binding agent, the final outcome is a polycrystalline that is a collection of crystal domains with random polarization directions. Although the polycrystalline does not show net polarization initially, domains can be turned under heavy electric field and elevated temperature so that the ceramic starts to show net polarization and approximate single crystal behavior. A fine description of the complete manufacturing process is given in [39].

The material chosen for the ECE-prototype is PZT-5H. Lead Zirconate Titanate, PZT, is a member of the Perovskites ceramic family, members of which are characterized by hexagonal oxygen network [67] shown in figure 19. PZT-materials show excellent piezoelectric properties, which can further be enhanced by adding dopants in the structure. Specifically, in PZT-5H the dopant is Neobium, Nb. Dopant takes its place in the center of

cube. The location of the dopant, however, changes somewhat as the material is polarized. This is shown in figure 19 as polarized tetragonal arrangements. The change in the location induces a permanent dipole moment in the crystal.

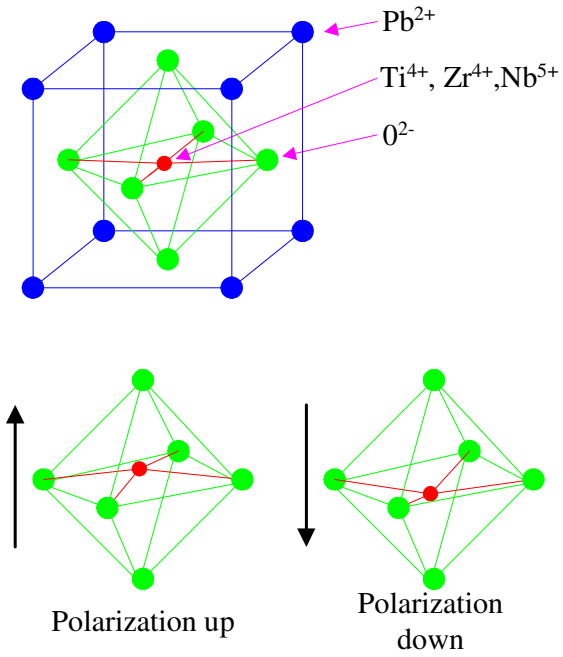

Figure 19. Unit cell for the Perovskite family.

PZT-5H shows cubic symmetry above Curie temperature with no piezoelectric properties [21], but by a careful choice of balance between the amounts of Zr and Ti, tetragonal crystal symmetry is obtained below Curie temperature. This choice allows the piezoelectric properties to be maximized [69]. The addition of Nb in the structure makes piezoelectric material soft in electrical sense, which means, amongst other things, large piezoelectric and electromechanical coupling coefficients. Soft materials can be polarized fairly easily, which behavior is in direct analogy with soft magnetic materials. All these features are preferable in a low-voltage actuator application, such as the ECE.

6.2 Theory

The constitutive equations of piezoelectric phenomenon are derived in this chapter. The derivation is based on the use of tensors. Introduction to the tensor mathematics can be found in various textbooks, such as [7].

It is recognized [55] that the piezoelectric phenomenon is dependent upon the variables presented in table 2.

Variable	Symbol	Tensor rank	Number of components
Temperature	T	0^{th} rank	1 (scalar)
Entropy	S	0^{th} rank	1 (scalar)
Electric field	E_i	1^{st} rank	3 (vector)
Electric flux density	D_i	1^{st} rank	3 (vector)
Stress	σ_{ij}	2^{nd} rank	6
Strain	e_{ij}	2^{nd} rank	6

Table 2. Variables required in the piezoelectric analysis.

In addition to the variables above, the derivation exploits medium equation for electric flux density, generalized Hooke's law, 1^{st} and 2^{nd} laws of thermodynamics, equation for thermal expansion as well as definition of Gibb's free energy and direct piezoelectric effect. The two latter are perhaps the least known and, hence, they are quoted next in equations (45) and (46), respectively.

Gibbs free energy $$G = U - \sigma_{ij} e_{ij} - E_i D_i - TS \,, \tag{45}$$

Direct piezoelectric effect $$D_i = d_{ijk} \sigma_{jk} \,, \tag{46}$$

where G is Gibb's free energy, U internal energy of the system and d_{ijk} piezoelectric 3^{rd} rank tensor.

Now, by choosing σ_{ij}, E_i and T as independent variables in the analysis, e_{ij}, D_i and S become functions of independent variables. By forming the exact differentials, it is obtained [55] for dependent variables that

$$
\begin{aligned}
&\qquad\text{I}\qquad\qquad\text{II}\qquad\qquad\text{III}\\
\mathrm{d}e_{ij} &= \left.\frac{\partial e_{ij}}{\partial \sigma_{kl}}\right|_{(E,T)} \mathrm{d}\sigma_{kl} + \left.\frac{\partial e_{ij}}{\partial E_k}\right|_{(\sigma,T)} \mathrm{d}E_k + \left.\frac{\partial e_{ij}}{\partial T}\right|_{(E,\sigma)} \mathrm{d}T\\
&\qquad\text{IV}\qquad\qquad\text{V}\qquad\qquad\text{VI}\\
\mathrm{d}D_i &= \left.\frac{\partial D_i}{\partial \sigma_{kl}}\right|_{(E,T)} \mathrm{d}\sigma_{kl} + \left.\frac{\partial D_i}{\partial E_k}\right|_{(\sigma,T)} \mathrm{d}E_k + \left.\frac{\partial D_i}{\partial T}\right|_{(E,\sigma)} \mathrm{d}T\\
&\qquad\text{VII}\qquad\qquad\text{VIII}\qquad\qquad\text{IX}\\
\mathrm{d}S &= \left.\frac{\partial S}{\partial \sigma_{kl}}\right|_{(E,T)} \mathrm{d}\sigma_{kl} + \left.\frac{\partial S}{\partial E_k}\right|_{(\sigma,T)} \mathrm{d}E_k + \left.\frac{\partial S}{\partial T}\right|_{(E,\sigma)} \mathrm{d}T
\end{aligned}
\tag{47}
$$

Equation (47) now reveals fundamental relationships about piezoelectric crystals. The following table summarizes the effects found in the crystal and their meaning.

Term	Meaning	Explanation
I	Elasticity	Terms of stiffness tensor c_{ijkl} that relates strain and stress fields.
II	Converse piezoelectric effect	Refers to the strain field generation, when applying electric field in the crystal. Converse effect is utilized in piezoelectric actuator applications.
III	Thermal expansion	Terms of thermal expansion tensor α_{ij} that relates temperature rise to the strain in crystal.
IV	Direct piezoelectric effect	Terms of piezoelectric tensor d_{ijk} in equation (46) that relates electric flux density to the stress in the crystal. Direct effect is utilized in piezoelectric sensor applications.
V	Permittivity	Terms of permittivity tensor ε_{ij} that relates electric flux density and electric field.
VI	Pyroelectric effect	Terms of pyroelectric tensor p_i that relates electric flux density generation in the crystal to changing temperature.
VII	Piezocaloric effect	Refers to the heat generation in the crystal, when changing stress field.
VIII	Electrocaloric effect	Refers to the heat generation in the crystal, when changing electric field strength.
IX	Heat capacity	C, refers to the thermal intake capacity of the crystal under constant E and σ.

Table 3. Terms of the equation set (47) explained.

Now, integrating equation (47) would directly lead to the desired set of constitutive piezoelectric equations. However, omitting further analysis would result in a plethora of unknown material constants in the resulting equations. Therefore, the analysis continues by considering the Gibbs free energy of the system. The total differential of equation (45) is given by

$$dG = -eijd\sigma_{ij} - D_i dE_i - SdT \tag{48}$$

Further, forming the first and second differentials yields

$$-\left.\frac{\partial G}{\partial \sigma_{ij}}\right|_{(T,E)} = e_{ij} \text{ and } -\left.\frac{\partial G}{\partial E_i}\right|_{(T,\sigma)} = D_i \text{ and } -\left.\frac{\partial G}{\partial T}\right|_{(E,\sigma)} = S \tag{49}$$

and

$$\begin{aligned}
-\left.\frac{\partial^2 G}{\partial \sigma_{ij}\partial E_k}\right|_{(T)} &= \left.\frac{\partial e_{ij}}{\partial E_k}\right|_{(\sigma,T)} = \left.\frac{\partial D_k}{\partial \sigma_{ij}}\right|_{(E,T)} = d_{kij}^{(T)} \\
-\left.\frac{\partial^2 G}{\partial \sigma_{ij}\partial T}\right|_{(E)} &= \left.\frac{\partial e_{ij}}{\partial T}\right|_{(\sigma,T)} = \left.\frac{\partial S}{\partial \sigma_{ij}}\right|_{(E,T)} = \alpha_{ij}^{(E)} \\
-\left.\frac{\partial^2 G}{\partial E_i\partial T}\right|_{(\sigma)} &= \left.\frac{\partial D_i}{\partial T}\right|_{(\sigma,E)} = \left.\frac{\partial S}{\partial E_i}\right|_{(\sigma,T)} = p_i^{(\sigma)}
\end{aligned} \tag{50}$$

Now, the second differentials derived actually show that [67]

1. Coefficients for direct and converse piezoelectric effects match
2. Coefficients for thermal expansion and piezocaloric effect match
3. Coefficients for pyroelectric and electrocaloric effects match

These considerations show that it is possible to reduce the number of unknowns required in the analysis by thermodynamic considerations. Moreover, the number of constants required in the analysis is further reduced by the symmetry of the piezoelectric crystals. Thirdly, the free differentiation order of the 2nd derivatives results in the symmetry of the tensors with respect to the main diagonal.

Finally, the integrated form of equation (47) may be presented by taking into account the above considerations [67].

$$\begin{aligned}
e_{ij} &= s_{ijkl}^{(E,T)}\sigma_{kl} + d_{mij}^{(\sigma,T)}E_m + \alpha_{ij}^{(\sigma,E)}\Delta T \\
D_i &= d_{ikl}^{(E,T)}\sigma_{kl} + \varepsilon_{im}^{(\sigma,T)}E_m + p_i^{(\sigma,E)}\Delta T \\
\Delta S &= \alpha_{ij}^{(E,T)}\sigma_{ij} + p_m^{(\sigma,T)}E_m + \left(C^{(\sigma,E)}/T\right)\Delta T
\end{aligned} \tag{51}$$

Equation (51) may further be simplified by omitting thermal effects as well as entropy changes.

$$\begin{aligned} e_{ij} &= s_{ijkl}^{(E)}\sigma_{kl} + d_{mij}^{(\sigma)}E_m \\ D_i &= d_{ikl}^{(E)}\sigma_{kl} + \varepsilon_{im}^{(\sigma)}E_m \end{aligned} \tag{52}$$

The final set of coupled constitutive equations for piezoelectric materials in matrix notation is given in equation (53) assuming that piezoelectric coefficients are independent of E_i or σ_{ij}.

$$\begin{cases} \underline{e} = s^{(E)}\underline{\sigma} + d\underline{E} \\ \underline{D} = d^T\underline{\sigma} + \varepsilon^{(\sigma)}\underline{E} \end{cases} \Leftrightarrow \begin{bmatrix} \underline{e} \\ \underline{D} \end{bmatrix} = \begin{bmatrix} s^{(E)} & d \\ d^T & \varepsilon^{(\sigma)} \end{bmatrix} \begin{bmatrix} \underline{\sigma} \\ \underline{E} \end{bmatrix}, \tag{53}$$

where

$\underline{e}$	Strain vector
$s^{(E)}$	Compliance matrix under constant electric field
d	Piezoelectric matrix
$\underline{\sigma}$	Stress vector
$\underline{D}$	Electric flux density
$\varepsilon^{(\sigma)}$	Permittivity matrix under constant stress
$\underline{E}$	Electric field

It can be shown that in tetragonal systems by taking into account all the symmetries and omitting temperature effects, the original 157 constants required in solving equation (47) are reduced to 11 independent material constants required in solving equation (53). This works to illustrate the significance of crystal symmetries in piezoelectric analysis.

Finally, it is noted that if another choice of independent variables were made

$$\begin{aligned} \sigma_{ij} &= c_{ijkl}^{(E)}e_{kl} - d_{mpq}c_{pqij}^{(E)}E_m \\ D_i &= d_{ikl}c_{klpq}^{(E)}e_{pq} + \varepsilon_{im}^{(e)}E_m \end{aligned}, \tag{54}$$

which form will be needed in the piezoelectric FE-formulation. In the matrix form this can be expressed by

$$\begin{bmatrix} \underline{\sigma} \\ \underline{D} \end{bmatrix} = \begin{bmatrix} c^{(E)} & -c^{(E)}d \\ \left(c^{(E)}d\right)^T & \varepsilon^{(\sigma)} \end{bmatrix} \begin{bmatrix} \underline{e} \\ \underline{E} \end{bmatrix} \tag{55}$$

6.3 Piezoelectric Finite Element Method

6.3.1 Weak form

A piezoelectric body needs to fulfill not only the Cauchy equation of motion introduced in equation (7), but also the Gauss's law for electric flux [10], i.e.

$$divD_i = q\,, \tag{56}$$

where q is the volume charge density. As with the purely structural FEM the underlying assumptions were the conservation of mass and linear momentum, here in addition to those, the conservation of charge is assumed. This can be expressed in integral form by

$$\int_{\partial V} \underline{J} \bullet \underline{n}\, dA + \frac{\partial}{\partial t}\int_V q\, dV = 0\,, \tag{57}$$

where $\underline{J}$ is the current density.

In order to apply the principle of virtual work, the concept of the virtual potential, δv, is utilized. It has the same properties as the virtual displacement introduced earlier. Accordingly, the energy balance by the principle of virtual work is given by

$$\int_V \delta v\left(divD_i - q\right) dV = 0 \qquad \forall \delta v\,, \tag{58}$$

where v is the electric potential. According to equation (17),

$$div(D_i \delta v) = \delta v\, div(D_i) + \delta\left(\nabla v\right) \bullet D_i\,, \tag{59}$$

from which it follows

$$0 = \int_V \delta v\left(divD_i - q\right) dV = \int_V div(D_i \delta v)\, dV - \int_V \left(\delta E_i\right) D_i\, dV - \int_V q\delta v\, dV \tag{60}$$

by noting that $\underline{E} = -\nabla v$. Applying the Gauss's divergence law yields

$$0 = \int_{\partial V} D_i \delta v \bullet \underline{n}\, dA - \int_V \left(\delta E_i\right) Di\, dV - \int_V q\delta v\, dV \tag{61}$$

Hence, any piezoelectric body must fulfill the set of weak form equations (62) as well as the constitutive equations given in equation (54).

$$\begin{cases} \int_V \rho \delta \underline{u} \bullet \ddot{\underline{u}}\, dV + \int_V \delta e_{ij} \sigma_{ij}\, dV = \int_V \rho \delta \underline{u} \bullet \underline{b}\, dV + \int_{A_{NEUMANN}} \delta \underline{u} \bullet \underline{a}\, dA \\ \int_V (\delta E_i) D_i\, dV + \int_V q \delta v\, dV = \int_{\partial V} D_i \delta v \bullet \underline{n}\, dA \end{cases} \quad \forall \delta \underline{u}, \forall \delta v \qquad (62)$$

6.3.2 Discretization

These equations now form the basis for the piezoelectric FE-formulation. In order to discretisize the weak form, it is acknowledged that the solution variables, nodal displacements and nodal electric potentials, may be approximated within a single element by

$$\underline{u}(\underline{x},t) \approx N^u(\underline{x})\underline{u^e}(t) = \sum_i^n N_i^u(\underline{x})\underline{u_i^e}(t) \qquad \text{(23) rewritten}$$

$$v(\underline{x},t) \approx \left[\underline{N^v}(\underline{x})\right]^T \underline{v^e}(t) = \sum_i^n N_i^v(\underline{x}) v_i^e(t), \qquad (63)$$

where $v(\underline{x},t)$ is the electric potential at a point within the element, $\underline{N^v}(\underline{x}) = \left[N_1^v(\underline{x}) \quad N_2^v(\underline{x}) \quad \cdots \quad N_n^v(\underline{x})\right]^T$ the element electric potential support with $N_i^v(\underline{x})$ being the electric potential shape function associated with the ith node, n the number of nodes, $\underline{v^e}(t)$ the listing of the nodal electric potentials in the element and $v_i^e(t)$ electric potential at the ith node. Shape functions N_i^v define the basis for the function space, in which electric potential is approximated. Moreover, as was done with purely structural FEM, also here spatial and time dependencies are separated to shape functions and nodal displacements as well as potentials, respectively.

Moreover, for equation (63) to hold, $N_i^v(\underline{x})$ are required to fulfill

$$N_i^v(\underline{x_j}) = \delta_{ij}, \qquad (64)$$

where $\underline{x_j}$ is the location of the jth node. This formulation is, again, called the Galerkin's method [43].

Now, strain $\underline{e}$ and electric field $\underline{E}$ are estimated from the nodal displacements and nodal electric potentials by equations (27), (28) and (65) by

$$\underline{e} \approx S^u N^u \underline{u^e} = B^u \underline{u^e} \qquad \text{(27)\&(28) rewritten}$$

$$\underline{E} \approx S^v \left(\underline{N^v}\right)^T \underline{v^e} = -B^v \underline{v^e} \qquad (65)$$

$$\text{with } B^v = S^v \left(\underline{N^v}\right)^T = \begin{bmatrix} \partial_x & \partial_y & \partial_z \end{bmatrix}^T \left(\underline{N^v}\right)^T, \qquad (66)$$

with S^v and B^v being continuous and discrete gradient operators, respectively. These definitions allow for solving the terms in the integral equation (62). Note that the time and spatial coordinate arguments for various variables are left out of the equations below for the sake of clarity.

$$\int_\Omega \rho \delta \underline{u} \bullet \ddot{\underline{u}}\, dV = \left(\delta \underline{u^e}\right)^T M^e \ddot{\underline{u^e}} \qquad \text{(35) rewritten}$$

$$\begin{aligned}
&\int_\Omega \delta e_{ij} \sigma_{ij}\, dV = \int_\Omega \delta e_{ij} \left(c_{ijkl}^{(E,T)} e_{kl} - d_{mpq} c_{pqij} E_m\right) dV \hat{=} \int_\Omega \delta \left(B^u \underline{u}^e\right)^T \left(c^{(E)} \underline{e} - dc^{(E)} \underline{E}\right) dV \\
&= \int_\Omega \delta \left(B^u \underline{u}^e\right)^T \left(c^{(E)} B^u \underline{u}^e + dc^{(E)} B^v \underline{v}^e\right) dV \\
&= \left(\delta \underline{u}^e\right)^T \left[\int_\Omega \left(B^u\right)^T c^{(E)} B^u dV\right] \underline{u}^e + \left(\delta \underline{u}^e\right)^T \left[\int_\Omega \left(B^u\right)^T dc^{(E)} B^v dV\right] \underline{v}^e \\
&= \left(\delta \underline{u}^e\right)^T K^e \underline{u}^e + \left(\delta \underline{u}^e\right)^T K_Z^e \underline{v}^e
\end{aligned} \qquad (67)$$

$$\int_\Omega \rho \delta \underline{u} \bullet \underline{b}\, dV = \left(\delta \underline{u^e}\right)^T \underline{F_V^e} \qquad \text{(38) rewritten}$$

$$\int_{\partial\Omega_{NEUMANN}} \delta \underline{u} \bullet \underline{a}\, dA = \left(\delta \underline{u^e}\right)^T \underline{F_P^e} \qquad \text{(39) rewritten}$$

$$\begin{aligned}
&\int_V (\delta E_i) D_i\, dV = \int_V (\delta E_i) \left(d_{ikl} c_{klpq} e_{pq} + \varepsilon_{im}^{(e)} E_m\right) dV \\
&\hat{=} -\int_V \left(B^v \delta \underline{v^e}\right)^T \left(\left(c^{(e)} d\right)^T B^u \underline{u^e} - \varepsilon^{(e)} B^v \underline{v^e}\right) dV \\
&= -\left(\delta \underline{v^e}\right)^T \left[\int_V \left(B^v\right)^T \left(c^{(e)} d\right)^T B^u\, dV\right] \underline{u^e} + \left(\delta \underline{v^e}\right)^T \left[\int_V \left(B^v\right)^T \varepsilon^{(e)} B^v\, dV\right] \underline{v^e} \\
&= -\left(\delta \underline{v^e}\right)^T \left(K_Z^e\right)^T \underline{u^e} + \left(\delta \underline{v^e}\right)^T K_D^e \underline{v^e}
\end{aligned} \qquad (68)$$

$$\int_\Omega q \delta v\, dV = \int_\Omega q \left(\underline{N^v}\right)^T \delta \underline{v^e}\, dV = \left(\delta \underline{v^e}\right)^T \int_\Omega \underline{N^v} q\, dV = \left(\delta \underline{v^e}\right)^T \underline{Q_V^e} \qquad (69)$$

$$\int_{\partial\Omega} D_i \delta v \bullet \underline{n}\, dA \hat{=} \int_{\partial\Omega} \left(\underline{N^v}\right)^T \left(\delta \underline{v^e}\right) \underline{D} \bullet \underline{n}\, dA = \left(\delta \underline{v^e}\right)^T \int_{\partial\Omega} \underline{N^v} \left(\underline{D} \bullet \underline{n}\right) dA = -\left(\delta \underline{v^e}\right)^T \underline{Q_S^e} \qquad (70)$$

Now, equation (62) becomes

$$\begin{cases} \left(\delta \underline{u}^e\right)^T M^e \ddot{\underline{u}}^e + \left(\delta \underline{u}^e\right)^T \left[K^e \underline{u}^e + K_Z^e \underline{v}^e\right] = \left(\delta \underline{u}^e\right)^T \left[\underline{F_V^e} + \underline{F_P^e}\right] \\ -\left(\delta \underline{v}^e\right)^T \left[\left(K_Z^e\right)^T \underline{u}^e - K_D^e \underline{v}^e\right] + \left(\delta \underline{v}^e\right)^T \underline{Q_V^e} = -\left(\delta \underline{v}^e\right)^T \underline{Q_S^e} \end{cases} \quad \forall \delta \underline{u}^e, \forall \delta \underline{v}^e \tag{71}$$

Since virtual displacement and potential are arbitrary, the discretized weak form must fulfill (with an addition of damping)

$$\begin{cases} M^e \ddot{\underline{u}}^e + C^e \dot{\underline{u}}^e + K^e \underline{u}^e + K_Z^e \underline{v}^e = \underline{F_V^e} + \underline{F_P^e} \\ \left(K_Z^e\right)^T \underline{u}^e - K_D^e \underline{v}^e = \underline{Q_V^e} + \underline{Q_S^e} \end{cases}, \tag{72}$$

which can be expressed in the matrix form by

$$\begin{bmatrix} M^e & 0 \\ 0 & 0 \end{bmatrix} \begin{bmatrix} \ddot{\underline{u}}^e \\ \ddot{\underline{v}}^e \end{bmatrix} + \begin{bmatrix} C^e & 0 \\ 0 & 0 \end{bmatrix} \begin{bmatrix} \dot{\underline{u}}^e \\ \dot{\underline{v}}^e \end{bmatrix} + \begin{bmatrix} K^e & K_Z^e \\ \left(K_Z^e\right)^T & -K_D^e \end{bmatrix} \begin{bmatrix} \underline{u}^e \\ \underline{v}^e \end{bmatrix} = \begin{bmatrix} \underline{F_V^e} + \underline{F_P^e} \\ \underline{Q_V^e} + \underline{Q_S^e} \end{bmatrix}, \tag{73}$$

where

M^e	From equation (35).	
C^e	From equation (36).	
$K^e = \int_\Omega \left(S^u N^u\right)^T c^{(E)} \left(S^u N^u\right) dV$	Element stiffness matrix. The same as (37), except that c under constant electric field.	(74)
$K_Z^e = -\int_\Omega \left(S^u N^u\right)^T c^{(E)} dS^V \left(\underline{N^V}\right)^T dV$	Piezoelectric coupling matrix.	(75)
$K_D^e = \int_\Omega \left(S^V \left(\underline{N^V}\right)^T\right)^T \varepsilon^{(e)} S^V \left(\underline{N^V}\right)^T dV$	Dielectric conductivity matrix.	(76)
$\underline{F_V^e} + \underline{F_P^e}$	Equations (38) and (39).	
$\underline{Q_V^e} = \int_\Omega \underline{N^v} q(t)\, dV$	Volume charges (predefined)	(77)
$\underline{Q_S^e} = \int_{\partial\Omega} \underline{N^v} \left(\underline{D}(t) \bullet \underline{n}\right) dA$	Surface charges (predefined)	(78)

These definitions complete the discretization of the constitutive piezo equations. Finally, the same principles stated about damping, total system matrices and harmonic analysis in the end of chapter 4.5 apply in the piezoelectric analysis as well.

6.4 Piezoelectricity in ANSYS

6.4.1 Analysis types

ANSYS software package [5] has the capability to perform static, transient, modal and harmonic analyses for piezoelectric structures.

Piezoelectric analysis is challenging from the numerical point of view, since such an analysis must couple structural and electric effects. There are two methods to achieve this coupling. The first method is sequential coupling. In sequential coupling one field is solved first and based on this information, the other field is solved. Ultimately, iteration leads to convergence. The other and more elegant method uses a direct method and coupled-field elements. In practice, the direct method handles coupling by formulating such element matrices and load vectors that all the necessary terms are directly taken into account. Piezoelectric analysis in ANSYS utilizes matrix coupling, which means that linear problems can be solved in one step.

In piezoelectric analysis, the user is required to input stiffness constants, permittivity constants, piezoelectric constants and density for the material. The data required is readily available in the piezo manufacturer supplied datasheets. In general, ANSYS allows for defining completely anisotropic piezo material. However, PZT-5H material used in this work shows tetragonal symmetry, which reduces the number of required parameters to 12. Moreover, the analysis requires correct selection of the element type and boundary conditions. These three factors are now considered in turn.

6.4.2 Material definition and element types

The required constant matrices for tetragonal z-polarized piezo system ready for input in ANSYS are defined in matrices (79), (80) and (81). The notation for constants follows ANSI/IEEE standard 176-1987.

$$\text{Relative permittivity } \varepsilon_r^{(e)} = \begin{bmatrix} \varepsilon_{11relative}^{(e)} & 0 & 0 \\ 0 & \varepsilon_{11relative}^{(e)} & 0 \\ 0 & 0 & \varepsilon_{33relative}^{(e)} \end{bmatrix} \tag{79}$$

$$\text{Piezoelectric strain matrix } d = \begin{bmatrix} 0 & 0 & d_{31} \\ 0 & 0 & d_{31} \\ 0 & 0 & d_{33} \\ 0 & 0 & 0 \\ 0 & d_{15} & 0 \\ d_{15} & 0 & 0 \end{bmatrix} \tag{80}$$

$$\text{Compliance matrix } s^{(E)} = \begin{bmatrix} s_{11}^{(E)} & s_{12}^{(E)} & s_{13}^{(E)} & 0 & 0 & 0 \\ s_{12}^{(E)} & s_{11}^{(E)} & s_{13}^{(E)} & 0 & 0 & 0 \\ s_{13}^{(E)} & s_{13}^{(E)} & s_{33}^{(E)} & 0 & 0 & 0 \\ 0 & 0 & 0 & s_{66}^{(E)} & 0 & 0 \\ 0 & 0 & 0 & 0 & s_{44}^{(E)} & 0 \\ 0 & 0 & 0 & 0 & 0 & s_{44}^{(E)} \end{bmatrix} = \left[c^{(E)}\right]^{-1} \tag{81}$$

For the 3D piezo modeling, there are two types of elements available in ANSYS Mechanical license, solid5 and solid98. Solid5 is an 8-node hexahedron with optional quadratic shape functions, whereas solid98 is a 10-node tetrahedron with quadratic shape functions. The use of quadratic shape functions generally improves the accuracy of the solution by allowing more accurate deformation shapes for elements.

Solid5 and solid98 elements support magnetic, thermal, electric, piezoelectric and structural field formulations. They do not, however, support dielectric tangent losses, which would allow for modeling the heating of the element. However, they do support large deflection analysis and stress stiffening in piezoelectric analysis, which are essential features, when non-linear structures, such as prestressed piezo elements, are modeled.

6.4.3 Boundary conditions and solvers

In the 3-D piezoelectric analysis, elements have four degrees of freedom: three displacement DOFs and voltage. Therefore, these are also available in setting the boundary conditions for the analysis. Generally, in an actuator analysis displacement DOFs model the clamping of the structure and voltage is used as an excitation signal. In

sensor analysis, on the other hand, displacement works as an excitation and the voltage output is the required output. In addition to displacement and voltage loads, pressure and force loads are available as well.

The final step before solving the model is the selection of the solver type. ANSYS recommends that either sparse matrix or Jacobi Conjugate Gradient (JCG) solver is used in the piezoelectric analysis. The choice of the solver affects the speed of the solution. In this work, the JCG solver was successfully utilized.

7. EAR CANAL EXCITER

7.1 Prototype specifications

The purpose of the prototype is to verify the FE-model predictions and demonstrate technology. Although the ear model clearly shows that the proposed actuator function will not be feasible, the prototype is still needed for the verification purposes. Moreover, the sensor function was not modeled. Therefore, the prototype will also be used as a demonstrator for the tissue microphone function.

The prototype needs to able to reproduce frequencies from 300 Hz to 10 kHz. Since the ECE is designed to work with mobile devices, it must comply with the audio bandwidth standards. The GSM narrowband and wideband range from 300 to 3400 Hz and from 150 to 7000 Hz, respectively. Therefore, the prototype almost covers the whole narrowband, but also the wideband, except for the lowest frequencies. However, the bandwidth of ECE will not be artificially reduced, if the ECE should be able to reproduce a larger bandwidth. Obtaining a flat response over a wide frequency range should not be problematic, since the piezo structures are very stiff and at the same time fairly light. Hence, the first resonance for a small structure should lie well above the audible frequency range.

In addition to the bandwidth requirements, there will also be size constraints. The ECE must fit in the tympanic canal and, hence, its outer diameter must be limited to 6 mm. The maximum length is 5 mm, since the canal makes the sharp S-turn near the outer end of the canal.

Since the size and shape requirements imply a cylindrical shape, the ECE will be optimized to produce maximal radial and minimal axial vibration. The impedance matching to the tissue will be made with a layer of silicon rubber, of which characteristics are known to comply well with water rich tissue.

This chapter describes the geometry of the ECE and certain design features that ensure fulfilling the requirements. The design points are confirmed with FE-simulations and the final prototype characteristics will be compared to the FE-simulation results. The chapter closes with a discussion on the modeling errors and an attempt to improve the modeling accuracy by including hysteresis in the analysis.

The prototypes were designed and manufactured by the University of Oulu Microelectronics laboratory based on the specifications listed above. The author wishes to stress that especially two design points, the method for the axial displacement reduction and the steel-stiffened piezo structure, are not author's own innovations, but originate from the University of Oulu.

7.2 Geometry

The geometry of the ear canal exciter is given in figure 20. A copper pipe (magenta) running through the structure and the end plates made of alumina ceramics (blue), Al_20_3, form the device body. The choice of alumina is based on its high stiffness and easy machineability. The ceramic plates are glued to the copper piper with Fineplacer 145 – glue (green).

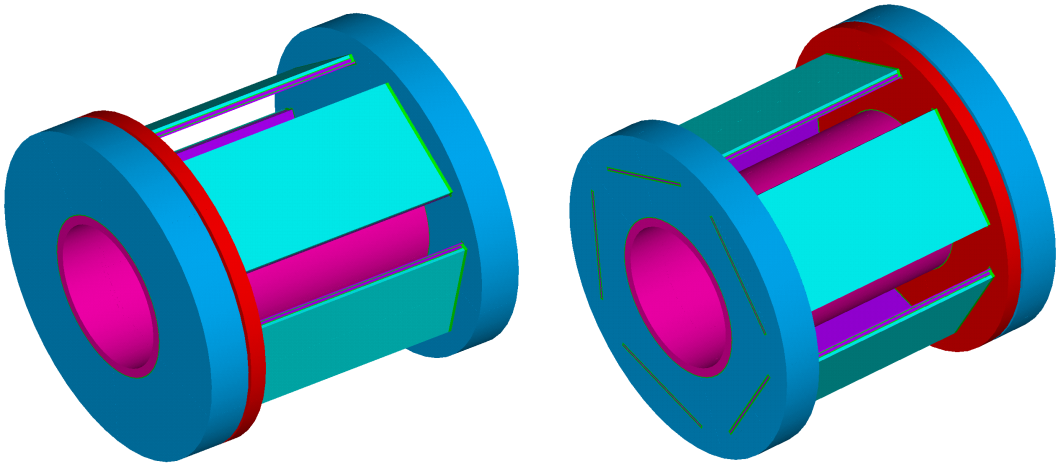

Figure 20. The CAD-drawing of the ECE geometry. The silicon rubber layer is not shown. Magenta – copper, blue - alumina ceramics, red – polycarbonate, turquoise – piezo, violet – steel, green – glue.

The piezo structure consists of steel and piezo material PZT-5H. The structure is best shown in figure 21. Steel (violet) is glued to the frame structure. On top of the connecting steel plate, there is another steel layer. The actual piezo element (turquoise) is then glued on top of the second steel layer. The steel plates stiffen the structure and provide more displacement. The increased displacement levels with a second steel layer were confirmed by FE-simulations. In total, there are five piezo plates in the ECE, which are electrically connected in parallel. In practice, this means that all the piezo plates are excited in the same phase and that the total capacitance of the system will be fairly large.

Initially, the piezo plates were directly glued to the alumina plates and there was no polycarbonate back plate in the structure as shown in figure 20 in red. However, it was noticed that such a solution led to very high axial displacement and reduced radial vibration levels. Therefore, the piezo structure was uncoupled from the ECE body with a polycarbonate plate as shown in figure 21. The innovation includes that the axial vibration affects only the polycarbonate and, hence, the alumina plates do not exhibit significant axial vibration.

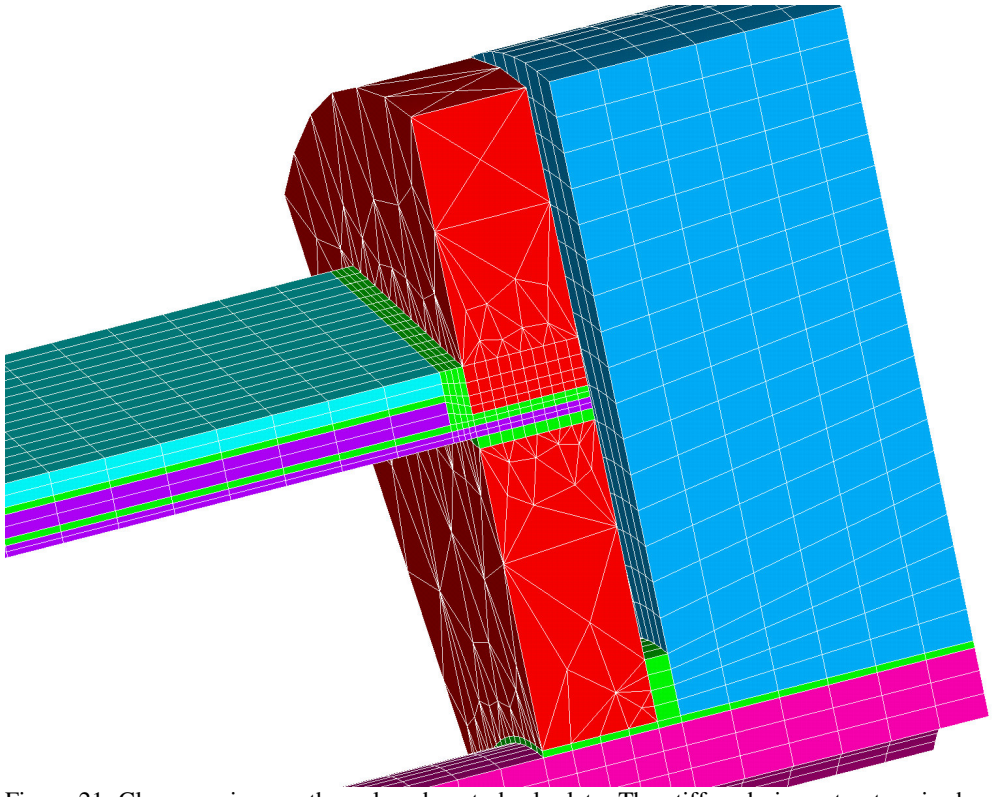

Figure 21. Close-up view on the polycarbonate back plate. The stiffened piezo structure is shown as well. The color coding is identical to that in figure 20.

Figure 22 shows the improvement achieved with an addition of the polycarbonate plate according to the FE-model. The axial vibration of the alumina plates decreases by 20 dB and the radial displacement of the piezo increases by 3 dB throughout the band.

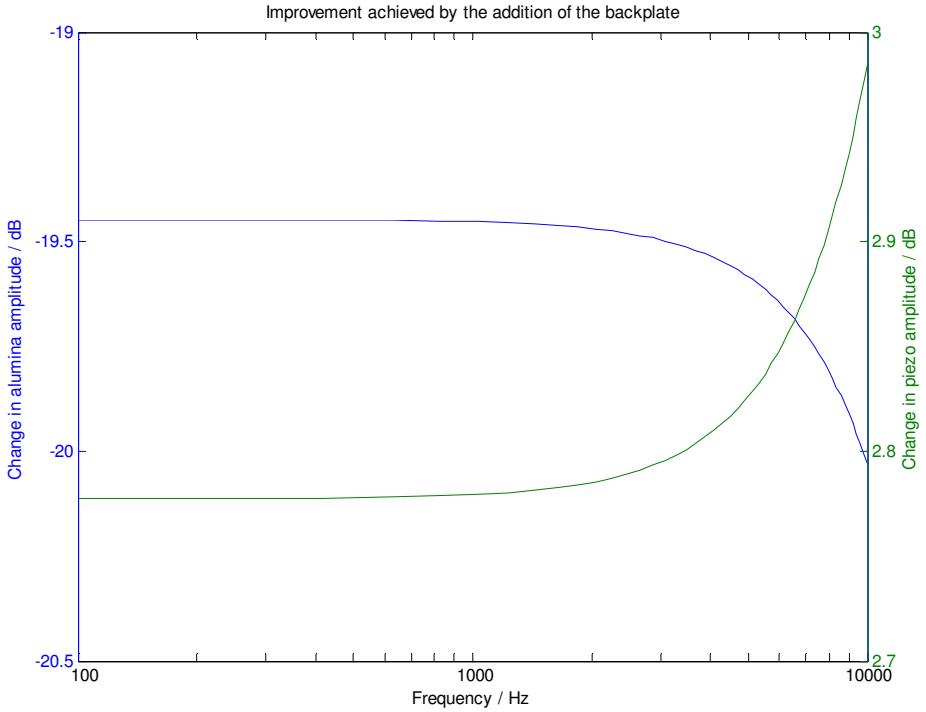

Figure 22. Improvement on the vibration characteristics achieved by the introduction of the polycarbonate back plate. The results are based on the FE-simulation.

7.3 Prototype

Figure 23 shows a sample of the prototype manufactured. The sample on the right hand side shows the device without the silicon layer. The frame of the device, the copper pipe and the alumina back plates, are clearly visible. Moreover, the piezo elements and the steel band providing electric connection can be seen. The piezo elements with steel supports attach to the polycarbonate plate at the front. The silicon layer is made of rubber rings, which can be replaced in order to ensure proper contact with the tympanic canal tissue.

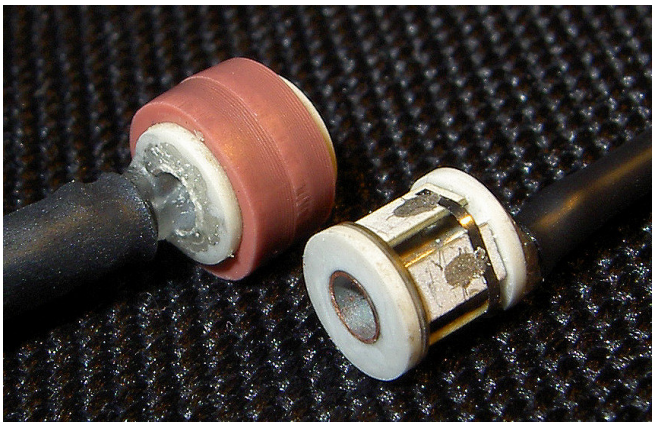

Figure 23. Ear Canal Exciter prototype. Left: ECE with silicon rubber rings. Right: ECE without rings. Piezo elements, alumina frame and the electric connections are clearly visible.

7.4 FEM model

7.4.1 Material properties

Table 4 lists the characteristics for the materials used in the ECE model. No sources are given for the data, since the materials are common engineering materials and, hence, the data is readily available in various data sheets.

Material	**Density ρ, kg·m^{-3}**	**Young modulus, GPa**	**Poisson's ratio**
Steel	7800	210	0.3
Polycarbonate	1300	15.18	0.36
Alumina, Al_2O_3	3750	300	0.21
Copper	8920	130	0.34
Glue, FinePlacer 145	1200	6	0.3
PZT-5H	7500	Equation (82)	0.3

Table 4. Material properties used in the ECE model. See equations (82)-(84) for the anisotropic piezo material properties.

Next, the piezo material characteristics are given for the z-polarized PZT-5H.

$$\text{Compliance} \quad s^{(E)} = \begin{bmatrix} 16.5 & -4.78 & -8.45 & 0 & 0 & 0 \\ -4.78 & 16.5 & -8.45 & 0 & 0 & 0 \\ -8.45 & -8.45 & 20.7 & 0 & 0 & 0 \\ 0 & 0 & 0 & 42.6 & 0 & 0 \\ 0 & 0 & 0 & 0 & 43.5 & 0 \\ 0 & 0 & 0 & 0 & 0 & 43.5 \end{bmatrix} \cdot 10^{-12} \ \text{m}^2\text{N}^{-1} \tag{82}$$

$$\text{Permittivity} \quad \varepsilon_r^{(e)} = \begin{bmatrix} 1700 & 0 & 0 \\ 0 & 1700 & 0 \\ 0 & 0 & 1470 \end{bmatrix} \tag{83}$$

$$\text{Piezoelectric matrix} \quad d = \begin{bmatrix} 0 & 0 & -274 \\ 0 & 0 & -274 \\ 0 & 0 & 593 \\ 0 & 0 & 0 \\ 0 & 741 & 0 \\ 741 & 0 & 0 \end{bmatrix} \cdot 10^{-12} \ \text{Vm}^{-1} \tag{84}$$

7.4.2 Model geometry

The FE-model compiled is an accurate replica of the final prototype and is shown in figure 24. The polycarbonate plate has been added in order to decouple the frame from the piezo structure. The piezo structure consists of two steel layers and of the piezo. Glue layers are also taken into account. Glue layers are approximated to be 15 μm thick.

The model does not take into account the silicon layer on the piezo elements. This is due to two reasons. First, the displacement levels were measured only from the surface of the piezo element, since measuring the actual silicon displacement was noticed to be virtually impossible. Secondly, the silicon rings exert force on the piezo elements and, hence, induce pretension in the piezo structure. The pretension, in turn, affects dielectric and piezoelectric properties of the piezo material [18]. Therefore, the silicon layer is omitted in order to keep the analysis of the system simple enough.

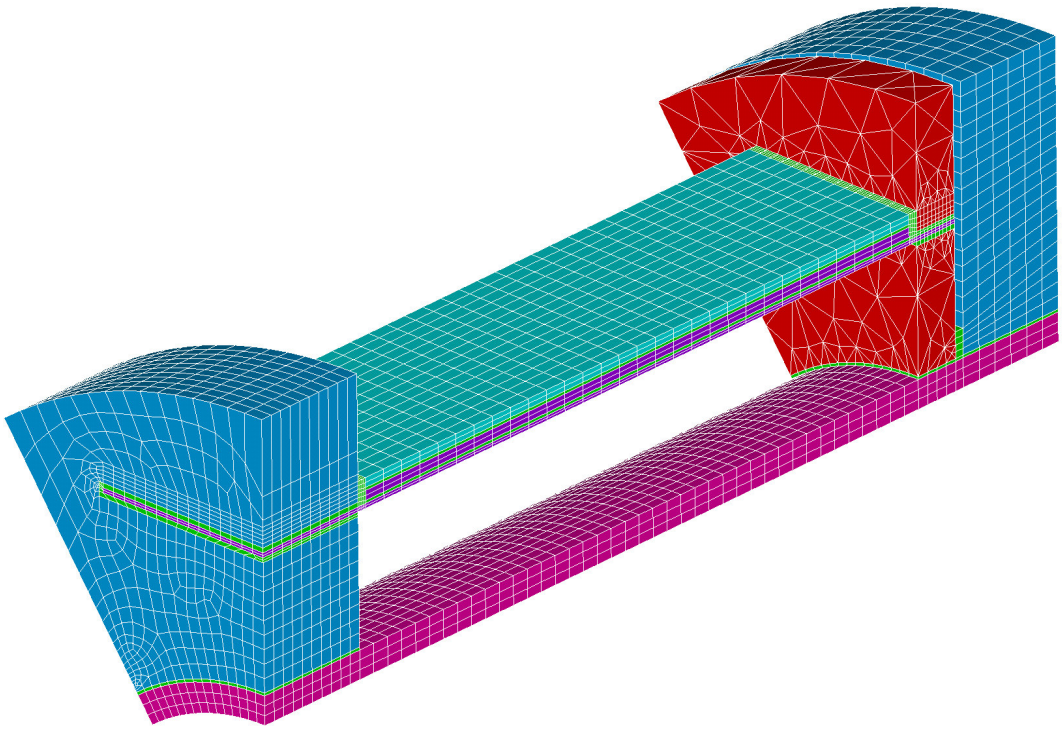

Figure 24. The ECE model mesh. $1/8^{th}$ of the total structure was modeled. Symmetry boundary conditions were applied on the cutting planes.

The piezo element is excited with a harmonic potential difference across the piezo. The symmetry boundary conditions are applied on the cutting planes. These BCs prevent the rigid body motion in circumferential direction. The clamping of the frame in radial and axial directions is realized by fixing the nodes at one of the copper pipe.

7.5 Model evaluation

Figure 25 shows the model predicted displacement characteristics of the ECE. The model was driven with a 1-V_p 1-kHz signal. The polycarbonate plate vibrates quite heavily, but the alumina plates remain practically fixed. The maximum displacement is 23.8 nm (peak) in radial direction in the center of the piezo. The alumina displacement is about 0.4 nm (peak) in axial direction.

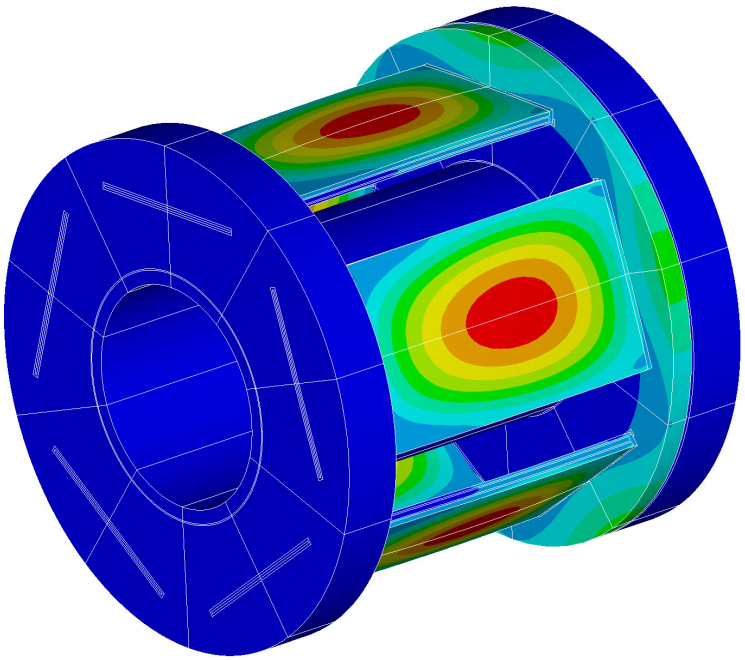

Figure 25. Displacement contours. Notice that the maximum displacement occurs at the center of the piezo.

Figures 26 and 27 show the measured and modeled radial piezo and axial alumina displacement responses, respectively. Measurements were made in the University of Oulu Microelectronics laboratory by attaching silicon mirrors at appropriate locations and using a Michelson interferometer.

As can be seen, the results are two-fold. The axial displacement is predicted accurately and the weak decreasing trend in the axial displacement is also captured by the FE-model. In practice, it was noticed that the axial-displacement was highly dependent on the amount of glue between the alumina and polycarbonate (see figure 21) plates. The axial displacement was calibrated to the measured level at low frequency by changing the amount of glue between the plates.

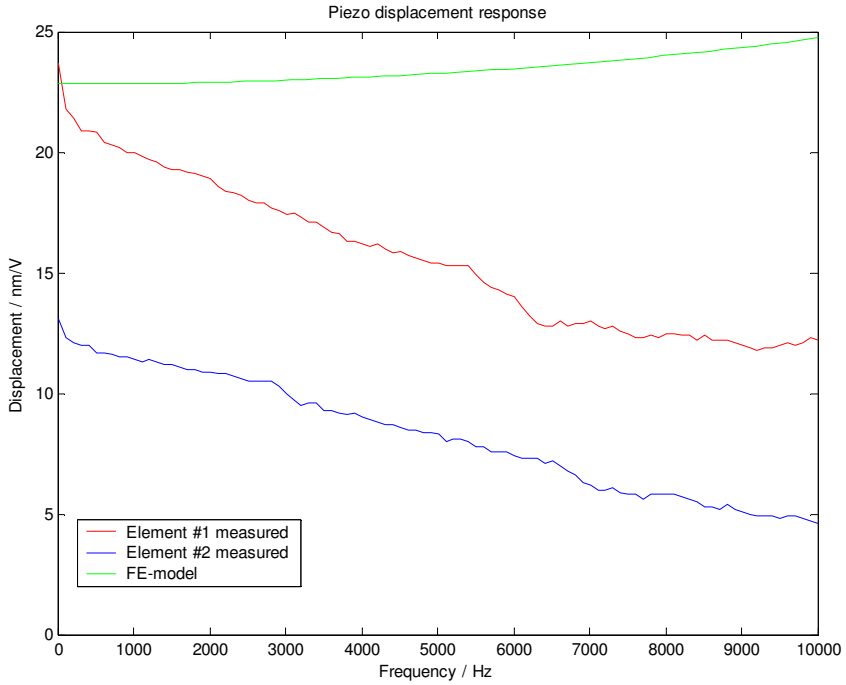

Figure 26. Radial displacement responses of the two piezo elements and the predicted displacement. Note the difference in general trends as well as the large difference between the two elements.

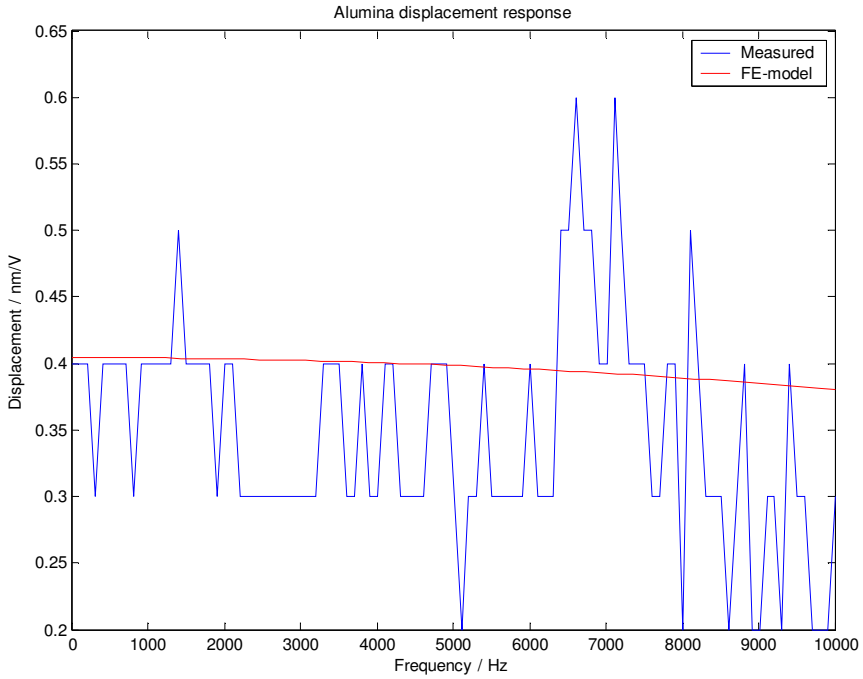

Figure 27. Alumina displacement response. The alumina displacement is fairly well predicted by the FE-model.

However, the FE-model completely misses the radial vibration characteristics of the ECE. Now, the analysis shown in figure 26 has been run without dielectric losses. Since

PZT-5H is soft piezoelectric material and, hence, is known to have high dielectric losses, an attempt was made to reduce the modeling error by introducing losses. The loss tangent for PZT-5H is 0.02 [52]. However, according to the measurements shown in figure 29, the real losses are approximately 10-fold at low frequencies. Moreover, the reference [52] states that the dielectric loss tangent grows rapidly as a function of electric field. The data presented in figure 26 has been measured with a 71-kV_{rms}/m electric field. Now, for hard piezo material PZT-4, the loss tangent grows approximately 3-fold, when going from a very low field to 100 kV_{rms}/m [52]. These considerations imply a loss tangent of about 1. However, the addition of losses (loss tangent was varied from 0.02 to 10) had only a minute effect (few nm/V maximum) on the predicted displacement and, hence, does not explain the observed discrepancy.

Continuing with the error analysis, one might argue that the shape of the response in figure 26 resembles that of a mass-controlled system. If the ECE were not properly clamped to a large mass in the measurements, then one should expect to see a low-frequency resonance and a mass-controlled decrease in vibration amplitude in ω^{-2}-fashion [53]. However, figure 28 shows the normalized piezo responses and a ω^{-2} reference curve. The conclusion is that the response behavior is not mass-controlled and, hence, no error has been made in the clamping. Also, the measurement method is one of the state-of-the-art and is very robust to external noise [40].

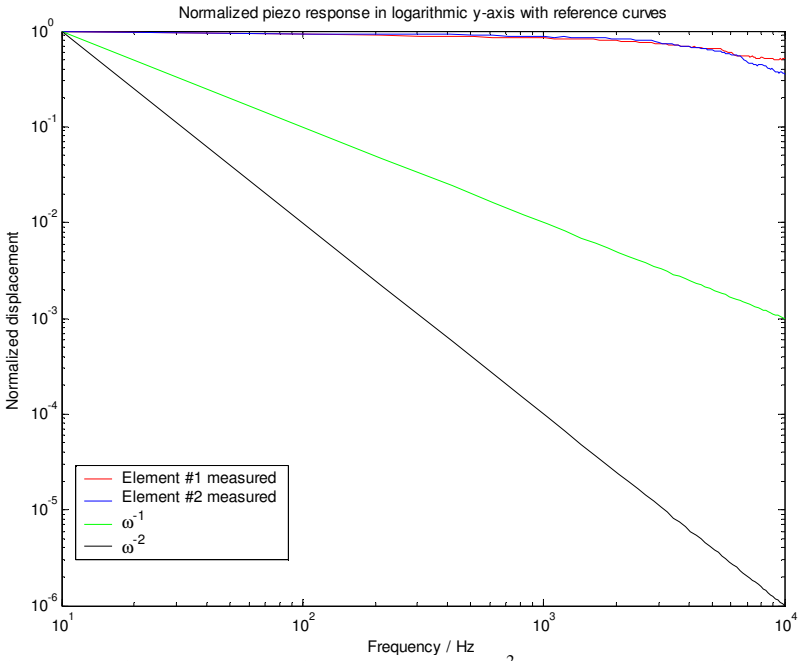

Figure 28. Piezo responses with respect to an ω^{-2}-curve. The conclusion drawn is that the measurement results are not mass-controlled.

The observed discrepancies between measured and modeled data highlight the problems in the area of piezo modeling. The piezoelectric, compliance and permittivity matrices are all functions of state variables temperature, electric field and stress field. Moreover, piezoelectric and permittivity matrices are functions of frequency [52]. Still, in the FE-model all the material parameters are assumed constant irrespective of frequency or the state of the system. The permittivity, compliance and piezoelectric constants are now discussed in turn to examine their dependencies and to identify the potential source(s) of errors.

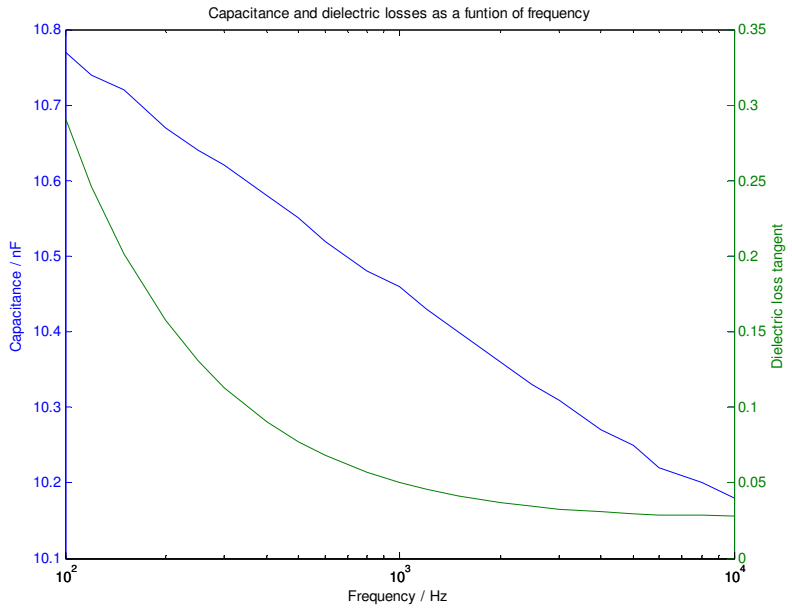

Figure 29. ECE capacitance and dielectric losses as a function of frequency. The data has been measured at 20 kV_{rms}/m.

Permittivity. Permittivity is a function of frequency, electric field strength, stress and temperature. The relative strengths of their effect are now considered in turn.

Figure 29 shows the capacitance of the ECE as a function of frequency. Capacitance is a function of geometry and permittivity. Since the geometry is virtually unchanged in the measurement, direct conclusions on the permittivity changes can be drawn based on the capacitance data. According to measurements, capacitance decreases by about 5 % over the band. The permittivity may therefore be approximated to decrease by the same amount.

The reference [52] states that the $\varepsilon_{33}^{(\sigma)}$-coefficient for the hard PZT-4 piezo increases by 5%, when the electric field increases to 100 kV/m. For somewhat harder material, PZT-8,

the same rise is below 1%. Although it is difficult to estimate, what the increase is for softer materials, 5% may be considered as the minimum increase, since the displacement measurements were made at 71 kV_{rms}/m. Since PZT-5H is considerably softer material, the increase may be tens of percents.

Next, the piezo manufacturer data sheet [52] states that the $\varepsilon_{33}^{(\sigma)}$ decreases by 4 %, when the stress increases to 35 MPa. According to the FE-simulations, the stress in the piezo at 71 kV_{rms}/m never exceeds 2 MPa. Hence, the changes in the permittivity due to the stress field can be considered negligible.

Changes in the permittivity due to the increase in temperature are significant. The data sheet [52] quotes that $\varepsilon_{33}^{(\sigma)}$ increases by 33% in the range from 0 to 40˚C. In the measurements, the piezo temperature necessarily rises due to the losses. However, because of the low electric field and the presence of the steel support acting as a heat reservoir, the heating should not, however, be excessive. Since the data sheet values are given at room temperature, a valid estimate is a 50% increase in the permittivity due to the temperature rise.

Finally, a FE-simulation was run in order to quantify the effect of permittivity on the displacement levels. For this purpose, the elements in the permittivity matrix were doubled. This resulted in a 0.5% increase in the piezo displacement at 1 kHz. Hence, it can be concluded, the changes in permittivity do not solve the discrepancy between the measured and modeled data.

Compliance. The data sheet [52] for PZT-5H states that the increase in the $s_{11}^{(E)}$-coefficient is approximately 0.1%, when the stress increases to 7 MPa. Earlier it was stated that at the electric field used in the measurements, the stress remains below 2 MPa. Hence, the compliance changes are insignificant. The data sheet does not provide data on the electric field, temperature or frequency behavior of compliance.

Moreover, the piezo stiffness contributes only a little to the total stiffness of the system. In the piezo structure, there are also steel layers as well as glue layers. Hence, only very significant changes in the piezo stiffness could result in modified vibration characteristics. In conclusion, there is no need to make any modifications to the compliance matrix.

The effect of stress stiffening on the displacement behavior was examined by first introducing pretension in the structure with static voltage that corresponded to the rms voltage of the harmonic excitation. The stress field found in the static analysis was then used as a pretension field in the harmonic analysis. However, no changes in the displacement pattern were observed by taking the pretension effects into account. It may be that the stress field at 71 kV_{rms}/m is such weak that it does not have significant stiffening effect.

Piezoelectric matrix. According to the reference [40], the elements of the piezoelectric matrix have the most significant impact on the displacement characteristics. This is plausible, since the piezoelectric coefficients couple the strain field and electric field linearly. Hence, changes in these coefficients affect the strain directly.

The elements of the piezoelectric matrix are functions of frequency, electric field strength, stress and temperature. However, no data on the behavior of the piezoelectric coefficients under changing electric field was found. Therefore, it is assumed that the electric field dependency is negligible.

The source [40] states that the changes in the piezoelectric coefficients are of the same order than those in permittivity. Based on figure 29 it was deduced that the permittivity changes by approximately –5% in the band considered. Therefore, a similar change may be attributed to the piezoelectric coefficients as well.

The changes in the elements as a function of stress field are in the order of few percents as well. The reference [52] gives for PZT-5H that the d_{33}-constant changes by –5% and –7% as the stress increases to 10 and 14 MPa, respectively. For PZT-4 the data sheet states that the d_{31}-coefficient decreases by 10% as the stress increases to tens of MPas. PZT-4 being a harder piezo material than PZT-5H, it is more resilient to the stress changes. However, because the stress in the measurement is fairly low (maximum 2 MPa), the changes in the coefficients due to the stress should not be more than -10%.

However, it should be noted that the stress field changes spatially in the piezo structure. Since in the current solution the structure bends, the lower surface of the piezo is under higher stress than the upper surface. This location dependency may introduce unexpected characteristics to the displacement behavior. However, as of now there is no possibility to model this effect properly. Although non-linear materials are possible, the materials

should first be characterized properly. Unfortunately, no extensive measured data sets are available.

Although no significant changes in neither the permittivity nor piezoelectric matrix can be observed at low stress levels, the recent studies have shown that by prestressing the piezo structures significantly, piezoelectric and dielectric characteristics may be optimized for greater displacement levels. Chaplya et al. [18] have shown that by introducing a 50-Mpa to 60-MPa pretension in PZT-5H plates, significant improvements in piezoelectric properties may be obtained. Notable amount of research is currently done on this topic, since it provides yet another means to increase the maximum obtainable displacement. Now, in actuator use thin structures are generally preferred in order to obtain high electric field strength with low voltage. However, the current manufacturing technology cannot handle the combination of a thin fragile structure and high level of pretension. Moreover, the pretension must be set to a correct level with high accuracy, which is yet another complication for commercial exploitation of this otherwise promising technology.

Finally, temperature affects the coefficients significantly. Based on the data presented in [52], the d_{31} and d_{33} coefficients increase by 23% and 71%, respectively, as the temperature rises from 20 to 100˚C. However, these figures mean that increasing the temperature, the piezoelectric coefficients grow and, hence, the displacement increases. If it is assumed that the piezo material warms in the measurement process, then the displacement should in fact be greater than predicted by the FE-model, in which the coefficients are taken at the room temperature. Hence, the temperature effects, although significant, cannot explain the observed behavior.

In conclusion, the known approximations in the mechanical parameters cannot account for the observed discrepancies between the model and the measurements. The modeling error is certainly partly due to these approximations, but based on the above discussion, more significant effects arise from the manufacturing process of the prototype. Already figure 26 shows that there are significant differences between the individual piezo elements. These differences arise from the human factor in their assembly. Still, both measurements presented in figure 26 show a decreasing trend as a function of frequency, which was not captured by the FE-model.

Finally, the attention is turned to the inherent property of the piezoelectric materials not previously introduced in this study, hysteresis. Hysteresis is quoted in the literature to add

damping to the system at high frequencies. Therefore, hysteresis is a potential explanation for the high frequency behavior observed in the measurements, but not in the FE-model. ANSYS does not support the inclusion of hysteresis and, hence, another method must be exploited.

7.6 Hysteresis

7.6.1 Overview

Ferroelectric materials exhibit hysteresis in analogy with magnetic materials. The difference is that in ferroelectrics hysteresis expresses itself between electric field and flux density (E-D curve), not magnetic field and flux density (H-B curve). More commonly, E-D hysteresis is shown on an E-Ψ graph with Ψ being the polarization. An E-Ψ type hysteresis loop is shown in figure 30.

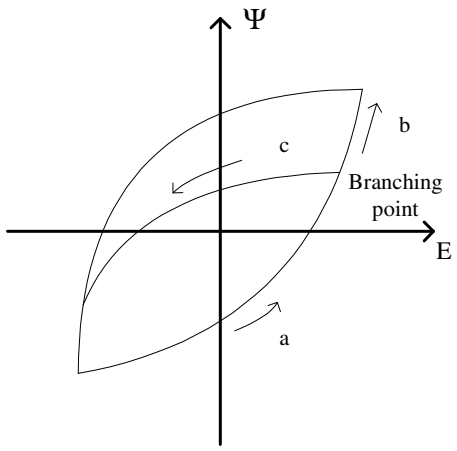

Figure 30. Hysteresis loop. Ψ is polarization.

Hysteresis can be subdivided in irreversible and reversible hysteresis. Irreversible hysteresis is responsible for energy losses in the system and is associated with domain instabilities in the crystal. In contrast, reversible hysteresis is associated with energy stored and released.

According to Bertotti [13], hysteresis may be characterized by *lag, dissipation* and *memory/branching*.

Lag. Lag is associated with phase shift. When a hysteretic system is excited with a harmonic input, the output will be out-of-phase by some phase-angle. This may be presented by

$$\begin{cases} Input(t) = Input_0 \cdot \sin(\omega \cdot t) \\ Output(t) = Output_0 \cdot \sin(\omega \cdot t + \phi) \end{cases}, \tag{85}$$

where ϕ is the phase angle. The treatment is complicated in the real system due to the phase-angle being a function of the input as well as of its history. Moreover, here it was assumed that the harmonic input results in a sinusoidal output at the same frequency. This is true for linear systems, where the superposition holds. However, hysteretic systems are non-linear and, hence, higher harmonics will be present in the output. Non-linear distortion reduces audio-quality and should therefore be compensated for in designing high-quality actuators [51]. [13] [64]

Dissipation. Hysteresis is associated with energy losses in the system. The losses arise from the hysteretic response being an out-of-equilibrium process, in which irreversible sub-processes take place [13]. Energy losses are closely related to friction between domains as their polarization orientation oscillates under periodic excitation. The measure of the energy loss is the area of the hysteresis loop in an E-D-graph, formally

$$\oint_{Cycle} E \, \mathrm{d}D = -\oint_{Cycle} \mathrm{d}Q, \tag{86}$$

which equation gives the energy loss as heat Q per cycle. It is now hypothesized that this energy dissipation is responsible for the decline in the displacement response as a function of frequency.

Memory/branching. Memory is related to the general statement that if a system exhibits hysteresis, its future behavior depends on the past states. Memory effect may further be subdivided in local and non-local memory. With local memory, the future of the system depends on the current state of the system (point on the E-D-curve) and the gradient of the input (i.e. whether the input is increasing or decreasing). In figure 30, this illustrated by the paths a, b and c. Assume the input is increasing from the negative saturation along the path a. Now, if the input increases monotonously until positive saturation is reached, the system behavior follows the lower curve of the major loop (path a-b). However, if at some point along the curve the input is turned decreasing, branching occurs. In such a case, output follows the path c. This is an example, where the evolution of the system is determined by the instantaneous state and the gradient of the input.

With non-local memory, the instantaneous state and the gradient are not sufficient to determine the future of the system. In fact, a given point on the E-D –graph is associated with a set of curves. The choice of the curve depends on the past history of the system. In figure 30 this means that as the system achieves the branching point and the input is turned decreasing, one would not be able to say that the system follows the path c. The full excitation history is needed before the decreasing branch could be defined.

From the modeling point of view, whereas modeling local memory requires rigorous mathematics, non-local memory effects may be accounted for fairly simply by using the Preisach model [49]. Hence, the Preisach model shall be utilized in this study. However, the Preisach model is able to capture only the irreversible part of hysteresis [49]. Nevertheless, in order to model hysteresis properly, the reversible part must also be accounted for [12]. Therefore, another model, called a scalar product model, is utilized for the reversible part [68].

The reader is reminded that the brief discussion above on the main properties of hysteresis is not complete and does not try to be such. Several sources, such as [13], discuss hysteresis phenomena in detail. The reader is encouraged to search for further information from the sources quoted in this text.

The hysteresis treatment is initiated by developing a time-domain model neglecting hysteresis for the current piezo structure.

7.6.2 Linear time-domain model

In the linear model it is assumed that electric field in the piezo material can be directly obtained from the voltage applied across the piezo. Equation (55) then yields

$$\underline{\sigma} = c\underline{e} - g\underline{E}, \tag{87}$$

where $g = c^{(E)}d$ is the inverse piezoelectric matrix. Before proceeding with the derivation, the detailed piezo behavior in the ECE must be considered. Figure 31 shows, how the piezo structure used in the ECE behaves in unclamped and clamped situations.

Piezo is polarized in the 3-direction that is chosen as the z-axis in the analysis. Now, the piezo works in the 3-1 mode. This means that as electric field in 3-direction is applied across the piezo, the material expands (or contracts) in 1-direction. 1-direction is defined

to be the x-axis. Naturally, the piezo responds in 2- and 3-directions as well, but since the 3-1 is the primary mode, the other modes are neglected in the analysis.

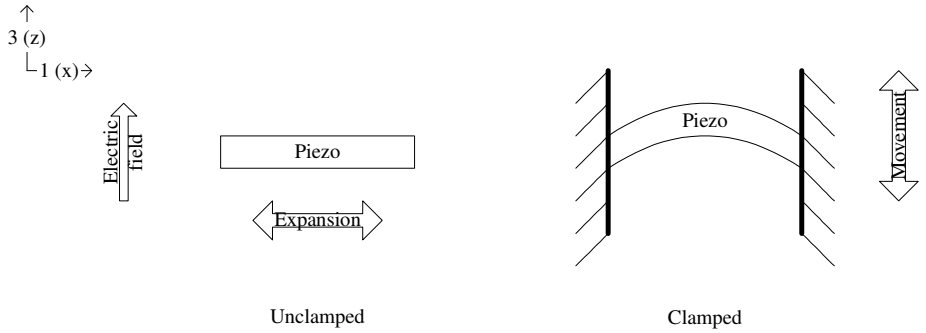

Figure 31. ECE piezo working mode.

However, in the ECE structure, the piezo is clamped in the x-direction. Therefore, the piezo movement takes place in the z-direction resulting in radial vibration. Based on the equation (87) and the reasoning above

$$\begin{bmatrix} \sigma_x \\ \sigma_z \end{bmatrix} = \begin{bmatrix} c_{11} \\ c_{13} \end{bmatrix} e_x - \begin{bmatrix} g_{13} \\ g_{33} \end{bmatrix} E_z , \tag{88}$$

since from the piezo point-of-view there is no expansion in the z-direction, only in x-direction. Moreover, electric field has only the z-component (3-direction). Now, figure 32 shows the dimensions of the piezo structure and the various symbols used for the corresponding measures.

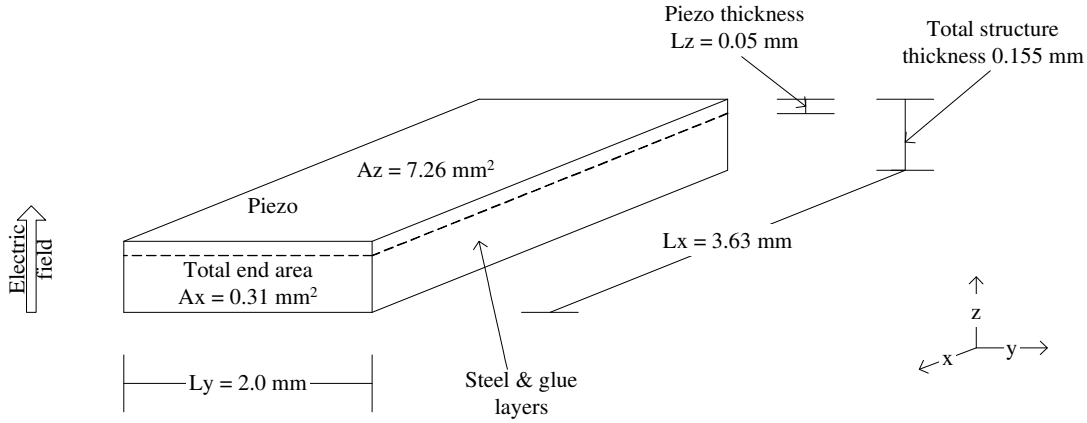

Figure 32. Dimensions for the piezo structure. The structure shown is the true piezo structure used in the ECE. Note that the whole structure with the steel support is considered. As electric field is calculated, the piezo thickness is used instead of the total thickness.

By multiplying the first equation in (88) by A_x and noting that $e_x = \Delta x / L_x$ (Δx is elongation in x-direction) as well as $F_x = \sigma_x A_x$ (F_x is force in x-direction), it is obtained that

$$F_x = A_x \left(\frac{c_{11}}{L_x} \Delta x - g_{13} E_z \right) \tag{89}$$

It seems now that it is straightforward to simulate the piezo movement in x-direction. However, an expression for the movement in the z-direction is required. Therefore, a mechanical 2-port [19] is defined in order to express the coupling between the movement in x- and z-directions. The 2-port may be expressed by

$$\begin{bmatrix} F_x \\ F_z \end{bmatrix} = \begin{bmatrix} C_{11} & C_{13} \\ C_{13} & C_{33} \end{bmatrix} \begin{bmatrix} \Delta x \\ \Delta z \end{bmatrix}, \tag{90}$$

where F_z and Δz are force and elongation in the z-direction, respectively.

The detailed method on how to extract the matrix coefficients C_{11}, C_{13} and C_{33} from the FE-analysis, is presented in the appendix C. It is worth mentioning that in determining the matrix elements, the complete stiffened piezo structure including the steel and glue layers is considered. Only then the analysis takes into account the correct stiffness, mass and boundary conditions.

Combining (89) and (90) yields for the elongation Δx

$$\Delta x = -\frac{C_{13}}{C_{11} - \frac{A_x c_{11}}{L_x}} \Delta z - \frac{g_{13} A_x}{C_{11} - \frac{A_x c_{11}}{L_x}} E_z, \tag{91}$$

from which it follows with (90) that

$$F_z = \left(C_{33} - \frac{C_{13}^2}{C_{11} - \frac{A_x c_{11}}{L_x}} \right) \Delta z - \frac{C_{13} g_{13} A_x}{C_{11} - \frac{A_x c_{11}}{L_x}} E_z \tag{92}$$

Finally, since there is no load on the system, the differential equation (93) is obtained for the movement of the piezo.

$$0 = m_{eff}\ \ddot{z}(t) + \left(C_{33} - \frac{C_{13}^2}{C_{11} - \frac{A_x c_{11}}{L_x}} \right) \cdot z(t) - \frac{C_{13} g_{13} A_x}{C_{11} - \frac{A_x c_{11}}{L_x}} E_z(t), \tag{93}$$

where mass of the system is the effective mass, m_{eff}, that is determined from the FE-analysis. Moreover, Δz has been replaced by the true coordinate, *z(t)*.

Assuming harmonically varying input and output, performing a Fourier transform and writing $E_z(t) = v(t)/L_z$, it is obtained for the transfer function $z(i\omega)/v(i\omega)$ that

$$\left| \frac{z(i\omega)}{v(i\omega)} \right| = \left| \frac{\frac{C_{13} g_{13} A_x}{C_{11} - \frac{A_x c_{11}}{L_x}} \frac{1}{L_z}}{C_{33} - \frac{C_{13}^2}{C_{11} - \frac{A_x c_{11}}{L_x}}} \cdot \frac{1}{1 - \omega^2 \frac{m_{eff}}{C_{33} - \frac{C_{13}^2}{C_{11} - \frac{A_x c_{11}}{L_x}}}} \right| \tag{94}$$

Further, the first mechanical resonance frequency ω_0 is defined by $\omega_0^2 = k_{eff}/m_{eff}$ and, hence,

$$\left| \frac{z(i\omega)}{V(i\omega)} \right| = \left| \frac{\frac{C_{13} g_{13} A_x}{C_{11} - \frac{A_x c_{11}}{L_x}} \frac{1}{L_z}}{C_{33} - \frac{C_{13}^2}{C_{11} - \frac{A_x c_{11}}{L_x}}} \right| \cdot \frac{1}{1 - \omega^2 \left(\frac{m_{eff}}{k_{eff}} \right)} = \left| \frac{\frac{C_{13} g_{13} A_x}{C_{11} - \frac{A_x c_{11}}{L_x}} \frac{1}{L_z}}{C_{33} - \frac{C_{13}^2}{C_{11} - \frac{A_x c_{11}}{L_x}}} \right| \cdot \frac{1}{1 - \left(\frac{\omega}{\omega_0} \right)^2}, \tag{95}$$

where

$$k_{eff} = C_{33} - \frac{C_{13}^2}{C_{11} - \frac{A_x c_{11}}{L_x}}. \tag{96}$$

Now, from the datasheet [52] it is obtained that $c_{11} = 12.6 \cdot 10^{10}$ N/m^2 and g_{13}=-6.55 Nm^{-2}/Vm^{-1} for PZT-5H. The linear response is calculated in two ways. Firstly, equation (95) provides a straightforward method to predict the piezo displacement transfer function.

Secondly, the time domain equation (93) can be solved analytically as well as numerically. The differential equation was solved numerically in Matlab [47] in order to validate the solving method for further use with the non-linear model taking hysteresis into account. Figure 33 summarizes results from both analyses.

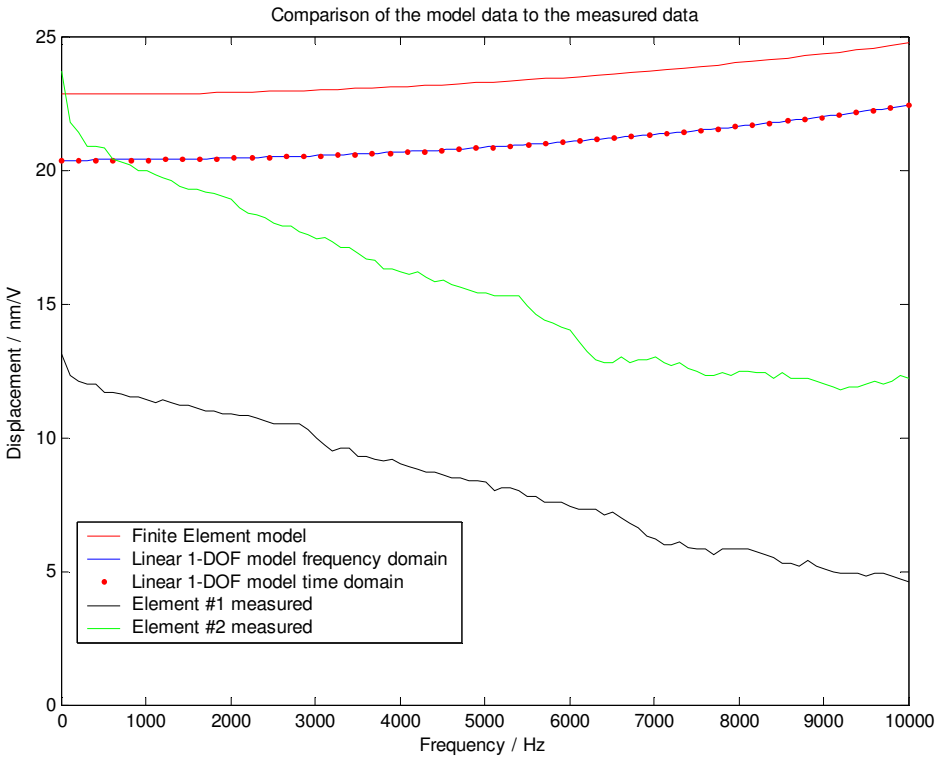

Figure 33. Results from the linear models.

Figure 33 shows that the linear model developed is successful in predicting the response. Clearly, the linear model cannot account for hysteresis, or any other non-linear effect. However, the response predicted by the model developed follows closely that of obtained from the FE-analysis. The similarity of the frequency responses arises from using the FE-model produced resonance frequency and effective mass in the linear model. It is still, however, encouraging that the linear model predicts the static displacement correctly. This can be used as an argument for the validity of the 2-port model utilized.

Moreover, figure 33 also shows that the responses from the time and frequency domain analyses match. This is important, since with the non-linear model, it is impossible to derive the frequency response directly. As the non-linear model is considered, the frequency response is determined solely based on the time-domain behavior.

7.6.3 Non-linear time domain model

The derivation is initiated by rewriting the equation (55).

$$\begin{bmatrix} \underline{\sigma} \\ \underline{D} \end{bmatrix} = \begin{bmatrix} c^{(E)} & -g \\ g^T & \varepsilon^{(\sigma)} \end{bmatrix} \begin{bmatrix} \underline{e} \\ \underline{E} \end{bmatrix} \qquad \text{(55) rewritten}$$

In order to take the hysteresis into account, the latter equation $\underline{D} = g\underline{e} + \varepsilon^{(\sigma)}\underline{E}$ must be rewritten in the form

$$\underline{D} = g^T \underline{e} + \varepsilon_0 \underline{E} + \frac{1}{3}\Psi(E_{history}), \qquad (97)$$

[61] [63]. The notation that Ψ is the function of $E_{history}$ underlines the property that the instantaneous polarization is not only a function of the current value of electric field, but also of its history. Moreover, it should be noted that now electric field $\underline{E}$ is not the voltage applied divided by the piezo thickness, but the real electric field acting inside the piezo. If one can now calculate the true $\underline{E}$, the piezo movement may then be predicted by substituting the true $\underline{E}$ in equation (93).

Now, equation (97) implies that

$$E_z = \frac{1}{\varepsilon_0}\left[D_z - \underline{\hat{z}} \bullet \left[g^T \underline{e} \right] - \frac{1}{3}\Psi(E_{history}) \right], \qquad (98)$$

where $\underline{\hat{z}}$ is the unit vector in the z-direction. Firstly, the term $\underline{\hat{z}} \bullet \left[g^T \underline{e} \right]$ can be obtained by combining equations (91) and (98) to yield

$$\begin{aligned} \underline{\hat{z}} \bullet \left[g^T \underline{e} \right] &= g_{13}\frac{\Delta x}{L_x} = -\frac{g_{13}C_{13}}{C_{11}L_x - A_x c_{11}} z - \frac{g_{13}^2 A_x}{C_{11}L_x - A_x c_{11}} E_z \\ &= -\frac{g_{13}C_{13}}{C_{11}L_x - A_x c_{11}} z - \frac{g_{13}^2 A_x}{C_{11}L_x - A_x c_{11}} \frac{1}{\varepsilon_0}\left[D_z - \underline{\hat{z}} \bullet \left[g^T \underline{e} \right] - \frac{1}{3}\Psi(E_{history}) \right] \end{aligned}, \qquad (99)$$

from which it directly follows

$$\underline{\hat{z}} \bullet \left[g^T \underline{e} \right] = \frac{-\frac{g_{13}C_{13}}{C_{11}L_x - A_x c_{11}} z - \frac{g_{13}^2 A_x}{C_{11}L_x - A_x c_{11}} \frac{1}{\varepsilon_0}\left[D_z - \frac{1}{3}\Psi(E_{history}) \right]}{1 - \frac{g_{13}^2 A_x}{C_{11}L_x - A_x c_{11}} \frac{1}{\varepsilon_0}} \qquad (100)$$

Moreover, an expression for the electric flux in the z-direction, D_z, is required. Since no better approximation is known, the linearized charge-voltage relation is utilized. Therefore, by the Gauss's law it is obtained

$$D_z \cdot A_z = q \cdot V = C_e \cdot v \tag{101}$$

and

$$D_z = \frac{C_e}{A_z} v \,. \tag{102}$$

The choice may be justified by figure 29, which shows that the capacitance changes only by 5%, when frequency increases from 0.1 to 10 kHz. Therefore, in the lack of more rigorous method for determining D_z, constant capacitance may safely be assumed.

Finally, by combining (93), (98), (100) and (102) as well as moving the origin so that the acceleration is zero, when $z(t) = v(t) = 0$, the differential equation to be solved becomes

$$\begin{aligned} 0 = m_{eff}\, \ddot{z}(t) + & \left(C_{33} - \frac{C_{13}^2}{C_{11} - \frac{A_x c_{11}}{L_x}} - \frac{\left(\frac{C_{13} g_{13}}{C_{11} L_x - A_x c_{11}} \right)^2 A_x L_x}{\varepsilon_0 - \frac{g_{13}^2 A_x}{C_{11} L_x - A_x c_{11}}} \right) \cdot z(t) \\ & + \frac{1}{\varepsilon_0} \frac{C_{13} g_{13} A_x}{C_{11} - \frac{A_x c_{11}}{L_x}} \cdot \left(1 + \frac{\frac{g_{13}^2 A_x}{C_{11} L_x - A_x c_{11}}}{\varepsilon_0 - \frac{g_{13}^2 A_x}{C_{11} L_x - A_x c_{11}}} \right) \cdot \left[-\frac{C_e}{A_z} v(t) + \frac{1}{3} \Delta\Psi(t) \right] \end{aligned} \tag{103}$$

The remaining unknown is the change of polarization, $\Delta\Psi(t)$, about the remanence polarization. Predicting the polarization $\Psi(E_{history})$ shall therefore be considered next.

7.6.4 Scalar Preisach model for hysteresis

Preisach model has successfully been applied in various hysteresis problems [64]. Before introducing the model in more detail, it should be noted that the Preisach model is defined without any reference to the underlying physics. Therefore, the Preisach model is a purely phenomenological description of hysteresis. Moreover, the Preisach model is generally applied to magnetic problems, but few sources, such as [63], have successfully utilized the model to piezoelectric problems as well. Reference [34] notes that the Preisach model may

be applied on the piezoelectric materials only if the load applied on the actuator is small. Since there was no load applied in the response measurements, the Preisach model is applicable.

The Preisach model may be explained in magnetic terms as follows [49]. Magnetic materials are considered to consist of magnetic domains that have rectangular hysteresis loops. Such a domain is analogous with an elementary Preisach operator shown in figure 34. The operator, or domain, has up and down switching values of ζ_1 and ζ_2, respectively. Since magnetic material is a collection of such domains, or operators, it is reasonable to assume that they have some distribution $p(\xi_1, \xi_2)$. The distribution is often considered to have statistical nature, although there is no physical reason, why it should have such.

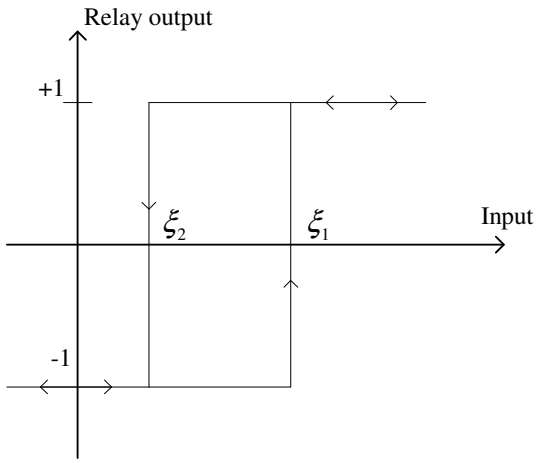

Figure 34. Elementary Preisach operator $\Gamma_{\zeta 1,\zeta 2}$ with switching values ζ_1 and ζ_2.

Finally, with the knowledge of the input, electric field *E(t),* and the distribution of the operators, the output, polarization $\Psi_{PREISACH}(t)$, can be given by

$$\Psi_{PREISACH}(t) = \iint_{\xi_1 \geq \xi_2} p(\xi_1, \xi_2)\Gamma_{\xi_1,\xi_2} E(t)\, \mathrm{d}\xi_1\, \mathrm{d}\xi_2 \,, \tag{104}$$

where Γ_{ξ_1,ξ_2} is the elementary hysteresis operator with switching values of ζ_1 and ζ_2. Now as the input changes, elementary operators are turned on and off based on their switching values and distribution. The integration limits depend on the input.

In this work, Lorentzian distribution is utilized [33]. Lorentzian distribution is given by

$$p(\xi_1,\xi_2) = N(\sigma_c,H_0)\cdot\left[1+\left(\frac{\xi_1-H_0}{\sigma_c H_0}\right)^2\right]^{-1}\left[1+\left(\frac{\xi_2+H_0}{\sigma_c H_0}\right)^2\right]^{-1}, \tag{105}$$

where σ_c and H_0 are the distribution parameters. Moreover, the normalization constant $N(\sigma_c,H_0)$ must fulfill the condition

$$\iint\limits_{1\geq\xi_1\geq\xi_2\geq-1} p(\xi_1,\xi_2)\,\mathrm{d}\xi_1\,\mathrm{d}\xi_2 \equiv 1 \tag{106}$$

Details of the implementation are not summarized here, but the output prediction was realized using the Everett function [32] [33] [49].

However, the Preisach model itself is not sufficient to describe hysteresis completely, since it lacks the reversible part of hysteresis. Hence, the reversible part must be added to the model. The complete polarization, $\Psi(t)$, accounting for both types, is given by

$$\Psi(t) = \Psi_{IRREVERSIBLE}(t) + \Psi_{REVERSIBLE}(t) = \Psi_{PREISACH}(t) + \Psi_{REVERSIBLE}(t)\,. \tag{107}$$

Hysteresis has a reversible part whenever the elementary hysteresis loops have non-rectangular shapes. This is the case with soft magnetic materials. [12] Since PZT-5H is soft piezoelectric material, it seems justified to include the reversible part in the analysis as well.

Finally, the scalar product model includes that the total polarization may be expressed by

$$\Psi(t) = \frac{\tanh(\gamma_1\cdot\Psi_{PREISACH}(t) + \gamma_2\cdot E_z(t))}{\tanh(\gamma_1+\gamma_2)}, \tag{108}$$

where γ_1 and γ_2 are weights for the irreversible and reversible hysteresis, respectively. [68] [17]

7.6.5 Hysteresis model fitting

The model defined by equations (104), (105) and (108) was fitted to the measured data by the least squares minimization [32]. Training data was measured from a non-polarized piezo structure introduced earlier. Since the piezos used in the ECE were polarized under the 1.5-MVm^{-1} electric field, a hysteresis measurement, in which *E* oscillates between

±1.5 MVm^{-1}, was selected for training data. The fitting procedure yields for the model parameters $\sigma_c = 0.38$, $H_0 = 0.42$, $\gamma_1 = 0.66$ and $\gamma_2 = 0.09$.

Figure 35 shows the measured and modeled major loops on normalized scales. In absolute terms, the maximum electric field and polarization were 1.5 MVm^{-1} and 0.2557 Cm^{-2}, respectively. The remanence polarization after the polarization process was 0.201 Cm^{-2}.

Figure 35 also shows the close correspondence between the measurement and the simulation. It was also noticed that adding the reversible part to the total hysteresis improved the accuracy of the fit significantly. It may therefore be concluded that adding reversible hysteresis to the model was justified.

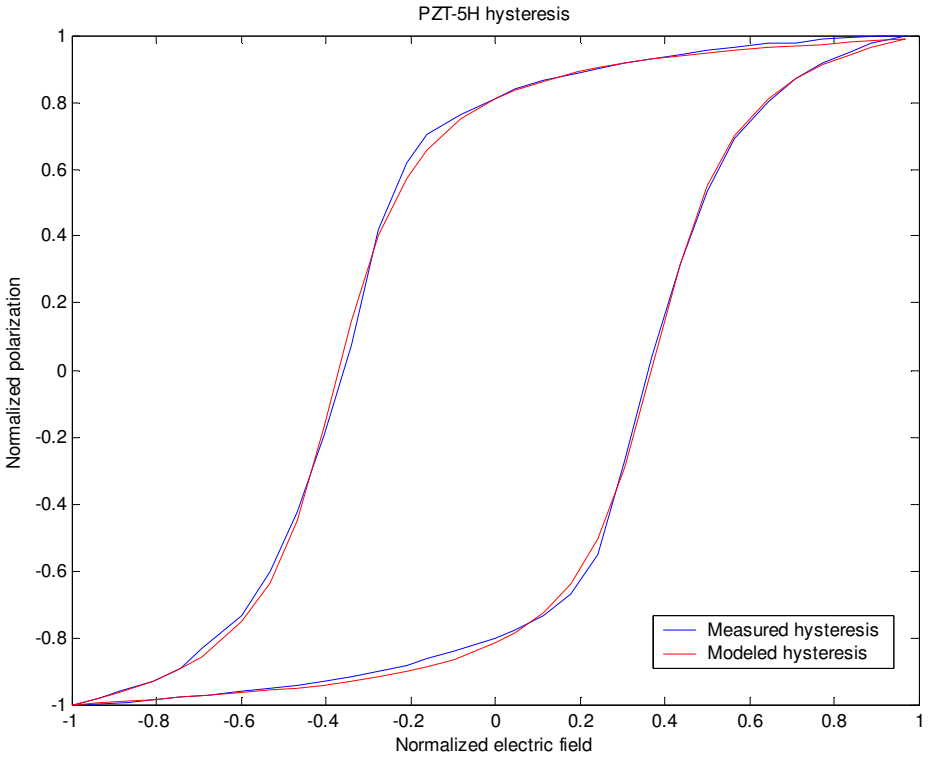

Figure 35. Measured and modeled hysteresis major loops. The maximum absolute electric field and polarization are 1.5 MVm^{-1} and 0.2557 Cm^{-2}, respectively. Hysteresis measurements were performed in the University of Oulu with DC excitation.

The hysteresis model definition now allows for solving the time-domain equation (103) with equation (108). Solving is performed in Matlab with a stiff ODE-solver. It should be noted that at each time step, equations (98) and (108) must be balanced iteratively in order to approximate the polarization and electric field.

7.6.6 Results and discussion

Figure 36 shows the output waveform (displacement) from the piezo as it is excited with a 1-V_p 1-kHz input signal. Firstly, the results show that the amplitude of vibration is considerably higher than expected. Based on the measurements as well as linear model predictions, one might expect to obtain displacement levels in the vicinity of 20 nm (figure 33). Hence, the vibration level now obtained is 7-8 times higher than predicted by the FE-model. The reason for the erroneous level may be in slightly incorrect values for the 2-port matrix elements. Inspection of equation (103) reveals that the acceleration is very sensitive to the errors in areas, lengths or C-matrix elements due to the division of some terms by ε_0. On the other hand, the error in the overall displacement level may reveal an error in the whole approach to the problem. One such potential error is the use of the actuator capacitance in determining the electric flux density. Despite the uncertainties in displacement levels, the model is hoped to provide information on the effect of hysteresis on the actuator performance.

In addition, figure 36 reveals that the addition of hysteresis has introduced a bias component in the displacement response. It may be observed that while the response achieves +187 nm at the positive side, only –145 nm is achieved at the negative side.

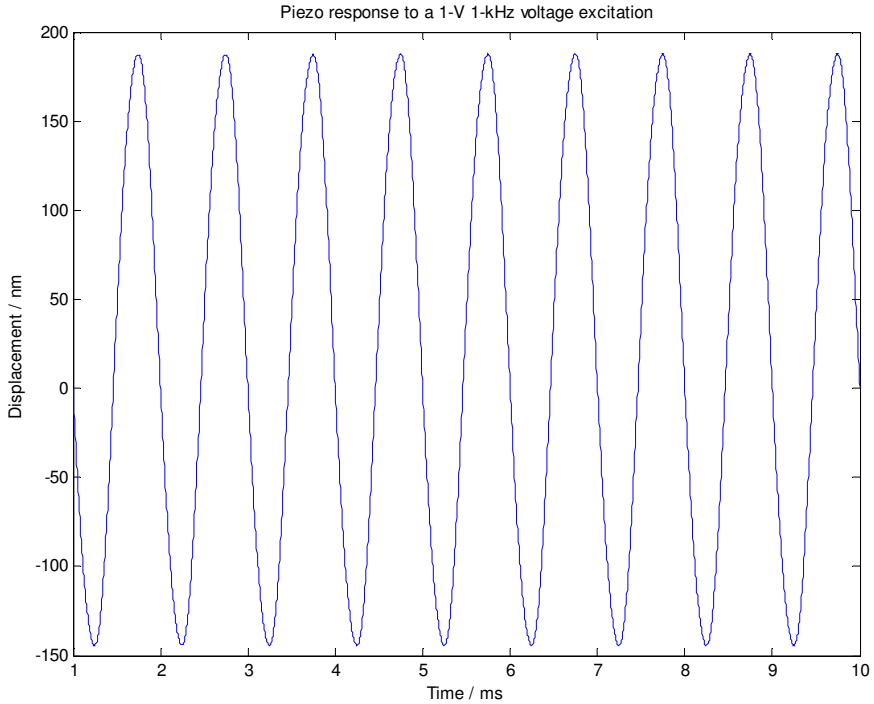

Figure 36. Piezo response under 1-volt 1-kHz excitation. Note that there is an induced dc-component in the output signal.

Such a behavior may be understood by figure 37. It represents modeled hysteresis loops for the actuator under the 1-V excitation at 1 and 10 kHz. Figure clearly shows that the loop is asymmetrically placed with respect to the rest state. The rest state is defined as having zero electric field and remanence polarization of 0.201 Cm^{-2}. Since electric field behaves in a biased manner, so does the acceleration and ultimately also the displacement. Similar behavior is quoted in [63]. The bias in electric field may be understood by noting that the permanent polarization introduced in the polarization process tries to compensate, or neutralize, the reversing negative electric field. Hence, the negative field direction does not achieve such high amplitudes. The behavior does not, however, cause problems for the audio reproduction, since once the bias is known, it may be compensated for by a suitable bias in the driving signal.

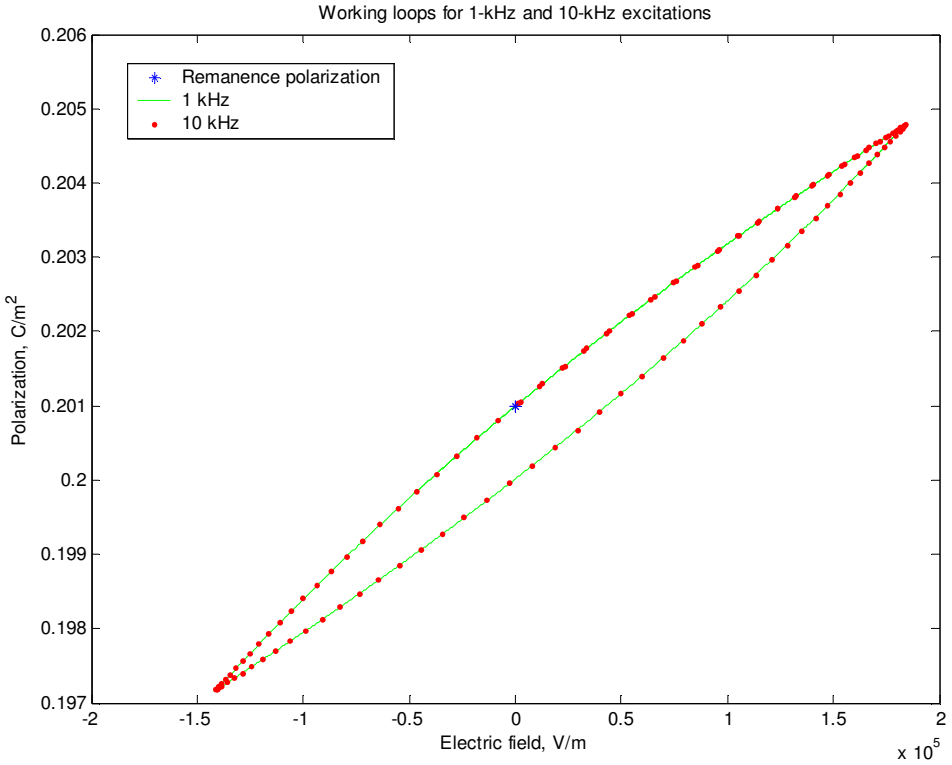

Figure 37. Actuator working loops on an E-Ψ -graph. Note that the loop shape is independent of the excitation frequency. Moreover, the bias in electric field is clearly observable. Each analysis was commenced with zero electric field and true measured remanence polarization.

The surprising finding is that no higher harmonics are present in the output signal. It was noted above that non-linear processes, such as hysteresis, generate higher harmonics. However, the signal waveform in figure 37 is free from such distortion. Naturally, the lack of harmonics induces questions on the validity of the model. However, it may also be that

higher harmonic generation only occurs at high frequencies. For frequencies up to 10 kHz, no harmonics generation was observed.

Figure 37 also shows that the hysteresis loops are independent of the excitation frequency. Hence, the energy loss per cycle, which is associated with the area of the loop by equation (86), is the same for both frequencies. The consequence of this finding is that the hysteretic losses, as predicted by the rate-independent Preisach model, do not affect the response at high frequencies such significantly that the losses would account for the measured decline in the displacement response. This behavior is shown in figure 38.

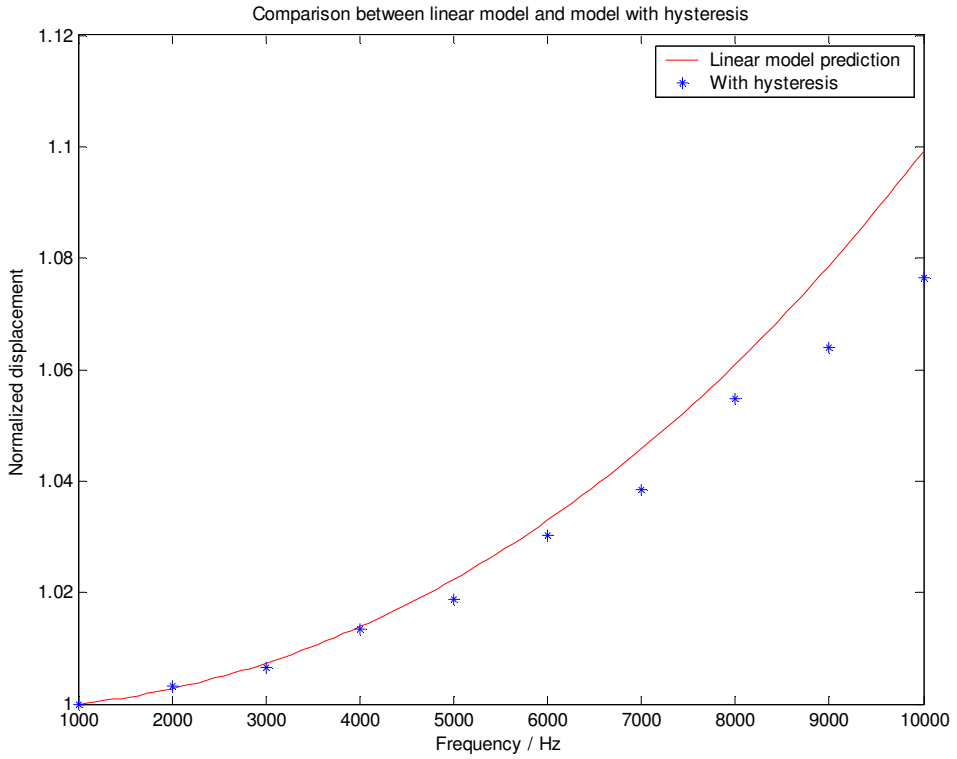

Figure 38. Comparison between the linear model and the model with hysteresis. The displacements have been normalized in such a way that both have a minimum displacement of 1 at 1 kHz.

In figure 38, data has been normalized in such a way that both, the linear model and the model with hysteresis, have an output of 1 at 1 kHz. The normalization is performed in order to turn the attention to the frequency behavior and not on the absolute displacement values. Figure 38 now shows that the model with hysteresis is not able to explain the measured decline in the response. Although the hysteretic model predicts somewhat lower displacement levels throughout the band, the response is clearly not declining. Figure 26, which summarizes the measurements, shows that the displacement response halves as the

frequency increases from 1 to 10 kHz. Hence, the classical Preisach model is not sufficient to explain the observed piezo behavior.

Despite the conclusion on the capabilities of the classical Preisach model in the current modeling problem, the model is able to capture yet another interesting property of hysteresis. Figure 39 shows the hysteresis behavior as the displacement is considered. Figure reveals, how increasing the frequency significantly affects the loop shape, area and positioning. This finding is partly in accordance with the results in [73]. However, the measurement results in [73] show that the changes in the loop tilts occur in the other direction as now observed. In the current model, the major axis angle with respect to the horizontal increases with increasing frequency, whereas in [73] the angle decreases. It may be concluded that more measurement data on the current piezo structure is required in order to evaluate the model in this respect.

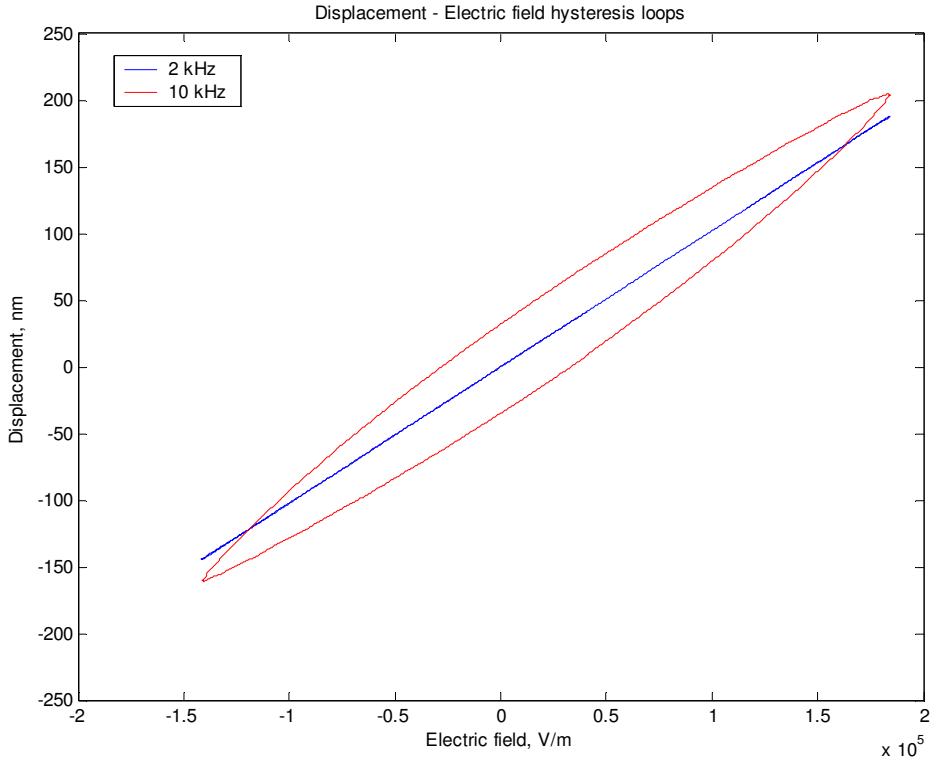

Figure 39. Displacement – Electric field hysteresis loops for 2- and 10-kHz excitations.

An issue still unaccounted for in the current model is the input rate-dependency. A modification of the Preisach model, called dynamic Preisach model, accounts for the time changes in the excitation signal [48]. In fact, it is known [34] that the accuracy of the

classical Preisach model not accounting for time effects decreases with increasing frequency. The model is accurate only at the frequency at which the training data was measured. If a classical Preisach model is to be used for various frequencies, the model should be fitted individually for each frequency. This requirement can be justified by noting that the hysteresis loop shape and area vary depending upon the excitation frequency [34] [45].

In fact, the H-B -loop area has been shown to increase with increasing frequency in soft magnetic materials [11]. The analogies between ferromagnetic and ferroelectric materials imply that the E-Ψ -loop area increases as a function of frequency in ferroelectric materials as well. The increase in the loop area leads to increased losses and, hence, presumably to lowered response. However, specifically the dynamic Preisach model was utilized to capture the frequency-dependent loop area in [11]. In conclusion, in order to improve modeling accuracy and determine more conclusively, whether hysteresis is the primary cause for the observed decline in response, the rate-dependent Preisach model must be implemented.

Having discussed hysteresis, yet another interesting hypothesis for the response decline is introduced, namely viscous effects. Yu et al. [73] quote similar behavior in the displacement response below the first mechanical resonance as now observed in the measurements. Yu et al. conclude that structural dynamics does not explain the observed behavior and, hence, they turn their attention to creep. They describe that as step voltage is applied on a piezo, there will be an immediate change in the strain followed by a delayed action. Therefore, as frequency increases, piezo will not have enough time to settle to the maximum displacement. Such creep is then observed as a declining response. The important conclusion in the paper is that Yu et al. claim to be successful in modeling low-frequency (below first mechanical resonance) hysteretic behavior with dynamic Preisach model. This finding can be used as a further argument for the need for implementing a dynamic Preisach model in the future model development.

8. ECE PERFORMANCE CHARACTERIZATION

A set of measurements was performed in order to evaluate the ECE performance in real usage circumstances. Both functions, actuator and sensor, were evaluated.

The actuator measurements are particularly challenging, since the evaluation is based on the testee's subjective experience on the sensation of sound produced by ECE. In addition, the situation is complicated because of the acoustic radiation produced by the ECE structure inside the tympanic canal. The challenge is to be able to differentiate between the sensation of sound resulting from acoustic radiation and mechanical vibration. The distinction can be done indirectly by first evaluating the sensed SPL in an acoustic-only condition and thereafter in a combined situation. Acoustic radiation from the ECE cannot be suppressed, but the ECE can be mechanically isolated from the ear structure. Ultimately, the increase in the sensed SPL in the combined situation is due to the mechanical vibration induced by the ECE to the ear structure.

The sensor function must also be characterized with human subjects, but the case is more straightforward, since no subjective evaluation is required. In order to characterize the transfer path from the sound producing organs to the ECE, a speech sample read by the testee is recorded with a microphone and the ECE. The transfer function between the recorded signals yields the transfer path characteristics including tissues, tissue-ECE coupling as well as the ECE vibration characteristics.

8.1 Actuator function

In the chapter 5, a FE-model describing the ECE transfer path was developed. Moreover, the model predictions were summarized in the chapter 5.8. Based on the model developed, the ECE actuator function was deemed unusable. However, the various assumptions and simplifications led to the conclusion that the results are only preliminary and must be verified by measurements.

The proposed measurement setup for the current problem is as follows. A set of test persons are made to compare the perceived sound pressure levels from the ECE and headphones. The ECE is inserted in one canal and an insert-type headphone in the other. Now, a sinusoidal single-frequency tone is fed to the both actuators. The test person then adjusts the gain in such a way that one perceives a centered stereo-image. Having

completed this phase, the both actuators are inserted in the tympanic canal of the Brüel&Kjær Head and Torso Simulator (HATS). The HATS canal mimics the acoustic impedance of the real canal and, hence, provides a suitable test platform for the ECE. It should be noted that the HATS ear does not detect the mechanical vibration induced by the ECE in the structure, but only the acoustic output.

The HATS measurement therefore produces data on the acoustic output of the ECE device as well as on the SPL produced by the insert type. By carefully calibrating the HATS microphones as well as taking into account the differences in the hearing threshold between the ears of the test person, an estimate on the amount of mechanically induced perceived SPL can be obtained. However, the proposed measurement is both time consuming as well as exhausting. The risks include that subjective measurements may produce data with substantial variance despite large number of repetitions.

The impressions on the ECE performance in actuator function qualitatively confirm the model predictions. The test persons detected no apparent increase in the perceived SPL between the case of having the ECE in concha not touching the ear structure and of having the ECE in the ear canal coupled to the canal structure. Based on these first impressions, it was decided not to pursue the actuator tests further. This is because the first impressions already fulfill the requirement for the prototype to provide proof-of-concept data. Clearly, the project was set to look for an improvement of tens of decibels, which increase in the perceived SPL would be clearly detectable. Therefore, it is insignificant to deduce whether the increase in the perceived SPL level is 0 or 3 dB, when for the concept to work, an improvement of greater than 10 dB is required.

In conclusion, the ECE produced sensation of sound is purely acoustic with no added perceived SPL from the mechanical-only path.

8.2 Sensor function

8.2.1 Measurement setup

In the sensor characterization the test person is given an extract to read. The sample is then recorded with a normal acoustic microphone and the ECE. The transfer function between the two signals yields the transfer path characteristics.

Figure 40 shows the measurement system used in the sensor characterization. The actual speech sample read by the test person is recorded with the reference microphone, amplified and A/D-converted with a *Hammerfall DSP Multiface* -system.

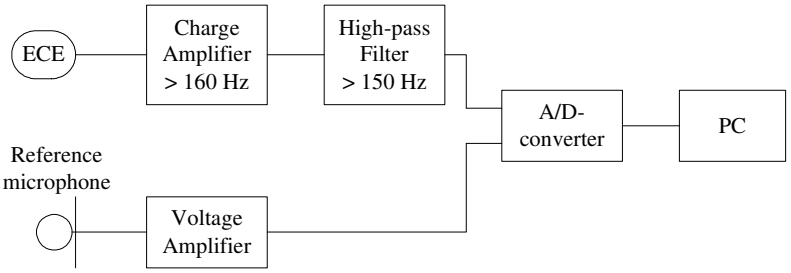

Figure 40. Measurement setup for the sensor function characterization.

The ECE-produced signal must also be amplified, but since piezoelectric materials produce polarization, not voltage, based on the strain state, a charge amplifier must be used. Moreover, additional complications to the measurements were introduced by the high output-impedance of the ECE. The impedance characteristics have an adverse effect on the signal-to-noise ratio (SNR) due to the high level of electrical noise induced in the transfer line between the ECE and the charge amplifier. The best solution would have been to have an impedance converter directly in the ECE device, but since this would have required a new prototype, such a converter was not implemented. However, reasonable performance was achieved by using a differential charge amplifier that amplifies only the differential mode. The schematics for the amplifier built is included in the appendix A.

It should be noted that the amplifier itself works as a high-pass filter with a cut-off frequency of 160 Hz. However, due to the high level of low-frequency noise, an additional high-pass filter with a cut-off frequency of 150 Hz was included in the system. After filtering, the ECE signal is A/D-converted and recorded on a PC.

Figure 41 shows, how the ECE couples to the air. The characteristics was measured by installing the microphone and the ECE approximately 50 cm from a loudspeaker, playbacking a sine-sweep from 0.2 to 10 kHz several times and recording the microphone and ECE output. The transfer function between the recordings is a measure of how the ECE couples to the air.

Firstly, figure 41 shows that the outputs correlate well (coherence graph in blue) and, hence, the measured transfer characteristics may be relied upon. Secondly, it is observed

that the acoustic sensitivity of the ECE increases rapidly in the region from 3 to 5 kHz, reaches a maximum at approximately 6 kHz and then decreases again. It shall be seen that this high-frequency acoustic sensitivity is observable also in the in-ear measurements. On the other hand, poor acoustic sensitivity at low frequencies is advantageous in the planned usage case, since disturbing noise generally occurs in that region [38].

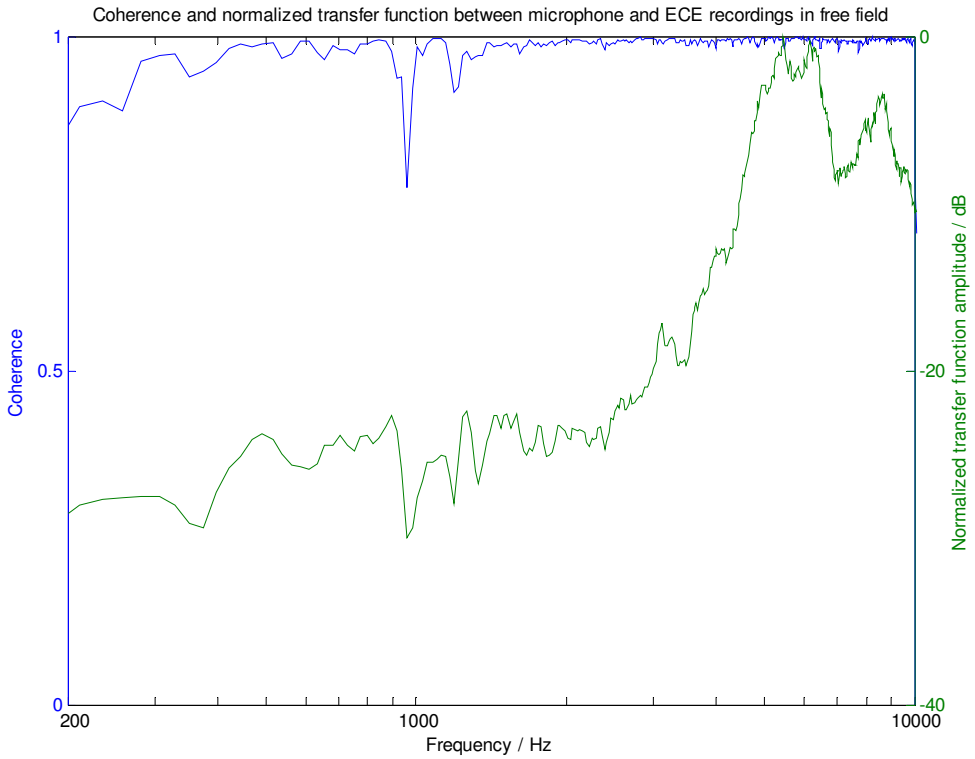

Figure 41. Pressure transfer characteristics of ECE.

Figure 42 shows the general characteristics of the speech sample as recorded by the microphone and the ECE as well as the noise characteristics for both recording mechanisms in a typical measurement case. Firstly, figure 42 shows that the speech sample used contains energy throughout the interesting band from 0.1 to 10 kHz. The speech energy is well (approximately 50 dB) above the microphone noise floor throughout the band.

The ECE measurement, on the other hand, shows the typical problem associated with piezo measurements. Firstly, the SNR is fairly low. Speech energy is generally only 10 dB above the ECE noise floor. Although figure 42 only shows relative levels, also the absolute noise level in the ECE recordings was observed to be very high due to the impedance mismatch problems between the ECE piezo and cabling. Moreover, without

yet going into a detailed discussion on the tissue transmission characteristics, it is apparent from the figure that the ECE performance degrades with increasing frequency. The energy diminishes faster with increasing frequency in the ECE recording than in the microphone case.

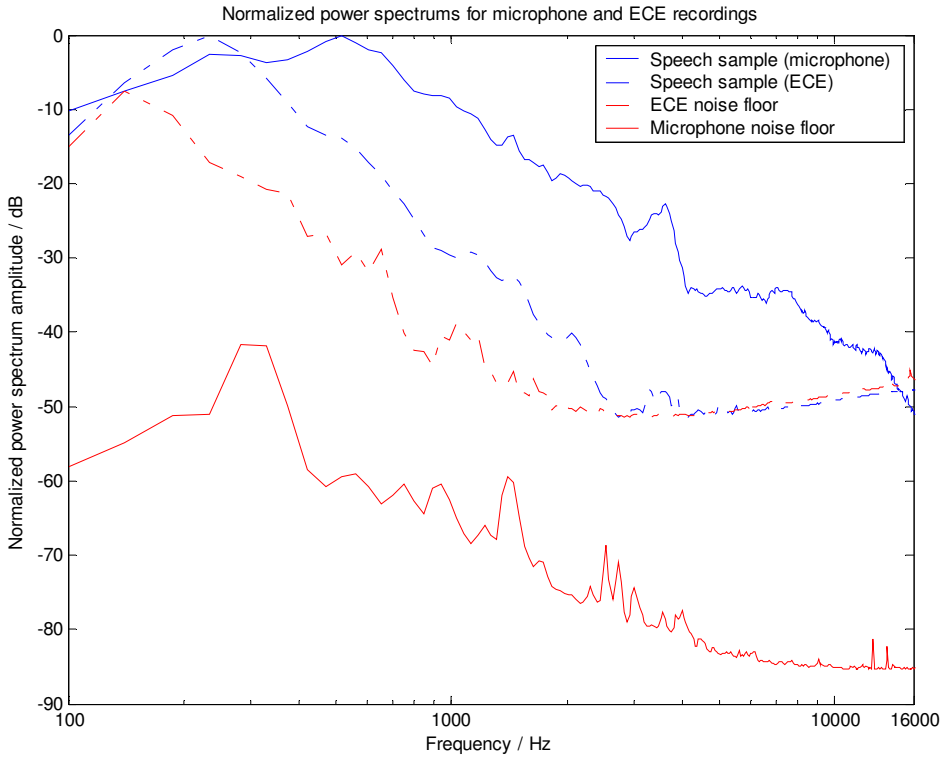

Figure 42. Characteristics of the speech sample and noise for the microphone and ECE system. The data for microphone and ECE recordings have been normalized independently in such a way that microphone and ECE recorded speech samples both have a maximum relative power of 0 dB.

8.2.2 Results

In sum three measurement cases were considered. Because of the noise problems and difficulties with inserting the ECE properly inside the tympanic canal, only one testee was used. However, it is believed that the general characteristics of the transfer path are adequately characterized by using only one testee. Each measurement case is repeated three times in order to minimize the errors due to the improper insertion of the ECE in the tympanic canal.

Measurement cases include a measurement with tympanic canal closed (i.e. the copper tube in the middle of the ECE frame is blocked), a measurement with canal open (i.e. the copper tube open in order to make the ECE transparent to the external sounds) and a

measurement with ear covered with an ear defender in order to prevent the ECE from picking up any acoustic signal from the surroundings.

I *Tympanic canal closed*. Figure 43 summarizes the results from the case, in which the tympanic canal is closed. It can be noted that the transfer function has a general decreasing characteristics with the transfer function declining down to the noise floor at about 2.5 kHz. The transfer function hitting the noise floor is also visible in the coherence graph at the same frequency.

The response shows a dip at approximately 900 Hz and a similar notch is visible in the pressure response in figure 41, as well. Although such a dip might not be expected to occur based on the displacement response shown in figure 26, the notch may, for instance, be caused by a change in the vibration characteristic due to prestress. The prestress occurs in the sensor structure because of the silicone rings and tight insertion in the tympanic canal.

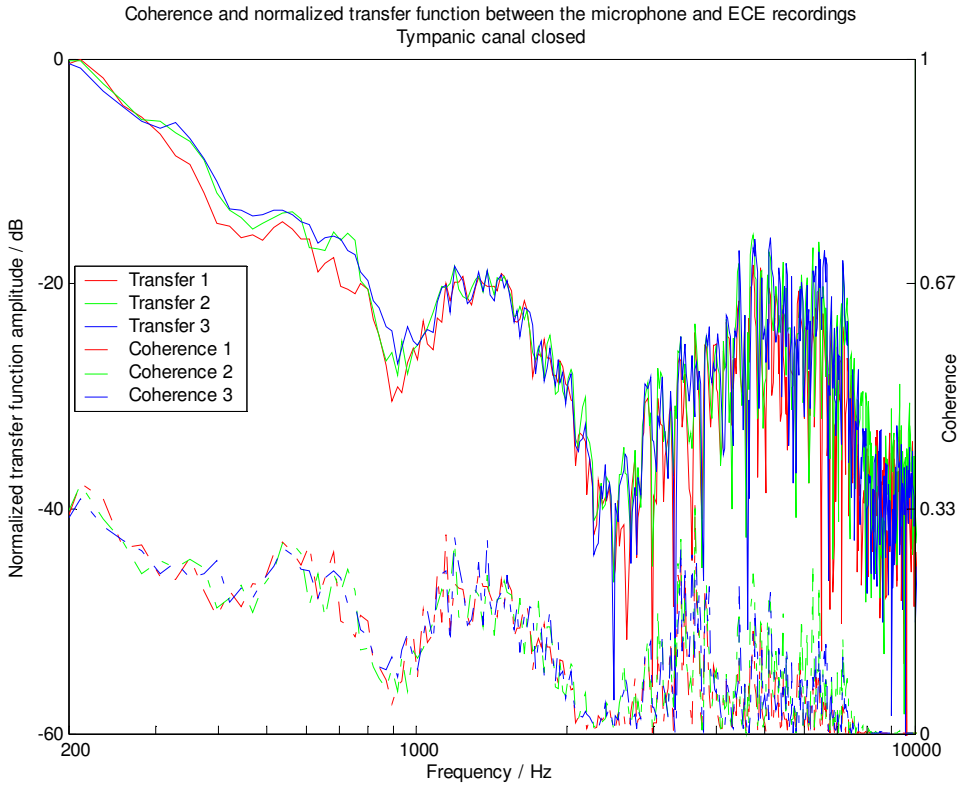

Figure 43. Transfer function and coherence between microphone and ECE, when the tube in the middle of ECE, and hence the tympanic canal, is closed.

However, above 2.5 kHz the transfer function as well as coherence improve. The ECE signal is above the noise floor up to 7 kHz, after which the coherence declines to zero. The explanation for this high-frequency behavior can be understood after considering the other measurement cases. It must be stressed that the increase occurs in the vicinity of the frequency at which the pressure sensitivity starts to increase (figure 41).

II *Tympanic canal open*. Figure 44 shows the transfer function as the canal is closed. Clearly, the trend is similar to the case I. The dip at 900 Hz and the first minimum at 2.5 kHz are both visible in figures 43 and 44. Moreover, the transfer function magnitude drops approximately 40 dB between 0.2 and 2.5 kHz in both cases. Hence, it may be concluded the tympanic canal opening or closuring does not affect the low-frequency performance of the ECE.

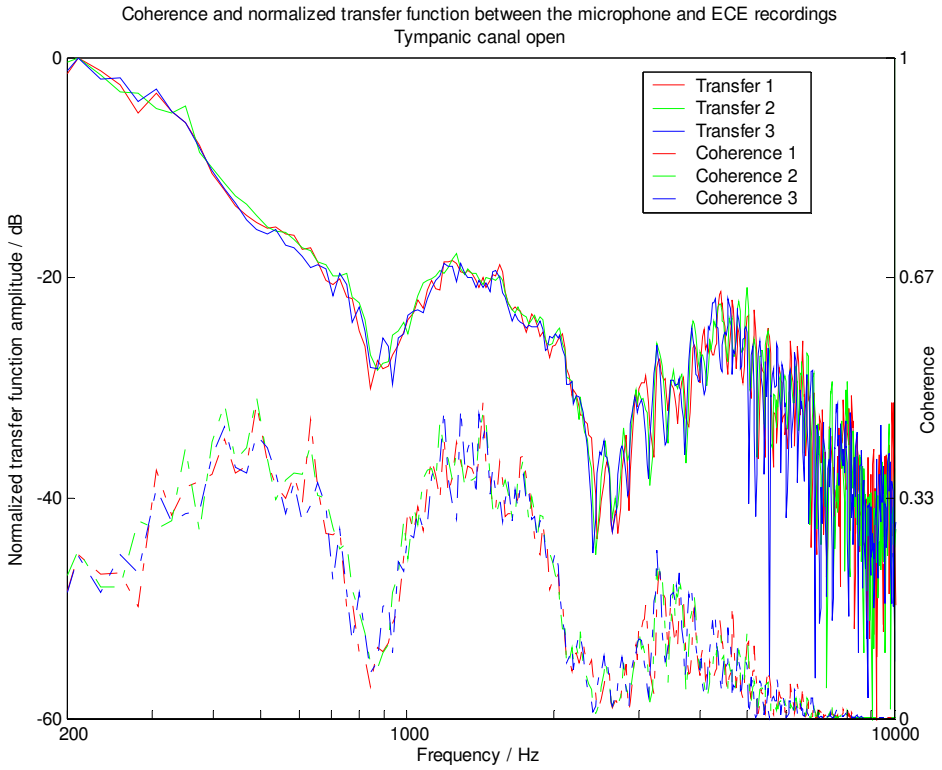

Figure 44. Transfer function and coherence between microphone and ECE, when the tube in the middle of ECE, and hence the tympanic canal, is open.

A minor difference, however, may be observed in the high-frequency behavior. In analogy with the first measurement case, the transfer function begins to increase after the first null at 2.5 kHz. In contrast with the closed-canal measurement, the response in the open-canal measurement begins to decline somewhat earlier. Whereas in the case I the transfer

function maintains relatively high level up to 7 kHz, in the current case the decline occurs just after 4 kHz. However, the data from the second case is generally cleaner based on the visual judgment as well as the coherence and, hence, it is difficult to draw definite conclusions on the true levels and turning points.

III *Tympanic canal open and ear covered.* Figure 45 summarizes the findings from the covered-ear measurement. Once again, the low-frequency characteristics show the downward sloping trend with subtle differences to the previous cases. Firstly, a new notch at 400 Hz occurs. It should, however, be noted that the first measurement (red curve) shows substantially smaller notch than the other measurements. The difference between different measurements is significantly greater at 400 Hz than elsewhere. Therefore, the notch may well be due to the improper positioning of the ECE inside the canal, which causes additional prestress in the structure and changes vibration characteristics.

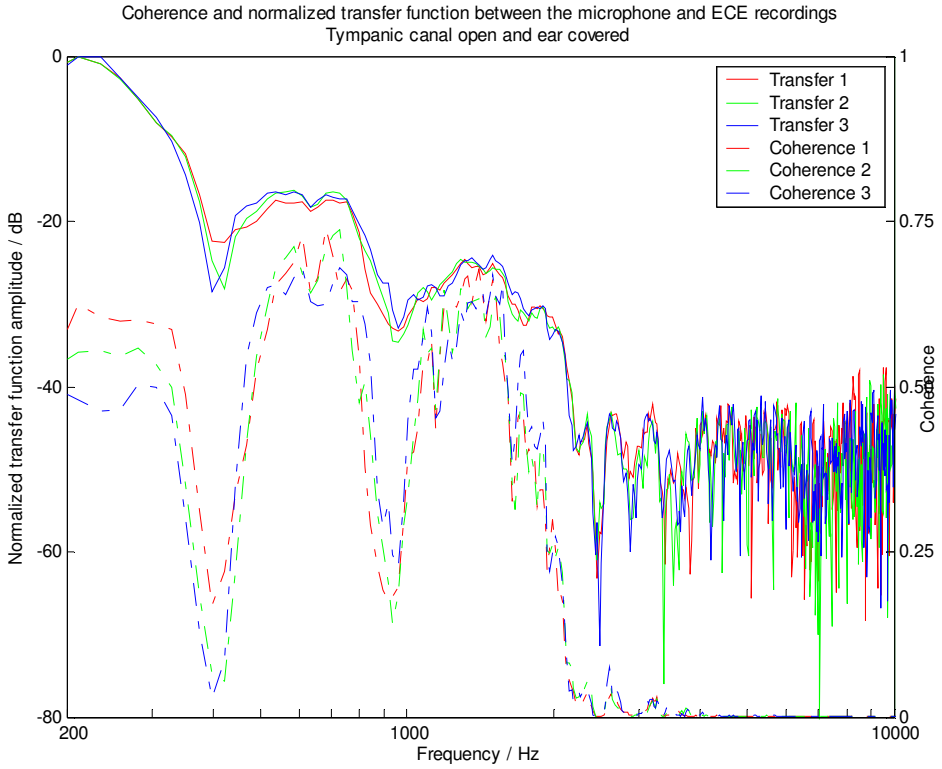

Figure 45. Transfer function and coherence between microphone and ECE, when the ear is covered in order to prevent direct acoustic radiation from reaching the ECE.

Moreover, the transfer function does not increase to such a high level after the 900-Hz notch as in the other cases. In the cases I and II the response rises back to approximately –20 dB. In the case III, the response stays clearly below –20 dB between 1 and 2 kHz.

The high-frequency behavior is in clear contrast with the previous measurements. Now, as in the non-covered measurements the response somewhat increases above 2.5 kHz, here the response clearly stays at the noise floor above 2.5 kHz. The conclusion is that the observed high-frequency rise in the response in the cases I and II is due to the acoustic coupling. Taking into account the rapid increase in the ECE pressure sensitivity at that frequency range (figure 41), the concluded coupling seems further justified.

Notable is that the low-frequency performance did not suffer from covering the ear. The conclusion that can now be drawn is that the ECE detects tissue vibrations up to 2.5 kHz and above that threshold frequency, the coupling is acoustic. By developing a low-noise charge amplifier, the limit might be pushed to somewhat higher frequency. However, the acoustic coupling increases rapidly above 2-3 kHz and, hence, begins to dominate soon after passing the 3-kHz mark.

Findings by Békésy [9] on the behavior of pressure in the closed tympanic canal at low frequencies provide further evidence that the ECE detected vibrations are tissue borne below 2.5 kHz. Békésy's conclusions include that with closed meatus the tone perceived arises mainly from the variation of sound pressure in the tympanic canal resulting from the bone conducted tone. With an open canal, the tissue vibrations can exert only minimal pressure in the meatus. In the bone conduction circumstances, according to Békésy, the pressure in the canal differs by 14 to 20 dB over the quoted frequency range, when comparing open and closed canal situations. However, based on the non-normalized (normalized data shown in figures 43 and 44) transfer function data from the cases I and II, it can be noted that the levels differ by only 2 to 6 dBs over the range of 0.2 - 2 kHz. Therefore, the ECE function does not base on detecting pressure variations below 2.5 kHz, but couples to the acoustic domain only above that threshold.

The question unaccounted for in this analysis is, whether the decreasing response in tissue pick-up is due to the tissue properties or due to the problems in coupling between the tympanic canal walls and the ECE silicone rings. Therefore, future measurements should include measuring the canal wall vibration levels as well as measurements on the ECE output with a known displacement excitation. Only then further conclusions on the transfer path characteristics and coupling efficiency can be drawn.

Penultimately, the Békésy findings may set an upper limit for the usable frequency limit. Now, Békésy found that as the skull bone is excited, there is no increase in the perceived

SPL between open and closed tympanic canal cases above 2.5 kHz. As stated earlier, Békésy deduced that the increase in the perceived loudness at low frequencies is due to the meatus wall movements. Now, as above 2.5 kHz no such increase in the perceived level is observed, it may be concluded that the canal walls do not vibrate at high frequencies. Békésy cleverly notes that this is due to the change in the skull vibration pattern. Therefore, based on this conclusion, 2.5 kHz may be the maximum usable frequency for the ECE-type conduction audio sensor. Comparing the results from the cases I and II to the case III, the 2.5-kHz limit seems plausible. Measuring the canal wall vibration with, say, laser could resolve this open question as well.

Finally, considering the typical noise properties, the ECE frequency characteristics are promising. The energy of noise is usually considered to have ω^{-2}-characteristics [38]. For the sake of an example, power spectrums from several noise cases as well as ω^{-2}-noise are shown figure 46.

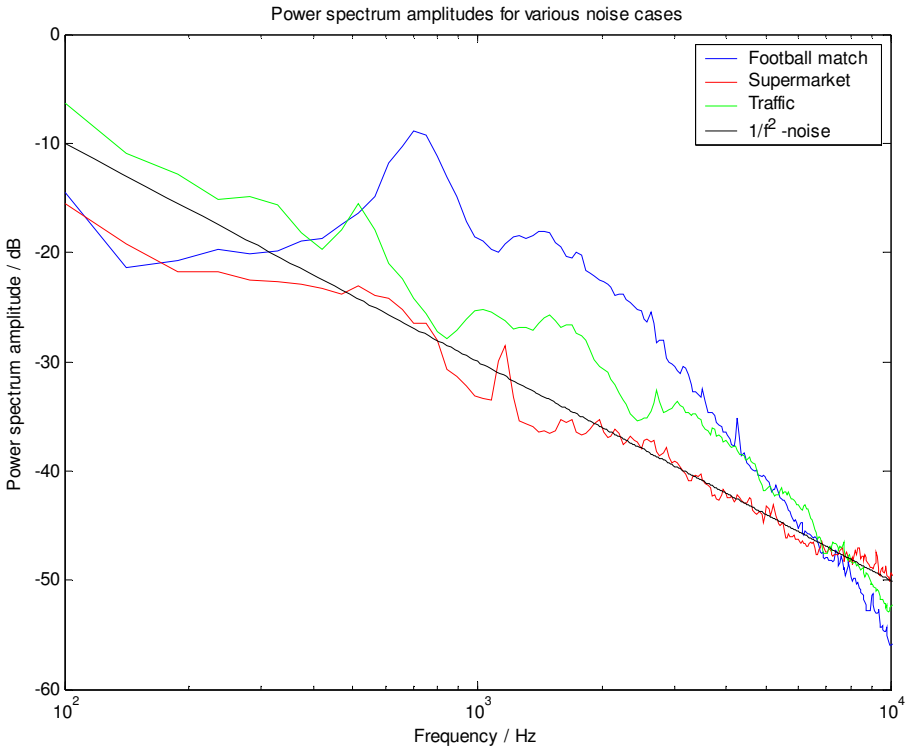

Figure 46. Power spectrums for various noise cases. Supermarket and traffic noise approximately follow the $1/f^2$ –relationship, in football match the decrease in noise energy is even faster.

Since it is now known that the ECE couples well to the tissue domain at low frequencies, where the acoustic coupling, on the contrast, is insignificant, the ECE could significantly

improve the audio quality below 2-3 kHz in noisy conditions. On the other hand, at high frequencies (above 3 kHz), where ECE does not function well, but in which range the noise is also at significantly lower level, a traditional pressure microphone could be utilized.

8.2.3 Lessons learned

Several lessons may be learned for the development of the next generation prototype. They are now summarized.

Electric issues. Solving electric noise problems required significant effort. The cabling and the amplifier design were considered to be the biggest obstacles. The next prototype should include the impedance converter already at the sensor block. Good noise characteristics could, for instance, be achieved by soldering a FET-based impedance converter directly to the piezo electrodes. In such an arrangement, the electric noise arising from long cables and impedance mismatch could be minimized.

Better electric insulation is required for all current carrying parts. It was noticed that if skin touched any non-isolated part, say, piezo electrodes, the amplifier became saturated with noise. Moreover, occasionally ear wax short circuited piezo electrodes leading to random behavior. The sensor might therefore be molded in silicone rubber, in which case also a proper contact between the piezo and coupling material could be secured. The choice to leave electric parts unshielded and use only replaceable silicone rings seems therefore erroneous against these experiences. Replaceable silicon parts can be used in the future as well, but the electric components must be adequately and permanently shielded.

Form factor. With the first prototype the form factor of the ECE was not considered as a primary design goal. The current design provided the proof-of-concept data sought, but it was noticed in practice that inserting the ECE inside the canal was time consuming and unrepeatable. A sensor that expands to couple to the canal walls well should be developed. For instance, canal installable ear defenders use this principle. Such an insertion method would also provide a means to control the static pressure that the sensor exerts on the canal walls. It was noticed that in order to get good SNR, the sensor has to be fairly tightly in the canal. Békésy [9] states that the static pressure controls the transmission loss in bone conduction devices and must therefore be controllable.

Digital Signal Processing. As noted in the measurements, the transfer function between the microphone and ECE declines with increasing frequency. Now, if the transfer function is well characterized, a filter may be set up to equalize the response. More natural sound can be obtained in this manner. Moreover, sudden changes in the tympanic canal shape, cause high peaks in the ECE output. This may happen, for instance, when swallowed as the jaw bone moves and affects the canal positioning and shape. These peaks must be controlled, since they saturate the amplifier. A median filter can be used to remove such high peaks from the signal.

Use cases. The ECE device as it is now, is usable up to 2.5 kHz. With proper impedance conversion at the sensor, the noise floor can be lowered and the usable range could somewhat be extended. If simultaneously the acoustic coupling above 3 kHz could be reduced, the ECE might be usable over the GSM narrowband depending on how fast the wall vibration diminished in the range from 2.5 to 3.5 kHz. The means of reducing the acoustic coupling should be examined thoroughly before building another prototype. Furthermore, if wider bandwidth is required, a traditional microphone can readily be used for high-frequency pick-up.

Finally, the ECE device could be used purely for Voice Activity Detection (VAD). This means that the ECE is not used for pick-up purposes at all, but only provides the DSP processor information on, when the person is speaking. In such a case, an ordinary pressure microphone is utilized for audio pick-up. Other options might include using the ECE and a traditional microphone together. Then a DSP processor could process the audio signal from the microphone based on the ECE provided noiseless signal in order to reduce the noise level in the final audio signal.

Actuator function. As found, the actuator function fulfilled neither the specifications nor expectations. Based on this finding, it may be concluded that the ECE should be inserted deeper in the tympanic canal in order to provide the ECE coupling to the bone instead of soft tissues. However, due to the medical reason it is too risky to build and use such a device. Therefore, it may be questioned, whether the ECE should be in the ear at all. In order to fulfill the sensor task, the sensor may be positioned fairly arbitrarily. It may be located near the jaw bone or on the throat. Of course, in the canal the rejection properties against external noise are better than if the sensor was located on, say, throat.

9. CONCLUSIONS

This study is a proof-of-concept research. The aim in the study is to examine an ear-insert device that can work as a tissue-conducting actuator and sensor in the audio range. The carrying idea is to produce perception of hearing without producing pressure waves in air. In fact, soft tissue is excited instead of air. Moreover, in sensor function tissue vibrations are detected instead of pressure variations. The benefits include efficient coupling in the actuator mode and high rejection ratio of external noise in the sensor mode.

The thesis introduces basic ear anatomy in order to understand better, what is required of such a device. Based on the anatomy studies a FE-model of the ear is developed to study, how ear behaves under such excitation. In addition, structural FE-modeling is studied from a theoretical point of view.

FE-modeling is also utilized in the actuator development. Firstly, piezoelectric theory and the associated FE-formulation are discussed. This establishes grounds to analyze the model and measurement results as well as further refine the actuator model. A prototype of the Ear Canal Exciter (ECE) is manufactured based on the FE-modeling.

Finally, the ECE device is characterized in its real working environment, a tympanic canal. Both, the actuator and sensor functions are characterized and the obtained transfer functions are discussed.

The FE ear model yields excellent results, when compared to the published measurements as well as other FE-models. The novelty value in the model is the use of lumped parameter representation for the ossicles. The articles reviewed clearly show that modeling ossicles is a time-consuming and challenging task. However, only the behavior of the tympanic membrane is of interest in this project. Still, it is important to apply proper ossicles load on the membrane. Hence, a frequency-dependent spring-damper-mass representation is developed for the ossicles. This allows for applying correct boundary conditions on the membrane without modeling the ossicles in detail. The comparison to the other models shows that the method introduced is valid.

The ear model also reveals that the ECE actuator function cannot work. In the FE-model it is observed, how the energy radiated from the ECE dissipates in the surrounding soft tissue layer and does not propagate along the canal towards the tympanic membrane.

Moreover, no sound conduction directly to the cochlea via bone is observed, since it seems that virtually no vibration propagates from the soft tissue to the bone. The impedance difference between the tissue and bone is such significant. These findings are confirmed by subjective listening tests, in which it is concluded that the sound perception resulting from the ECE vibration is purely acoustic and no mechanical transfer of sound occurs. The conclusion is that in order to make the ECE work properly, the actuator should be placed deeper in the tympanic canal to allow for proper coupling to the temporal bone.

The actuator modeling shows that the linear FEM is not able to predict the displacement response of the manufactured actuator. The discrepancy is clear. While the measured response shows a declining response with increasing frequency, the linear FE-model yields a slightly increasing response. The rate of increase in the modeled response may be shown to be in accordance with the behavior of a simple harmonic oscillator.

Detailed considerations are given on how various mechanical and electric parameters affect the response, but no explaining factor is found from these parameter sets. Therefore, in order to model the response properly, a non-linear effect, hysteresis, is considered. Classical rate-independent Preisach-model with a scalar product model for reversible hysteresis is applied to the problem. The hysteretic model shows some decrease in the response as compared to the linear model, but still yields an increasing displacement response with increasing frequency.

Finally, it is noted that literature gives evidence that the rate-dependent Preisach model yields the observed declining response below the first mechanical-response by taking viscous effects into account. It seems that as soft piezoelectric materials are modeled, rate-dependent hysteresis effects cannot be excluded from the analysis. Development of such a model is left for future work.

The measurements on the sensor functionality of the ECE show that the tissue vibrations can be used to pick-up speech up to 2.5 kHz. The finding is supported by the literature. The lower limit is below 200 Hz, which was the cut-off frequency for the measurement system. However, for future purposes measurements concerning the tissue vibration levels in ear are recommended. The measurement would confirm the applicable frequency range. The knowledge of true vibration levels should also yield data to estimate the ECE coupling efficiency to the soft tissue. No such analysis is done in this study due to the lack of measurement data.

Although some general transfer characteristics are measured, the resulting audio quality is, for instance, not characterized in any manner. The reason for this is the high-level of electric noise induced in the system. Therefore, any future prototype must include better control for the impedance match between the sensor and the wiring. In addition, the improved signal-to-noise ratio in the measurements would allow for the characterization of the true external noise-rejection. The external noise rejection characteristics are not measured in this study due to the low SNR of the current prototype-amplifier setup.

Moreover, any future work should also include an attempt to predict the sensor behavior. However, this should be done only after the rate-dependent hysteresis has been implemented in the model. For verification purposes, the sensor output with respect to the displacement input should be measured.

Despite the large number of open questions, the research has achieved the main goal of being a proof-of-concept study. The results show that the proposed actuator function is not feasible, but the sensor function is. The research also shows various points for improvement in the modeling of piezoelectric materials, which information is beneficial in any future work with piezoelectric actuators and sensors.

10. ACKNOWLEDGMENTS

In addition to the persons named in the preface, the author wishes to acknowledge the following persons for their support in making the thesis.

Bergqvist, Anders
ANSYS support
Medeso AB, Sweden

Bright, Andrew
Specialist
Nokia Technology Platforms, Finland

Demkowicz, Leszek
Professor, Department of Aerospace Engineering and Engineering Mechanics
University of Texas, USA

Dobrodolac, Branislav
Researcher, Institute of Theory of Electrical Engineering
University of Stuttgart, Germany

Funnell, Robert
Professor, Biomedical Engineering
McGill University, Canada

Gan, Rong
Professor, Bioengineering
University of Oklahoma, USA

Myllylä, Ville
Senior Research Engineer
Nokia Research Center, Finland

Pääaho, Jouni
Research Engineer
Nokia Technology Platforms, Finland

Sipilä, Markku
Docent, Department of ear diseases
Tampere University Hospital, Finland

Wada, Hiroshi
Professor, WADA laboratory
University of Tohoku, Japan

Zacharov, Nick
Principal Scientist
Nokia Technology Platforms, Finland

11. REFERENCES

[1] Abel, E.W. & Lord, R.M. 2001. A Finite Element Model for Evaluation of Middle Ear Mechanics. Proceedings of the 23rd Annual EMBS International Conference. Istanbul, Turkey, October 25th-28th. Pages 2110-2112.

[2] Allik, H. & Hughes, J. R. Finite Element for Piezoelectric Vibration. International Journal Numerical Methods of Engineering. Number 2, pages 151-157.

[3] Alvord L.S. & Farmer B.L. 1997. Anatomy and orientation of the human external ear. Journal of American Academy of Audiology. Volume 8, pages 383-390.

[4] Anson B.J. & Donaldson J.A. 1981. Surgical anatomy of the temporal bone. 3rd edition. Philadelphia, W.B. Saunders Company.

[5] ANSYS Inc. Canonsburg, PA 15317, USA.

[6] ANSYS Inc. 2004. ANSYS release 8.1 documentation theory reference.

[7] Arfken G.B. & Weber H.J. 1995. Mathematical methods for physicists. 4th edition. London, Academic Press, London.

[8] Bauer, R. & Lotton, P. & Hamery, P. & Bruneau, A.-M. 2003. An active noise reduction earplug using a piezoelectric laterally radiating loudspeaker. Applied Acoustics. Volume 64, pages 591-609.

[9] Békésy, G.V. 1960. Experiments in hearing. McGraw-Hill Book Company.

[10] Benjeddou, A. 2000. Advances in piezoelectric finite element modeling of adaptive structural elements: a survey. Computers and Structures. Volume 76, pages 347-363.

[11] Bertotti, G. & Fiorillo, F. & Pasquale, M. 1993. Measurement and prediction of dynamic loop shapes and power loss in soft magnetic materials. IEEE Transactions on magnetics. Volume 29, number 6, pages 3496-3498.

[12] Bertotti, G. & Basso, V. & Pasquale, M. 1994. Application of Preisach model on the calculation of magnetization curves and power losses in ferromagnetic materials. IEEE Transactions on magnetics. Volume 30, number 2, pages 1052-1057.

[13] Bertotti, G. 1998. Hysteresis in magnetism. San Diego, Academic Press.

[14] Bruneau, A-M. & Bruneau, M. & Lotton, P. & Skvor, Z. 1999. A model to describe the behaviour of a laterally radiating piezoelectric loudspeaker. Applied Acoustics. Volume 58, pages 419-442.

[15] Brown, F.C. 1967. The physics of solids: Ionic crystals, Lattice vibrations and Imperfections. New York, W.A. Benjamin Inc.

[16] Cady, W.G. 1964. Piezoelectricity: An introduction to the theory and applications of electromechanical phenomena in crystals. New York, Dover publications.

[17] Cardelli, E. & Finocchio, G. & Pinzaglia, E. 2004. Increasing the accuracy of the numerical identification of the modified scalar Preisach model. IEEE Transactions on magnetism. Volume 40, number 2, pages 892-895.

[18] Chaplya, P.M. & Carman, G.P. 2001. Dielectric and piezoelectric response of lead-zirconate titanate at high electric and mechanical loads in terms of non-180˚ domain wall motion. Journal of Applied Physics. Volume 90, number 10, pages 5278-5286.

[19] Crocker, M.J. 1997. Encyclopedia of acoustics, 4th volume. New York, John Wiley & Sons, Inc.

[20] Feinberg, B.N. & Fleming, D.G. 1976. CRC Handbook of engineering in medicine and biology. Boca Raton, FL.

[21] Damjanovic, D. 2001. Piezoelectric properties of perovskite ferroelectrics: Unsolved problems and future research. Ann. Chim. Sci. Mat. Volume 26, pages 99-106.

[22] Decraemer, W.F. & Dirckx, J.J.J. & Funnel, W.R.J. 2003. Three-Dimensional Modelling of the Middle-Ear Ossicular Chain Using a Commercial High-Resolution X-Ray CT Scanner. Journal of the Association for Research in Otolaryngology. Volume 4, pages 250-263.

[23] Deloitte. 2004. Mobile and wireless predictions 2004. New York, USA.

[24] Duck, F.A. 1990. Physical properties of tissue: A comprehensive reference book. London, Academic press.

[25] Fung, Y.C. 1993. Biomechanics: mechanical properties of living tissues. 2nd edition. New York, Springer.

[26] Fung, Y.C. 1990. Biomechanics: motion, flow, stress and growth. New York, Springer.

[27] Gan, R.Z. & Sun, Q. 2002. Finite Element Modeling of Human Ear with External Ear Canal and Middle Ear Cavity. Proceedings of the Second Joint EMBS/BMES Conference. Houston TX, USA, October 23rd-26th. Pages 264-265.

[28] Gan, R.Z. & Feng, B. & Sun, Q. 2004. Three-dimensional modeling of human ear for sound transmission. Annals of Biomedical Engineering. Volume 36, number 6, pages 847-859.

[29] Gladilin, E. 2003. Biomechanical Modeling of Soft Tissue and Facial Expressions for Craniofacial Surgery Planning. Doctoral thesis. Berlin, Free University of Berlin.

[30] Global Mobile Suppliers Association, GSA. 2005. GSM/3G market update. Sawbridgeworth, UK.

[31] Gu, H. 2003. Processing of Pb(Mg1/3Nb2/3)O3-PbTiO3 by a novel coating approach. Doctoral thesis. Philadelphia, Drexel University.

[32] Henze, O. & Rucker, W.M. 2000. Application of Preisach model on a real existent material. Proceedings of the 9th International IGTE Symposium on Numerical Field Calculation in Electrical Engineering. Graz, Austria, September 11th –13th. Pages 380-384.

[33] Henze, O. & Rucker, W.M. 2002. Identification procedures of Preisach model. IEEE Transactions on magnetics. Volume 38, number 2, pages 833-836.

[34] Hu, H. & Mrad, R.B. 2003. On the classical Preisach model for hysteresis in piezoelectric actuators. Mechatronics. Number 13, pages 85-94.

[35] Hudde, H. & Engel, A. 1998. Measuring and Modeling Basic Properties of the Human Middle Ear and Ear Canal. Part I: Model structure and Measuring Techniques. Acustica. Volume 84, pages 720-738.

[36] Hudde, H. & Engel, A. 1998. Measuring and Modeling Basic Properties of the Human Middle Ear and Ear Canal. Part II: Ear Canal, Middle Ear Cavities, Eardrum, and Ossicles. Acustica. Volume 84, pages 894-913.

[37] Hudde, H. & Engel, A. 1998. Measuring and Modeling Basic Properties of the Human Middle Ear and Ear Canal. Part III: Eardrum Impedances, Transfer Functions, and Model Calculations. Acustica. Volume 84, pages 1091-1109.

[38] Hänsler, E. & Schmidt, G. 2004. Acoustic Echo and Noise Control – A practical approach. New Jersey, Wiley.

[39] Juuti, J. 2000. Pelkistettyjen ja sisäisesti jännitettyjen pietsosähköisten rakenteiden valmistus ja karakterisointi. Masters thesis. Oulu, Oulu University, Faculty of technology.

[40] Juuti, J. 2005. Private discussions via E-mail with Oulu University Microelectronics laboratory.

[41] Kirikae, I. 1960. The structure and function of middle ear. Tokyo, University of Tokyo Press.

[42] Koike, T. & Wada, H. & Kobayashi, T. 2002. Modeling of the human middle ear using the finite-element method. Journal of Acoustical Society of America. Volume 111, issue 3, pages 1306-1317.

[43] Kärkkäinen, L. 2004. Akustiikan sovelluksia. Lecture notes. Helsinki, Helsinki University.

[44] Lai, W.M. & Rubin, D. & Krempl, E. 1987. Introduction to continuum mechanics. Oxford, Pergamon press.

[45] Liu, J-M. & Yu, H. & Pan, B. & Chen, X.Y. 2005. Dynamic scaling of hysteresis dispersion in ferroelectrics. Material science and engineering B. Number 118, pages 2-6.

[46] Maijala P. 2003. Akustiikan mittaukset. Lecture notes. Tampere, Tampere University of Technology.

[47] Matlab 6.5. The Mathworks. Massachusetts, USA.

[48] Mayergoyz, I.D. 1988. Dynamic Preisach models of hysteresis. IEEE Transactions on magnetics. Volume 24, number 6, pages 2925-2927.

[49] Mayergoyz, I.D. 1991. Mathematical models of hysteresis. New York, Springer-Verlag.

[50] Meschke, G. 2003. Finite Element Methods in Linear Structural Mechanics. Lecture notes. Ruhr-University, Bochum. http://www.sd.ruhr-uni-bochum.de/academics-students/lehre/mastercourse/lectures/finite_element_methods_for_linear_structural_mechanics/fem_e.pdf (Referenced 27th December 2004).

[51] Mittal, S. & Menq, C-H. 2000. Hysteresis compensation in electromagnetic actuators through Preisach model inversion. IEEE Transactions on mechatronics. Volume 5, number 4, pages 394-409.

[52] Morgan Electroceramics. Technical Publication TP-226: Properties of Piezoelectricity Ceramics. http://www.morganelectroceramics.com/pdfs/tp226.pdf (Referenced 9th February 2004).

[53] Morse, P.M. & Ingard K.U. 1986. Theoretical Acoustics. Princeton, Princeton University Press.

[54] Newland, D.E. 1989.Mechanical Vibration Analysis and Computation. New York, John Wiley & Sons, Inc.

[55] Nye J.F. 1969. Physical properties of solids. Oxford, Oxford University Press.

[56] Park, J.B. 1992. Biomaterials: an introduction. New York N.Y., Plenum.

[57] Prendergast, P.J. & Ferris P. & Rice H.J. & Blayney A.W. 1999. Vibro-Acoustic Modeling of the Outer and Middle Ear Using the Finite-Element Method. Audiology & Neuro-Otology. Volume 4, pages 185-191.

[58] Prendergast, P.J. & Kelly, D.J. & Rafferty, M. & Blayney, A.W. 1999. The effect of ventilation tubes on stresses and vibration motion in the tympanic membrane: a finite element analysis. Clinical otolaryngology. Volume 24, pages 542-548.

[59] Ramana, Y.V. & Krishna, G.G. & Khadeer, M.A. 1980. Shear velocity of muscle tissues. Journal of Biomedical Engineering. Volume 2, pages 211-215.

[60] Rao, S.S. 1989. The Finite Element Method in Engineering. 2nd edition. Oxford, Pergamon Press.

[61] Reitz, J.R. & Milford, F.J. & Christy, R.W. 1993. Foundations of electromagnetic theory. New York, Addison-Wesley.

[62] Saunders, W.H. & Paparella M.M. 1971. Atlas of ear surgery. 2nd edition. Saint Louis (Mo.): Mosby, 1971.

[63] Simkovics, R. & Landes, H. & Kaltenbacher, M. & Lerch, R. 2000. Finite Element analysis of ferroelectric hysteresis effects in piezoelectric transducers. Proceeding of the IEEE Ultrasonic Symposium. Puerto Rico, 22nd-26th October. Pages 1081-1084.

[64] Sjöström, M. 1999. Frequency analysis of classical Preisach model. IEEE Transactions on magnetics. Volume 35, number 4, pages 2097-2103.

[65] Stinson, M.R. & Lawton, B.W. 1989. Specification of the geometry of the human ear canal for the prediction of sound pressure level distribution. Journal of Acoustical Society of America. Volume 85, issue 6, pages 2492-2503.

[66] Sun, Q. & Gan, R.Z. & Chang, K.-H. & Dormer, K.J. 2002. Computer-Integrated Finite Element Modeling of Human Middle Ear. Biomechan. Model. Mechanobiol. Volume 1, pages 109-122.

[67] Takuro, I. 1990. Fundamentals of piezoelectricity. Oxford, Oxford University Press.

[68] Torre, E.D. & Oti, J. & Kádár, G. 1990. Preisach modeling and reversible magnetization. IEEE Transactions on magnetics. Volume 26, number 6, pages 3052-3058.

[69] Tressler, J.F. & Alkoy, S. & Newham, R.E. 1998. Piezoelectric sensors and sensor materials. Journal of Electroceramics. Volume 2, issue 4, pages 257-272.

[70] Wada, H. & Metoki, T. & Kobayashi, T. 1992. Analysis of dynamic behavior of human middle ear using a finite-element method. Journal of Acoustical Society of America. Volume 92, issue 6, pages 3157-3168.

[71] Wang, Z.G. & Abel, E.W. & Mills, R.P. & Liu, Y. 2002. Assessment of multi-layer piezoelectric actuator technology for middle-ear implants. Mechatronics. Volume 12, pages 3-17.

[72] Warwick, R. & Williams P.L. 1973. Gray's anatomy. Edinburgh, Longman group Ltd.

[73] Yu, Y. & Xiao, Z. & Naganathan, N.G. & Dukkupati, R.V. 2002 Dynamic Preisach modeling of hysteresis for the piezoceramic actuator system. Mechanism and Machine Theory. Number 37, pages 75-89.

[74] Zemlin, W.R. 1981. Speech and hearing science: anatomy and physiology. 2nd edition. Englewood Cliffs, Prentice-Hall.

[75] Zienkiewicz, O.C. & Taylor, R.L. 1994. The finite element method, volume 1. 4th edition. London, McGraw-Hill.

APPENDIX A. DIFFERENTIAL CHARGE AMPLIFIER FOR PIEZOS

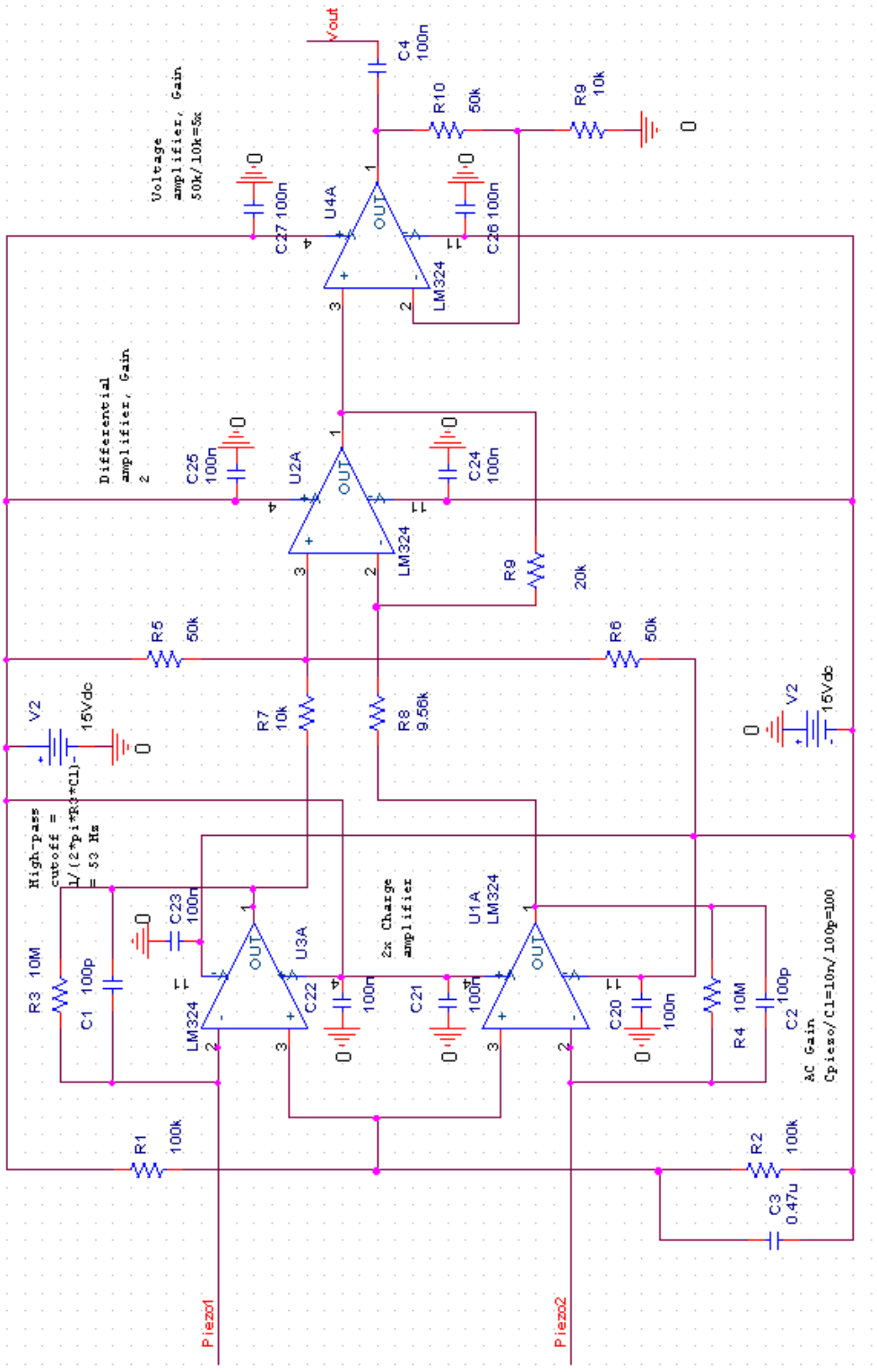

APPENDIX B. PATENT APPLICATION FI 20041625

REMOVED FROM THE VERSION POSTED TO INTERNET.

APPENDIX C. DETERMINING THE UNKNOWN 2-PORT MATRIX ELEMENTS

Equation (90) defined the mechanical 2-port for the piezo structure:

$$\begin{bmatrix} F_x \\ F_z \end{bmatrix} = \begin{bmatrix} C_{11} & C_{13} \\ C_{13} & C_{33} \end{bmatrix} \begin{bmatrix} \Delta x \\ \Delta z \end{bmatrix} \qquad \text{(90) rewritten}$$

Note that the equality of 1-2 and 2-1 elements in the C-matrix is based on the reciprocity principle. Define an inverse mapping

$$\begin{bmatrix} \Delta x \\ \Delta z \end{bmatrix} = \begin{bmatrix} A_{11} & A_{13} \\ A_{13} & A_{33} \end{bmatrix} \begin{bmatrix} F_x \\ F_z \end{bmatrix}, \qquad (109)$$

where

$$\begin{bmatrix} C_{11} & C_{13} \\ C_{13} & C_{33} \end{bmatrix} = \begin{bmatrix} A_{11} & A_{13} \\ A_{13} & A_{33} \end{bmatrix}^{-1} \qquad (110)$$

Now, equation (109) implies a procedure for determining the unknown matrix elements.

1. By applying force in x-direction (note that F_z then zero, since there are no constraints in z-direction), it is obtained

$$A_{11} = \frac{\Delta x}{F_x} \text{ and } A_{13} = \frac{\Delta z}{F_x}. \qquad (111)$$

2. By applying force in z-direction (note that F_x then zero, since there are no constraints in x-direction), it is similarly obtained

$$A_{13} = \frac{\Delta x}{F_z} \text{ and } A_{33} = \frac{\Delta z}{F_z}. \qquad (112)$$

3. The redundancy in the determination of A_{13} can be used a check.

4. Finally, a modal analysis is run to find the first resonance frequency ω_0. For a simple harmonic oscillator the first resonance frequency is given by

$$\omega_0^2 = \frac{k_{eff}}{m_{eff}}. \qquad (113)$$

Hence, using equation (96) it is obtained

$$\omega_0^2 = \frac{C_{33} - \dfrac{C_{13}^2}{C_{11} - \dfrac{A_x c_{11}}{L_x}}}{m_{eff}}, \tag{114}$$

which allows for determining the effective mass for the lumped parameter model.

5. The structure geometry as well as the appropriate material parameters are defined in ANSYS FE-software, which makes it straightforward to apply proper boundary conditions and determine the required elongations.

Results

For the elements of the 2-port matrix, the FE-analysis yields

$$\begin{bmatrix} A_{11} & A_{13} \\ A_{13} & A_{33} \end{bmatrix} = \begin{bmatrix} \Delta x / F_x & \Delta x / F_z \\ \Delta z / F_x & \Delta z / F_z \end{bmatrix} = \begin{bmatrix} 0.3905 \cdot 10^{-8} / 1/120 & 0.1615 \cdot 10^{-8} / 1/1000 \\ 0.1940 \cdot 10^{-7} / 1/120 & 0.1972 \cdot 10^{-7} / 1/1000 \end{bmatrix} \tag{115}$$

Above it was stated that the 1-2 and 2-1 elements should be equal. However, now their ratio is 0.69 . The reason may be in the used boundary conditions or numerical accuracy. Also, it should be noted that since forces and displacements in y-direction are not accounted for in the 2-port model, the reciprocity principle may not be valid. Despite this, the average of the 1-2 and 2-1 elements will be used as the A_{13}-element.

Finally, modal analysis yields for the resonance frequency

$$\omega_0^2 = 4\pi^2 \cdot 33146^2 \frac{1}{s^2},$$

from which it further follows that $m_{eff} = 2.4$ mg.